Atomistic Modelling Approaches to the Challenges in Lithium – Sulfur Batteries

by

Haesun Park

A dissertation submitted in partial fulfillment
of the requirements for the degree of
Doctor of Philosophy
(Mechanical Engineering)
in the University of Michigan
2019

Doctoral Committee:

Associate Professor Donald J. Siegel, Chair
Assistant Professor Yue Fan
Professor Wei Lu
Assistant Professor Liang Qi

Haesun Park

haesun@umich.edu
ORCID: 0000-0001-6266-8151

Acknowledgements

First and foremost, I would like to express my sincere and profound gratitude to my advisor, Professor Don Siegel. When I started my graduate study, senior graduate students advised me that the most important task is to find a good advisor, and, in that sense, I was so lucky to have him as my advisor. He was a great teacher and scientist who always gave me right guidance and insightful comments which made me easily resolve the hardships that I encountered while conducting my research. Also, his kindness and willingness to help students made it easier to communicate with him, so I was able to have lots of valuable discussions where I learned most of my scientific knowledge during my PhD. None of my PhD works would have been accomplished without his support and patient.

I'm grateful to my committee members, Professors Wei Lu, Yue Fan, and Liang Qi for taking their time to assess my dissertation and providing valuable suggestions. I express additional thanks to Prof. Yue Fan for his great lecture of defects in solids which gave me a precious lesson on how the MD can be extended to mechanical properties of solids. I also appreciate his encouragement and support throughout my postdoctoral job search.

I also appreciate to Professor Jeff Sakamoto who gave me a chance to conduct experiments on sulfide solid electrolytes in his lab. Although they are not included in my dissertation, it was a priceless experience because I was able to compare my simulation works with experimental results. I specially thank to Regina Garcia-Mendez and Andrew Davis for their practical helps (EIS, XRD, XPS, sample preparation, sputtering; namely everything in the lab). I would like to thank to my collaborators from Demark; Prof. Tejs Vegge, Prof. Juan Maria Garcia Lastra, and Dr. Marko Melander. I enjoyed learning about their constrained-DFT for nonadiabatic charge transport calculations which made our paper novel.

I would also like to acknowledge to all the members of the Siegel group, from past to now, for their support and fruitful discussions during my graduate study. The majority of my scientific knowledge was built through the valuable interactions with the lab members. I extend my gratitude to Hyun who taught me every single and small step to run the VASP code in the supercomputer. I

also appreciate to Dr. Max Radin, Dr. Sheng Yang, and Dr. Jeff Smith for their advice and discussions which were very helpful to my study on defects in Li_2S. I would like to thank to Dr. Nitin Kumar for close collaborations and discussions in our charge transport paper. I also acknowledge to Dr. Seungho Yu for helping in calculating the stabilities of solid electrolytes as well as being a great golf buddy. I acknowledge to Dr. Alauddin Ahmed for introducing the machine learning based materials discovery and advising on planning a successful future career as a researcher. I still thank to Kwangnam Kim, Dr. Jeff Lowe, Kely Nagy, Mallory Fuhst, Steven Kiyabu, and Everardo Olide for their kindness and willingness to help.

I should thanks to my friends from Michigan for their friendship and support. I appreciate Korean friends from ME and EECS for taking their time to have conversation with me when we encounter at the GGB hallway. I especially thank to Sangeon Lee, Jeongseop Yoon, and Hyunwook Cho.

I acknowledge financial support from the Kwanjeong Educational Foundation during my master's degree. Without their support, I could not start my graduate degree in the first place. I also appreciate the financial support for the Joint Center for Energy Storage Research (JCESR), an Energy Innovation Hub funded by the U.S. Department of Energy, Office of Science, and Basic Energy Sciences.

Finally, I cannot say enough words to thank to my parent for their endless support and understanding. Lastly, but mostly, I thank to my beloved wife, Yeonjee Bae, who has motivated and encouraged me with everlasting love and support over the last 10 years.

Table of Contents

List of Tables

List of Figures

Abstract

Internal combustion engine vehicles (ICEVs) rely on petroleum-based fuels; these fuels have limited reserves and their combustion is a major contributor to climate change. These issues have triggered the development of electric vehicles (EVs) that use electricity stored in Li-ion batteries as a fuel. However, the performance of current Li-ion technology has largely plateaued, yet the driving range of EVs remains below that of conventional ICEVs. This limitation has sparked a search for safer battery chemistries with higher capacities than Li-ion at lower cost.

The lithium-sulfur (Li-S) battery is one promising chemistry due to its high theoretical energy density and potential for low cost. Despite these benefits, Li-S batteries are not commercially feasible yet because their cycleability and practical energy density do not meet expectations. The limited performance is attributed to deficient understanding of several phenomena, including slow transport in the positive electrode, dissolution of polysulfide species, and the cycleability of Li metal anodes. This thesis aims to provide insight into these mechanisms using density functional theory (DFT) calculations, and thereby provide information aiding the design of Li-S systems.

As a first step in understanding the fundamental features of Li-S batteries, the state-of-art DFT techniques were applied to predict several properties of redox end members in Li-S batteries. More specifically, the relative stabilities of the α- and β- sulfurs were confirmed by calculating the phase diagram. Similarly, the stability analysis of Li_2S_2 suggests that this is a metastable phase. The equilibrium crystallites of Li_2S are predicted to be comprised entirely of stoichiometric (111) surfaces, while for α-S a mixture of several facets is predicted. Finally, α-S, β-S, Li_2S, and Li_2S_2 are predicted to be insulators with band gaps greater than 2.5 eV.

Regarding PS dissolution from the cathode, metal-organic frameworks (MOFs) are explored as cathode support materials. MOFs combine encapsulation and chemical adsorption as strategies for minimizing PS dissolution. Optimal MOF compositions are pinpointed by computationally screening 16 metal-substituted variants of M_2(dobdc) for their ability to chemically anchor prototypical PS species. Ti_2(dobdc), Ni_2(dobdc), and Mo_2(dobdc) are identified as the

compositions with the largest affinities for Li_2S_4 and Li_2S. As Ni_2(dobdc) has been synthesized previously, this MOF is proposed as a promising cathode support for Li-S batteries.

Charge transport limitations through insulating Li_2S and α-S have the potential to constrain the capacity of Li-S batteries. Therefore, understanding these charge transport mechanisms is a prerequisite for enhancing cell performance. Charge transport mechanisms were explored in both the adiabatic and nonadiabatic regimes. Charge transfer in Li_2S is predicted to be adiabatic. In sulfur, however, transitions between S_8 rings are nonadiabatic and conventional DFT overestimates charge transfer rates. Delocalized holes are predicted to be the most mobile charge carriers in α-S; in Li_2S hole polarons dominate.

Finally, the last portion of this dissertation examines sulfide-based solid electrolytes (SSEs). These electrolytes are expected to enable the use of a high-capacity Li-metal anode. Realizing these systems requires stability between the SSEs and Li metal. This stability is investigated computationally by predicting band edge positions. Based on this information we predict the likelihood charge injection from Li anodes. Our calculations reveal that reduction by Li is expected for all SSEs examined. The position of the CBM is sensitive to the surface features of the SSE and varying the surface composition of Li_3BS_3 can stabilize the Li/Li_3BS_3 interface.

Chapter 1 Introduction

1.1 Motivation

Global dependence on oil as an automotive fuel remains a serious environmental concern. The vast majority of current automobiles employ an internal combustion engine (ICE) fueled by petroleum-derived liquid fuels such as gasoline.[1] Gasoline is an excellent energy storage material due to its high gravimetric (13,000 Wh/kg) and volumetric (10,000 Wh/L) energy densities,[2] which enable a driving range of more than 500 km. However, the carbon emissions resulting from gasoline combustion increase the risk of climate change. The magnitude of petroleum reserves is also uncertain.[3-4]

One solution to these problems is to transition from ICE-based automobiles to electrified vehicles (EV) which use electricity as a power source. Unlike petroleum, electricity has diverse generation sources such as solar power, geothermal, and gravitational.[2] These sources are almost limitless, so they are frequently referred as *renewable energy*. The transition to EV's is already on-going, with an acceleration anticipated in the future. According to the International Energy Agency (IEA), the global stock of EVs exceeded 3 million in 2017; approximately 100 million EVs have been forecast for 2030.[5] While the EV market share was only 0.2% in 2016, this number is expected to increase to ~90% in 2060.[6]

Such a rapid increase in the EV sector is attributed to Li-based rechargeable energy storage systems, Li-ion batteries. Despite the higher energy density of Li-ion systems (~350 Wh/kg[7-13] theoretically and ~120 Wh/kg[14] at the system level) compared to earlier approaches based on nickel-metal-hydride or lead-acid systems, further gains in capacity are highly desirable for emerging applications such as EVs.[7-14] The fact that Li-ion based EVs have inadequate driving range, high cost, and may be subject to potential resource constraints, call into question the future market for EV's based on Li-ion batteries.[15-16] These barriers motivate the search for new battery chemistries having higher energy densities and at lower cost;[17] these are often referred as *beyond Li-ion batteries*.

1.2. Lithium-Sulfur Batteries

The Lithium – Sulfur (Li–S) chemistry is one promising beyond Li-ion candidate due to its high energy density, low cost, and the high abundance of sulfur.[8] The net electrochemical reaction, $2Li + S \rightarrow Li_2S$, has high theoretical energy density of 2,199 Wh/L ($Li + Li_2S$) and specific energy of 2,567Wh/kg; these values are approximately 2 and 7 times higher than those of a typical Li-ion cell, respectively.[8] Sulfur raw materials are only $69/ton and the estimated S reserves on earth is 600 billion tons[18]; hence, S is an economically viable material. Figure 1.1 shows the projected vehicle prices and the corresponding driving range of a variety of battery chemistries at the worse and best scenarios. Based on this data it is clear that Li-S batteries are highly promising.[6]

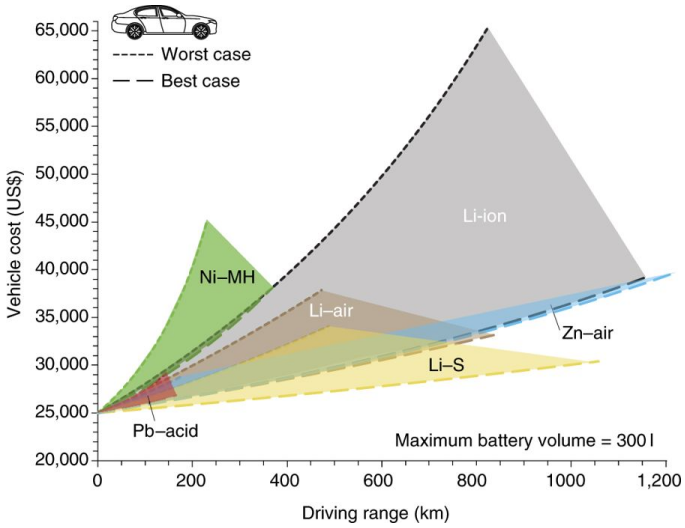

Figure 1.1 Sensitivity to minimum specific energy, minimum energy density, maximum cost and maximum system overheads (defined as the worst-case characteristics) and maximum specific energy, maximum energy density, minimum cost and minimum system overheads (defined as the best-case characteristics) for each battery.

1.3. Challenges in Li-S batteries

Although recent cell designs involving nano-structured cathodes have improved cycleability and sparked renewed interest in sulfur-based systems[19-23], several performance gaps should be addressed before these systems become commercially viable. The presumably insulating nature of solid-state redox end members consisting of sulfur and metal sulfides[20] limit the recharging efficiency, and capacity fade[24] arising from the so-called "polysulfide shuttle" effect deteriorates cycleability. Also, an approach that allows for use of a Li metal anode has yet to be demonstrated. One promising solution is to substitute a Li-ion conducting solid for commonly-used liquid electrolytes.[25]

The foregoing discussion suggests that several fundamental performance gaps need to be addressed for Li-S batteries to become viable. As a step toward closing these gaps, this dissertation focuses on improving our understanding of the following four topics using first-principles calculations:

1) Properties of the redox-end members, Li_2S, S, and Li_2S_2
2) Cathode support materials that can control PS dissolution
3) Slow charge transport in Li_2S and S_8
4) Reductive stability of S-based solid electrolytes

1.3.1. Properties of Redox-end Members

One issue of both fundamental and practical importance in Li-S batteries is the relative stability of Li-S redox end members. For example, lithium persulfide, Li_2S_2, has been proposed as an insoluble discharge product in Li-S batteries.[20, 26-27] The formation of Li_2S_2 would be undesirable, as it has been suggested to limit capacity.[24, 26-27]However, as Li_2S_2 does not appear in the Li-S phase diagram,[28] its presence as a discharge phase remains a matter of debate. A recent study based on X-ray absorption near-edge spectroscopy (XANES)[29] found no evidence for the presence of Li_2S_2 during battery operation. Likewise, Hagen *et al.* employed Raman spectroscopy to characterize polysulfide formation in the Li-S system, but was unable to directly identify Li_2S_2.[30]

In a similar vein, the presence of higher-temperature allotropes of sulfur has been suggested to impact the longevity of Li-S batteries. Recent experiments employing encapsulated sulfur or carbon fiber-sulfur composite cathodes[18,26] have observed the presence of β-sulfur, a monoclinic phase which in bulk form has been reported to be stable at temperatures above approximately 95^{o}C.[31] However, these measurements were performed using cells cycled at room temperature[19, 26] and reported reduced capacity fade. It was therefore suggested that the formation of β-sulfur could improve the cycleability, although the mechanism by which this could occur is unclear.

Another issue which can impact battery performance is surface properties (*i.e.*, composition and structure) of the redox end members.[32] The surfaces of these phases are expected to play a critical role in both electrochemical and chemical processes occurring in the cathode of Li-S batteries. For example, discharge[33] of a Li-S cell is believed to occur via the formation of soluble polysulfides according to the sequence:[8, 23]: $S_8 \rightarrow Li_2S_8 \rightarrow Li_2S_6 \rightarrow Li_2S_4 \rightarrow Li_2S_2 \rightarrow Li_2S$. From the standpoint of electrochemistry, charge transfer to/from these species is likely to occur at surfaces of the solid-phase redox end members. From a chemical standpoint, surfaces are also

likely to be the location for processes such as disproportionation, nucleation, and growth. The importance of surface phenomena also extends to approaches involving sulfur cathodes pre-loaded with Li_2S particles.[34-36] In this regard, a necessary step in understanding the reaction sequence associated with cycling of a Li-S cell is to determine the stable surface terminations of solid phases present in the sulfur cathode.

Transport phenomena are also expected to impact the performance of Li-S batteries. For example, sulfides are believed to be electrically insulating,[37] and electrical passivation by a resistive discharge product has been proposed as a major obstacle to achieving both high capacity and efficient charging in related precipitation-dissolution systems such as the Li-O_2 battery.[38-39] In the case of Li-S batteries, a thick film of sulfur or Li_2S could limit charge transfer across the film, leading to early cell death during discharge and high overpotentials during charging.[36] Consequently, the charge transport properties of redox end members play an important role in battery performance. Nonetheless the band gaps of these phases have received relatively little attention.

1.3.2. Polysulfide Dissolution

The commercial viability of Li-S batteries is limited by their tendency to undergo capacity fade upon cycling. This effect can be traced to the so-called "poly-sulfide shuttle,"[24] which arises from the formation of polysulfide (Li_2S_x) intermediates during discharge. The polysulfides (PS) are highly soluble within conventional organic liquid electrolytes. This solubility is deemed to be undesirable, as it can entail uncontrolled deposition of the Li_2S discharge product within the positive electrode, and crossover of PS to the anode. Both processes result in a loss of active material. For example, deposition of insulating Li_2S on the anode surface can impede charge transfer, limiting capacity and power density.[40-41] Also, due to the PS shuttle effect, Li-S batteries experience self-discharge.[42] Consequently, PS dissolution leads poor cycling performance of Li-S cell, as described in Figure 1.2.[43]

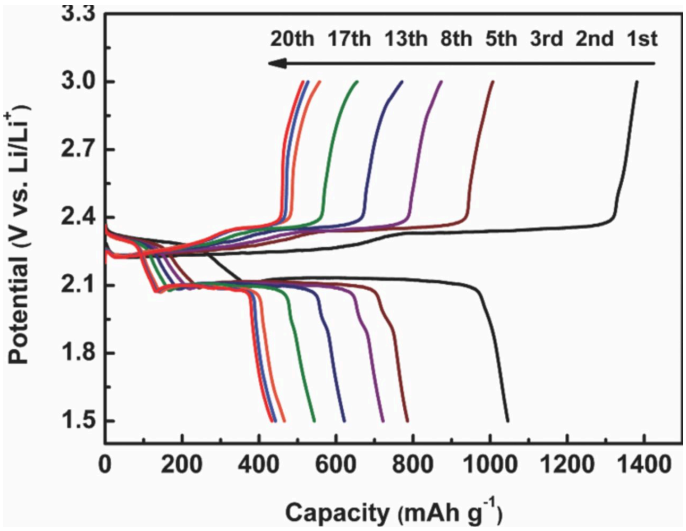

Figure 1.2 Discharge/charge curves of Li-S cell at a current density of 0.1C for 20 cycles[43]

Given the performance limitations arising from polysulfide dissolution, many strategies have been proposed to confine the PS, or dramatically reduce their solubility.[44-57] Perhaps the most widely-studied strategy employs physical encapsulation of sulfur and PS. For example, Nazar *et al.*[20] used mesoporous carbon to encapsulate elemental sulfur and the discharge products within the cathode. Approaches[20, 22, 58-61] involving infiltration of molten sulfur into hollow carbon materials also have been reported to enhance the cycleability of Li-S cells. However, due to the weak interaction between PS and these host materials the confinement is often imperfect, and some PS eventually escape.[62]

As an alternative strategy to physical encapsulation, Nazar and co-workers proposed that capacity retention can be strongly influenced by the surface area of the cathode support and the support's affinity for PS.[63] This was demonstrated by comparing the performance of supports based on porous carbons (Super P, Vulcan, FW200), Ti_4O_7-C, electrolytic manganese dioxide (EMD), anatase-TiO_2, meso-TiO_2, graphene oxide (GO) and MnO_2. Materials with strong PS adsorption exhibited low irreversible capacity loss. Improved cycleability attributed to PS adsorption has also been observed in cells where 2-D materials such as SiO_2[64] and TiO_2[65] were added to the cathode. Cui *et al.* designed yolk-shell structures using TiO_2[66] and various metal sulfides[67] that showed low capacity fade (0.033%/cycle). The bonding between 2-D metal chalcogenides and polysulfide species/S_8/Li_2S were examined computationally.[68] The use of metal chalcogenides as cathode supports also showed improvement in performance.[69-73] Additional development of these strategies is needed to simultaneously achieve high sulfur loadings and PS retention.[62]

The foregoing discussion highlights encapsulation and adsorption as two strategies for limiting PS dissolution. At present, it appears that neither approach is sufficient on its own; therefore, it is natural to ask whether superior performance could be achieved through their *combination*. For this approach to succeed, a porous cathode support with a high density of adsorption sites is needed. Metal-organic frameworks (MOFs) are one class of materials that can satisfy these requirements. MOFs are micro-porous, crystalline materials made via self-assembly of metal clusters and organic linkers.[74] Due to their high surface areas, structural diversity, and potential to exhibit coordinately unsaturated metal sites (CUS), MOFs are candidates for use in a wide variety of applications, including the storage of molecular species such as CO_2,[74-76] CH_4,[77-78] and H_2.[5, 79-80] An additional advantage of MOFs is that their composition – and, consequently, their performance – can be tuned via metal substitution.[74]

Among the thousands of reported MOFs, the compound M_2(dobdc)[81] exhibits several properties that are conducive to its use as a Li-S cathode support. [M_2(dobdc) is comprised of unsaturated metal $(M)^{2+}$ ions in a square-pyramidal coordination arranged in linear, infinite chains linked by 2,5-dioxido-1,4-benzene dicarboxylate (dobdc) linkers.] First, the nano-scale pores of M_2(dobdc) are arranged in a 1-D close-packed (honeycomb) structure, consistent with low-tortuosity access of Li-ions and encapsulation of active materials. Second, the density of CUS in M_2(dobdc) is the highest for any known MOF, thereby providing a high number of PS adsorption sites. Finally, the surface area of M_2(dobdc), $>\sim 1{,}000 m^2/g$,[82] is much higher than that of other sulfur host materials ($<\sim 300 m^2/g$),[63] consistent with a high sulfur loading. The MOF support is envisioned to encapsulate both redox end members (S and Li_2S) and all PS intermediates present during cell operation. In principle, there is no need for any of these compounds to migrate in to or out of the pores if they are accessible to Li^+ and electrons.

Based on these data, and following the analysis performed in Ref. [63], the adsorption capacity of M_2(dobdc) is predicted to range from 6.6 to 13.4 mg of Li_2S_4 per 10 mg of MOF. (The capacity range arises from variations in the CUS composition; we also assume 1 molecule of Li_2S_4 is adsorbed per CUS.) These theoretical capacities outperform the best sulfur support material demonstrated in the literature, MnO_2, which has an adsorption capacity of ~6 mg Li_2S_4/10 mg MnO_2.[63] Other examples include TiO_2 (~2.5 mg/10 mg) and graphene oxide (~5 mg/10 mg).[63]

Despite these potential benefits, studies exploring the use of MOFs in Li-S battery cathodes are relatively rare.[62] To our knowledge, the earliest study to employ MOFs in these batteries was

that of Tarascon *et al.,* who reported the performance of a MIL-100(Cr)-based composite cathode.[83] Subsequently, Zhou *et al.* examined ZIF-8, MIL-53(Al), NH_2-MIL-53(Al) and HKUST-1-based cathodes, and demonstrated that a ZIF-8 based electrode can achieve 300 cycles at relatively high rates (0.5 C), corresponding to a capacity fade of only 0.08%/cycle.[84] Qian *et al.* demonstrated a HKUST-1-based cathode with a high sulfur loading (40 wt. % of the S+MOF mass), a lifetime of 170 cycles, and a capacity at the conclusion of cycling of approximately 500 mAh/g.[85] Wang *et al.* explored composite cathodes based on the MOF-525 series.[86] A cell using MOF-525(Cu) demonstrated the best performance to-date for a S/MOF composite cathode, with a reversible capacity of 700 mAh/g after 200 cycles at 0.5C.[86] Zheng *et al.* examined Ni- and Co-MOF-based S cathodes experimentally and computationally.[87] The Ni-MOF cathode exhibited superior performance (89% capacity retention over 100 cycles at 0.1 C), which was attributed to the synergistic effects of physical encapsulation and strong interactions between PS and the Ni(II) sites. Finally, MOFs have also been examined as solid electrolyte hosts in Li-ion batteries[88] and as separators in Li-S batteries.[89]

1.3.3. Slow Charge Transport in Li_2S and S_8

Strategies aimed at suppressing PS dissolution are expected to alter electrochemical reactions in the cathode such that they become localized near the surface of the cathode support, resulting in more solid-state-like behavior.[90-91] Consequently, transport mechanisms involving solid-state S and Li_2S are expected to play an important role in this 'surface mediated' regime. Transport limitations involving both S and Li_2S REM are possible, as both phases are insulators with large bandgaps.[92-93]

Regarding Li_2S, the formation of this compound during discharge can mimic the behavior of Li_2O_2 in Li/O_2 cells. Earlier studies on the Li/O_2 system have shown that the insulating nature of the Li_2O_2 discharge product can limit capacity and increase overvoltages during charging.[38, 94-100] Thus, by limiting PS solubility in Li-S cells one risks trading the PS dissolution problem for a transport problem arising from cathode passivation. Passivation can also be a concern in Li-S cells in the charged state: oxidation of Li_2S during charging generates sulfur, which is also a poor electronic conductor. Transport through S may also be an important consideration in optimizing the initial distribution and loading of S in the cathode, to maximize S utilization. In total, transport limitations in Li-S cells may pose challenges that are double those of the Li/O_2 system, because in the former chemistry *both* REM are electronic insulators.

Figure 1.3 illustrates plausible electronic and ionic transport mechanisms that may occur in the cathode of a Li-S cell during discharge or charge. Figure 1.3 (a) demonstrates electronic transport through a sulfur film that covers a carbon cathode support. Reduction of S_8 to S_x^{2-} requires charge transport from the current collector to the reaction site on the S surface. This could result in solid-state film growth of Li_2S at the reaction site, or the formation of soluble PS that ultimately precipitate as Li_2S elsewhere in the cell.

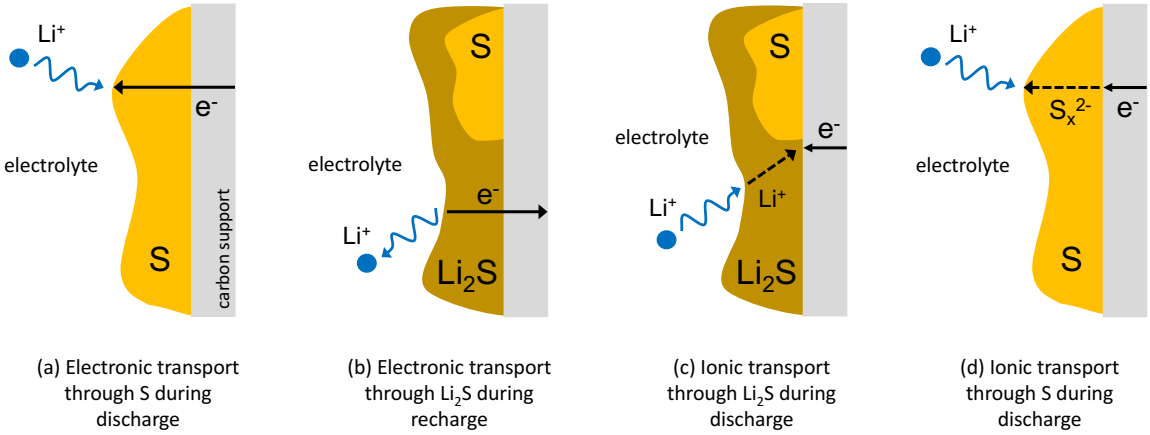

Figure 1.3 Possible electronic and ionic transport processes in the cathode of a Li-S cell during discharge or charging. Yellow represents sulfur, brown represents Li_2S, and grey represents the cathode support (assumed to be carbon).

An alternative scenario occurs when S does not completely cover the carbon support. This creates a three-phase boundary between the electrolyte, S, and the support in the fully or partially charged state.[101] Consequently, facile electronic charge transport would occur (at least initially) through the conductive support, and not through insulating S. However, deposition of Li_2S as discharge progresses can ultimately bury the three-phase interface, as depicted in Figure 1.3 (b). In this case, electronic transport through insulating Li_2S is necessary during charging.

The need for long-range electronic transport can be minimized if rapid ionic transport through Li_2S is possible. For example, Figure 1.3 (c) shows that Li_2S or PS can grow at buried Li_2S/S or Li_2S/support interfaces if Li_2S conducts Li-ions. Similarly, transport of reduced S ions, S_x^{2-}, through S (or Li_2S) could allow Li_xS_y formation on the surface of these phases, Figure 1.3 (d).

Understanding the transport properties of the S and Li_2S REMs is a prerequisite for the development of rational strategies to improve the capacity, efficiency, and cycle life of Li-S batteries. Nevertheless, transport mechanisms in these compounds have not been widely studied, especially in the case of S.[102-105] While a few studies exist for Li_2S, consensus regarding the dominant charge-carrying species has been slow to emerge. For example, Kang *et al.* reported that

the dominant charge carriers in Li_2S are negative Li and positive S vacancies, based on calculations performed at the hybrid functional level of theory. The most likely electronic charge carrier was predicted to be the electron polaron, which localizes on sulfur ions.[92] In contrast, Mukherjee *et al.* argue that hole polarons are formed on sulfur ions in Li_2S and, together with negative Li vacancies, serve as lowest energy charge carriers.[105] Moradabadi and co-workers found that the dominant charge carriers were Li vacancies and Li interstitials, based on calculations employing a semi-local functional.[103] (Li interstitials were not considered in Refs. [92] and [105].) Finally, Mukherjee *et al.* reported that the main charge carriers in metastable[93] Li_2S_2 (based on a hypothetical crystal structure) are hole polarons and negatively charged Li vacancies.[104]

More generally, nearly all prior studies on charge migration/hopping in cathode materials (typically involving localized electronic carriers such as polarons)[102-104] have been performed assuming these are *adiabatic* processes. Within the adiabatic picture, the Born-Oppenheimer approximation is assumed to hold, and it is thus sufficient to map the minimum energy pathway (MEP) along a single, smoothly varying electronic ground state, using, for example, the nudged elastic band method (i.e., green curve in Figure 1.4).[106-108] The rate constant can then be derived from the energy at the saddle point along the MEP using (harmonic) transition state theory.

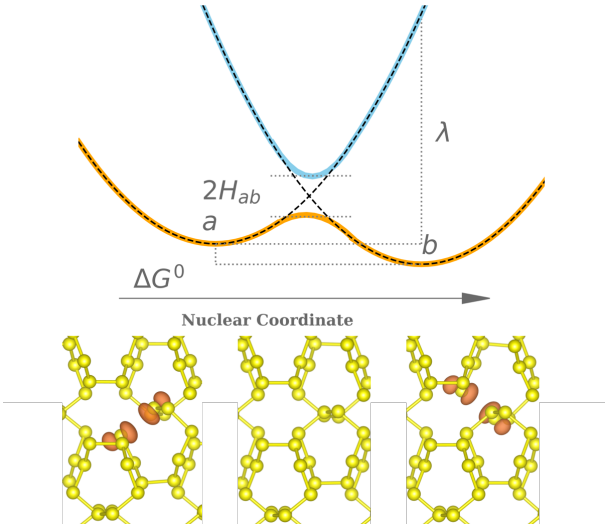

Figure 1.4 Schematic representation of charge transfer in Marcus theory. The orange (blue) solid line is the adiabatic ground (excited) state while the dashed lines are the two diabatic states describing the initial (a) and final (b) states. H_{ab} is the coupling constant, ΔG^0 is the free energy of the reaction, and λ is the reorganization energy.

However, charge transfer processes can also be electronically *nonadiabatic* if the ground and excited states become sufficiently close in energy or cross each other (i.e., a conical intersection) and are thus weakly coupled. Instead of a smooth MEP, the resulting nonadiabatic charge transfer

event exhibits an abrupt change and a cusp in the energy along the reaction coordinate, as shown with the dashed curves in Figure 1.4. In such cases, it is natural to work with *diabatic* electronic states. These states are not ground states but retain their chemical and physical character independent of the geometry. Nonadiabatic behavior is expected to occur in materials where large hopping distances must be traversed to achieve macroscopic charge transfer. This scenario exists in sulfur for hopping between S_8 rings.

1.3.4. Li Metal Anode Enabled by Sulfide Solid Electrolytes

A cycleable Li metal anode is needed to realize several high capacity battery concepts, such as Li-S or Li-air.[109] It is generally expected that use of a solid electrolyte (SE) would enable the implementation of a Li metal anode. Amongst the various SEs, sulfides are noteworthy because of their high ionic conductivities, low grain boundary resistances, and favorable mechanical properties.[110-111] Another desirable feature of SEs is the ability to resist charge injection from the electrodes. The role of an electrolyte in the battery is not only to shuttle the ionic components between electrodes, but also to force the electrons stay at the electrode and the external circuit.[10] This property has been related to the band gap of SEs[112], however the relative band edge positions of SEs with respect to electrochemical potentials in the electrode are more relevant to evaluate the tendency to undergo for charge injection by reduction, or charge extraction from oxidation.

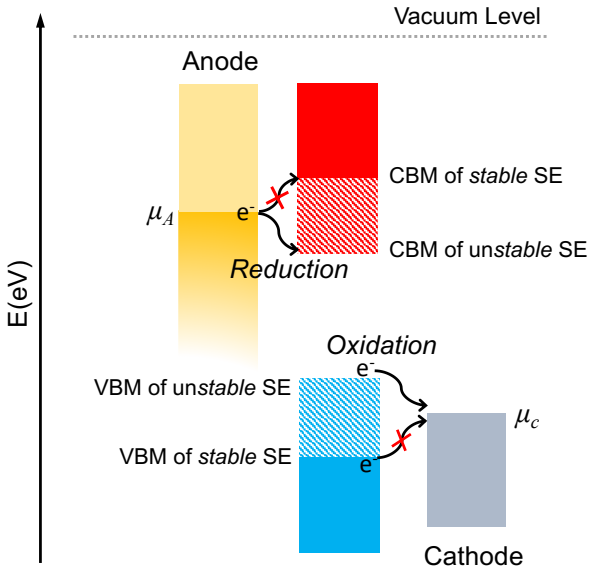

Figure 1.5 Schematic showing the electrochemical energy levels in the electrodes and the band edge positions of a solid electrolyte.

Figure 1.5 illustrates the relative energy levels of electrons in the electrode and the conduction band minimum (CBM) and the valence band maximum (VBM) of a solid electrolyte.[113] If the CBM is higher than the electrochemical potential of the anode (e.g. the Li/Li^+ level, μ_A =-1.39 eV vs. the vacuum level)[114], then no electron injection from anode into the electrolyte will occur due to the energy barrier (a.k.a. *Schottky barrier*).[115] A band alignment that fosters charge injection is known as an *Ohmic contact*.[115] Conversely, if the position of the CBM and μ_A are reversed, then undesirable electron transfer from anode to the solid electrolyte will occur, corresponding to reduction of the electrolyte by the anode. Similarly, at the interface with the cathode, if the valence band maximum (VBM) of the SE is lower in energy than the electrochemical potential of cathode (e.g. μ_C), hole injection into the SE (e.g. electron injection to the cathode from the electrolyte) is thermodynamically unfavored. If the energetic ordering of these levels is reversed, then the cathode will oxidize the electrolyte, resulting in hole injection into the SE. These undesirable charge transfers can stimulate the self-discharge or short circuiting of the battery by introducing electronic charge carriers into the SE. These processes indicate that the relative position of band edges relative to the electrochemical potentials of the electrodes is important for predicting the performance and stability of a solid electrolyte; the size of a SE's bandgap on its own is insufficient to predict a tendency to undergo these failure modes.

Another stability concept that is important for solid electrolytes concerns their chemical stability as a function of Li chemical potential. The chemical stability window is the potential range where the SE and electrode materials more stable (have a lower free energy) than the competing decomposed phases formed from chemical reactions involving the SE and/or electrodes. Chemical stability is calculated from the Li grand potential phase diagram.[116] The electron transfer reactions described in the preceding paragraph may be considered to be an initial step in a more extensive reaction cascade resulting in decomposition of the SE in the interfacial region. Chemical decomposition involves significant mass transfer, and may be kinetically limited. In these cases the aforementioned charge transfer reactions may dominate. In addition, even if chemical decomposition does occur, charge transfer through this phase may still occur via tunneling if the interphase that is formed is thin. Therefore, a complete understanding of SE stability can be achieved by considering both charge transfer and chemical stability.[10, 113, 117]

1.4. Goals and Scope of Thesis

As described in section 1.3., the challenges still remain, and they need to be addressed to urge the commercialization of Li-S batteries. Most previous studies on Li-S batteries have focused on experimental approaches for enhancing the cycleability and the capacity of the cell by engineering the electrolytes or the cathode supports. This thesis aims to explore the underlying mechanisms of the challenges to enrich the knowledge on Li-S batteries by density functional theory (DFT)-based atomistic modeling.

I first calculated the thermodynamic, electronic, and surface properties of redox-end members in Li-S batteries to provide the phase stability, electronic structure, and the morphology information (Chapter 3). In order to address the polysulfide dissolution, we adopted new class of adsorption material, metal-organic frameworks (MOFs), at the cathode of Li-S and test their ability to anchor the polysulfide species from dissolution (Chapter 4). The prerequisite to mitigate the charge transport limitation is to understand the charge transport mechanism of insulating charge/discharge product of Li-S battery, Li_2S and S_8, and it was accessed by considering point defects and their migrations (Chapter 5). Finally, we tested the interfacial stability between sulfide type solid electrolytes and Li metal anode by considering their band edge positions (Chapter 6)

Chapter 2 Methods

2.1. Many-body Problem

The majority of properties of materials are determined by the interactions among electrons and nuclei. The behaviors of electrons and nuclei are governed by the time dependent Schrödinger Equation:

$$i\hbar \frac{d\Psi}{dt} = \hat{H}\Psi \tag{2.1}$$

where, $\hbar$ is the reduced Planck constant, $\Psi = \Psi(x,t)$ is the many-body wavefunction, and H is the Hamiltonian operator. Within the time independent assumption, the wavefunction is a function of the coordinates of electrons $\mathbf{r}_i$ and nuclei $\mathbf{R}_i$:

$$\Psi = \Psi(\mathbf{r}_1, \mathbf{r}_2, \ldots, \mathbf{r}_\mathrm{N}; \mathbf{R}_1, \mathbf{R}_2, \ldots \mathbf{R}_\mathrm{M}). \tag{2.2}$$

However, the extreme complexity of the Schrödinger Equation precludes its analytic solution, so many attempts to simplify the equation have been made. One simplification proposed by Born and Oppenheimer (BO) utilizes the fact that the mass difference (approximately 1000 times) between nuclei and electrons is large, so the motion of electrons are much faster than that of nuclei, so one can consider nuclei are relatively stationary. So, we only need to consider the electronic part of Hamiltonian quantum mechanically, while the nuclei are treated as classical particles. Then, the wave function can be reduced to:

$$\Psi=\Psi(\mathbf{r}_1,\mathbf{r}_2, \ldots,\mathbf{r}_\mathrm{N}) \tag{2.3}$$

This excludes the kinetic energy of nuclei and nuclei-nuclei interactions from the Hamiltonian, so the time independency and BO approximation reduce Schrödinger Equation into an eigenvalue problem only related to electron wave functions:

$$\hat{H}\Psi = E\Psi \tag{2.4}$$

Although this approximation reduces the dimension of the problem from 3(N+M) to 3N, the equation is still unsolvable for practical system. One of the most widely used approximations is density functional theory (DFT)[118] because it can effectively and accurately calculate the electronic structure of the ground state.

2.2. Density Functional Theory

The DFT was first introduced by Pierre Hohenberg and Walter Kohn in 1964 and the two theorems stated by them constitute a fundamental of DFT.[118] Walter Kohn and Lu Jeu Sham have further developed two theorems and establish formalism finding the ground state energy.[119] The most significant challenge of DFT is the reasonable approximation of exchange-correlation functionals. In this section, we introduce the heart of DFT, Hohenberg-Kohn (HK) theorems, and show how the Kohn-Sham formalism is derived from them. In addition, the exchange-correlation functional approximations that are used in this study are also discussed.

2.2.1. Hohenberg-Kohn Theorems

The main idea of DFT is to treat the interacting electrons as non-interacting particles that are moving in an effective potential that can manifest the behavior of interacting electrons. This mapping can significantly reduce the dimension of the wavefunction and charge density from 3N to 3, so they are viable calculations with modern computing;

$$\Psi(\mathbf{r}_1,\mathbf{r}_2,\ldots,\mathbf{r}_N) \rightarrow \psi(\mathbf{r}) \tag{2.5}$$

The first theorem stated by HK is that there is a unique one-to-one mapping between an external potential, $V_{\text{ext}}(\mathbf{r})$, and the ground state charge density, $n(\mathbf{r})$. This is because the external potential determines the Hamiltonian, in turn, the wavefunction, ψ, and charge density, $n(\mathbf{r})$, of the system. HK showed the uniqueness of the mapping with a process of *reductio ad absurdum,* by showing the statement "*Another potential* $V'_{\text{ext}}(\mathbf{r})$*, with ground state* ψ' *gives rise to the same density* $n(\mathbf{r})$" is wrong.[118]

The second HK theorem is that there is a universal functional associated with kinetic and interaction energy, $F[n(\mathbf{r})]$, and with an aid of this functional, we can define the energy functional, $E[n]$, whose global minimum is the ground state energy for a given external potential, $V_{\text{ext}}(\mathbf{r})$.[118]

$$F[n(\mathbf{r})] \equiv (\psi, (T+U)\psi) \tag{2.6}$$

$$E[n(\mathbf{r})] \equiv \int V_{\text{ext}}(\mathbf{r})n(\mathbf{r})d\mathbf{r} + F[n(\mathbf{r})] \tag{2.7}$$

The energy E is assumed to be minimum at the ground state density $n(\mathbf{r})$ that satisfies the condition:

$$\int n(\mathbf{r})d\mathbf{r} = N \tag{2.8}$$

where N is the number of electrons in the system. The minimum energy functional can be easily calculated if the universal functional $F[n(\mathbf{r})]$ is a known and sufficiently simple functional, so the determination of the universal functional is the key part of the complexity of the many-body problem.

2.2.2. Kohn-Sham formulation

The universal functional $F[n(\mathbf{r})]$ consists of the many-body kinetic energy T and the mutual Coulomb repulsion U. In the Kohn-Sham formulation, we can write $F[n(\mathbf{r})]$ in terms of the kinetic energy of non-interacting electrons $T_0[n(\mathbf{r})]$, the classical Columbic interaction $E_H[n(\mathbf{r})]$, and all remaining many-body contributions, frequently called as the *exchange* and *correlation* energy $E_{\text{XC}}[n(\mathbf{r})]$.[119]

$$E[n(\mathbf{r})] \equiv \int V_{\text{ext}}(\mathbf{r})n(\mathbf{r})d\mathbf{r} + T_0[n(\mathbf{r})] + E_{\text{H}}[n(\mathbf{r})] + E_{\text{XC}}[n(\mathbf{r})] \tag{2.9}$$

Here,

$$T_0[n(\mathbf{r})] = -\frac{\hbar^2}{2m_e}\sum_{i=1}^{N}\int \psi_i^*\nabla^2\psi_i d\mathbf{r} \tag{2.10}$$

$$E_{\text{H}}[n(\mathbf{r})] = \frac{1}{2}\int\int \frac{n(\mathbf{r})n(\mathbf{r}')}{|\mathbf{r}-\mathbf{r}'|}d\mathbf{r}d\mathbf{r}' \tag{2.11}$$

The wavefunctions are unique functionals of the charge density, so the kinetic energy of non-interacting electrons is also a unique functional of $n(\mathbf{r}) = \sum_{i=1}^{N}\psi_i^*(r)\psi_i(r)$. The ground state energy of $E[n(\mathbf{r})]$ can be calculated by minimizing the Lagrange function subject to the wave function orthonormality constraint $\left(\int \psi_i^*\psi_j d\mathbf{r} = \delta_{ij}\right)$. This yields the Kohn-Sham equation;

$$\left[-\frac{\hbar^2}{2m_e}\nabla^2 + V_{\text{ext}}(\mathbf{r}) + V_{\text{H}}[n(\mathbf{r})] + V_{\text{XC}}[n(\mathbf{r})]\right]\psi_i(\mathbf{r}) = \varepsilon_i\psi_i(\mathbf{r}) \tag{2.12}$$

Here,

$$V_{\text{H}} = \frac{\delta E_{\text{H}}[n(\mathbf{r})]}{\delta n(\mathbf{r})} = \int \frac{n(\mathbf{r}')}{|\mathbf{r}-\mathbf{r}'|}d\mathbf{r}' \tag{2.13}$$

$$V_{\text{XC}} = \frac{\delta E_{\text{XC}}[n(\mathbf{r})]}{\delta n(\mathbf{r})} \tag{2.14}$$

The equation (2.10) can be also achieved by solving a set of single-particle Schrödinger equations of non-interacting electrons moving in the effective potential of $V_{\text{eff}}[n(\mathbf{r})]$;

$$\left[-\frac{\hbar^2}{2m_e}\nabla^2 + V_{\text{eff}}[n(\mathbf{r})]\right]\psi_i(\mathbf{r}) = \varepsilon_i\psi_i(\mathbf{r}). \tag{2.15}$$

Here,

$$V_{\text{eff}}[n(\mathbf{r})] = V_{\text{ext}}(\mathbf{r}) + V_{\text{H}}[n(\mathbf{r})] + V_{\text{XC}}[n(\mathbf{r})]. \tag{2.16}$$

The most crucial part in the Kohn-Sham equation is the appropriate approximation of the *exchange-correlation* (XC) energy because its exact functional dependence on $n(\mathbf{r})$ is still unknown. The following sections will deal with the effective approximation of the XC energy functional.

2.2.3 Exchange-Correlation (XC) functional

This section deals with the various classes of XC energy approximation schemes that were used in this study, namely, the local-density approximation, generalized gradient approximation, van der Waals augmented DFT (vdW-DF), DFT+U, and hybrid functionals. The XC energy can be expressed in terms of the XC energy functional per electron, ε_{xc};

$$E_{\text{XC}} = \int n(\mathbf{r})\varepsilon_{\text{xc}}[n(\mathbf{r})]\, d\mathbf{r} \tag{2.17}$$

For simplicity, the assumption holds that the functionals are non-spin-polarized (except DFT+U), but generalization to spin-polarized calculations is straight forward.[120]

LDAs. The simplest form of XC energy functional is the local-density approximation (LDA). In this approximation, $\varepsilon_{\text{xc}}^{\text{LDA}}[n(\mathbf{r})]$ only depends on the local density of a homogeneous electron

gas (HEG) having density $n(\mathbf{r})$. The exchange contribution of HEG, $\varepsilon_{\mathrm{X}}^{\mathrm{LDA}}$, is analytically known and the correlation part $\varepsilon_{\mathrm{C}}^{\mathrm{LDA}}$ is determined by fitting parameterized models (Vosko-Wilk-Nusair[121], Perdew-Zunger,[122] and Perdew-Wang[123]) to the energy of the HEG determined by quantum Monte Carlo simulations[124] and to analytic high/low density limits. The LDA provides accurate predictions of atomic structure, elastic, and vibrational properties of a wide variety of materials. Nevertheless, it still has deficiencies in estimating the energetics of chemical reactions and phase ordering in both bulk and molecular systems.[120, 125-126]

GGAs. The generalized gradient approximation (GGA) is one practical improvement on the LDA.[120] Unlike the LDA, the GGA employs not only the local density, but also the density gradient as additional ingredients, so the GGA XC functional is dependent on $n(\mathbf{r})$ and $\nabla n(\mathbf{r})$; $\varepsilon_{\mathrm{XC}}^{\mathrm{GGA}}[n(\mathbf{r});\ \nabla n(\mathbf{r})]$. Among the many GGA functionals, [127-135] one of the most widely used functionals is the one proposed by Perdew, Burke, and Ernzerhof.[136] This functional can be expressed as:

$$E_{\mathrm{XC}}^{\mathrm{PBE}}[n(\mathbf{r});\ \nabla n(\mathbf{r})] = E_{\mathrm{X}}^{\mathrm{PBE}}[n(\mathbf{r});\ \nabla n(\mathbf{r})] + E_{\mathrm{C}}^{\mathrm{PBE}}[n(\mathbf{r});\ \nabla n(\mathbf{r})]. \tag{2.18}$$

Here, the exchange energy, $E_{\mathrm{X}}^{\mathrm{PBE}}$, is,

$$E_{\mathrm{X}}^{\mathrm{PBE}}[n(\mathbf{r});\ \nabla n(\mathbf{r})] = \int n(\mathbf{r})\varepsilon_{\mathrm{X}}^{\mathrm{LDA}}[n(\mathbf{r})]F_{\mathrm{X}}(r_{\mathrm{s}}, s\{\nabla n(\mathbf{r})\})\, d\mathbf{r} \tag{2.19}$$

where, the uniform density is $\varepsilon_{\mathrm{X}}^{\mathrm{LDA}} = -3e^2k_F/4\pi$ and the enhancement factor, F_{X}, is,

$$F_{\mathrm{X}}(r_{\mathrm{s}}, s) = 1 + \kappa - \frac{\kappa}{1 + \mu s^2/\kappa} \tag{2.20}$$

where, r_{s} is the local Seitz radius $(n = 3/4\pi r_{\mathrm{s}}^2 = k_{\mathrm{F}}^3/3\pi^2)$, $s = |\nabla n|/2k_{\mathrm{F}}n$ is a dimensionless density gradient, $\mu = \beta(\pi^2/3) \cong 0.219$ is the effective gradient coefficient for exchange, and $\kappa = 0.804$ is a general coefficient that satisfies the linear response of uniform electron gas and The Lieb-Oxford bound. β is approximately 0.066725 which is calculated from the generalized expansion of gradient contribution.[136] The correlation energy can be written as:

$$E_{\mathrm{C}}^{\mathrm{GGA}}[n(\mathbf{r});\ \nabla n(\mathbf{r})] = \int n(\mathbf{r})\left[\varepsilon_{\mathrm{C}}^{LDA}\big(n(\mathbf{r})\big) + H(r_{\mathrm{s}}, t\{\nabla n(\mathbf{r})\})\right] d\mathbf{r}. \tag{2.21}$$

The gradient contribution, H, that satisfies the slowly varying, rapidly varying, and the high-density limits can be satisfied by

$$H(r_s, t\{\nabla n(\mathbf{r})\}) = \frac{e^2\gamma}{a_0} \ln\left\{1 + \frac{\beta}{\gamma} t^2 \left[\frac{1 + At^2}{1 + At^2 + At^4}\right]\right\} \tag{2.22}$$

where,

$$A = \frac{\beta}{\gamma}\left[\exp\left(-\frac{\varepsilon_c^{LDA}}{\gamma e^2}\right) - 1\right]^{-1}. \tag{2.23}$$

$t = |\nabla n|/2k_S n$ is another dimensionless density gradient, where $k_S = \sqrt{4k_F/\pi a_0}$ is the Thomas -Fermi wave screening wave number ($a_0 = \hbar^2/me^2$) and $\gamma = (1 - \ln 2)/\pi^2$. The GGA functionals can predict the properties of single molecules and condensed matter very well,[137-138] but they poorly describe van der Waals (vdW) interactions which are long-ranged and non-local contributions.

Table 2.1 The list of vdW-DF methods and the form of the corresponding exchange energy or enhancement factor with a appropriate parameter settings

Method	Exchange energy (enhancement factor)	Parameter setting
PBE[138]	$F_X^{\mathrm{PBE}} = 1 + \kappa - \frac{\kappa}{1 + \mu s^2/\kappa}$	$\kappa = 0.804$ $\mu = 0.219$
rev-PBE[142]	$F_X^{\mathrm{revPBE}} = 1 + \kappa - \frac{\kappa}{1 + \mu s^2/\kappa}$	$\kappa = 1.245$ $\mu = 0.219$
optPBE[145]	$E_X^{\mathrm{optPBE}} = xE_X^{\mathrm{PBE}} + (1 - x)xE_X^{\mathrm{revPBE}}$	$x = 0.9452$ $\kappa = 1.048$ $\mu = 0.175$
optB88[145]	$F_X^{\mathrm{optB88}} = 1 + \frac{\mu s^2}{1 + \beta s\ \mathrm{arcshinh}(cs)}$	$c = 2^{4/3}(3\pi^2)^{1/3}$ $\mu = 0.22$ $\beta = \mu/1.2$
optB86b[143]	$F_X^{\mathrm{optB86b}} = 1 + \frac{\mu s^2}{(1 + \mu s^2)^{4/5}}$	$\mu = 0.1234$
vdW-DF2[144]	$F_X^{\mathrm{vdW-DF2}} = (1 + 15as^2 + bs^4 + cs^6)^{1/15}$	$a = 0.0864$ $b = 14$ $c = 0.2$
rev- vdW-DF2[146]	$F_X^{\mathrm{rev-\ vdW-DF2}} = 1 + \frac{\mu s^2}{(1 + \mu s^2)^{4/5}}$	$\mu = 0.7114$

vdW-DF. The vdW augmented DFT (vdW-DF)[139] describes covalent and vdW interactions within the DFT framework by adding a non-local interaction correlation energy to the sum of the LDA correlation energy and the GGA exchange energy,

$$E_{\mathrm{XC}}^{\mathrm{vdW}} = \int n(\mathbf{r})\varepsilon_{\mathrm{X}}^{LDA}[n(\mathbf{r})]F_{\mathrm{X}}[s(\mathbf{r})]\,d\mathbf{r} + \int n(\mathbf{r})\varepsilon_{\mathrm{C}}^{LDA}[n(\mathbf{r})]\,d\mathbf{r} + E_{\mathrm{C}}^{nl}, \tag{2.24}$$

where,

$$E_{\mathrm{C}}^{nl} = \frac{1}{2}\int\int d\mathbf{r}d\mathbf{r}'\mathrm{n}(\mathbf{r})\phi(d,d')\mathrm{n}(\mathbf{r}'). \tag{2.25}$$

The vdW kernel $\phi(d,d')$ which is a function of $n(\mathbf{r})$ and $|\nabla n(\mathbf{r})|$ determines the long range interactions and the short-range damping. Since vdW correlation energies only rely on the charge density and its gradient, the additional computation is marginal. The choice of LDA correlation functional prevents the double counting the gradient contribution in E_{C}^{nl}, because the uniform electron density condition cancels the LDA correlation effect from E_{C}^{nl}.[139] The accuracy of vdW-DF is influenced by the choice of enhancement factor and the corresponding exchange functional. Table 2.1 summarizes the widely used vdW-DF methods[140-144] and their combinations of GGA exchange energy (enhancement factor) and associated parameters. The enhancement factor of the PBE functional is listed first as a reference.[136]

DFT+U. Nominally-localized (correlated) d or f elections are incorrectly delocalized with semi-local (LDA or GGA) calculations on transition metal containing systems. This error can be mitigated by adding an energy penalty to the regular DFT energy to localize the electrons.[145] The energy penalty can be determined by the rationally simplified invariant that is associated with the effective on-site Coulomb- and exchange parameters, *U* and *J*:[146]

$$E_{\mathrm{DFT+U}} = E_{\mathrm{DFT}} + \frac{(U-J)}{2}\sum_{\sigma}\left(n_{m,\sigma} - n_{m,\sigma}^2\right). \tag{2.26}$$

The occupation number of the m th d or f state is denoted by $n_{m,\sigma}$ and σ is the spin state. In this approach, the energy difference between *U* and *J* matters and they are determined by empirical manners.

Hybrid Functionals. A drawback of semi-local GGA functionals and vdW-DF methods is their underestimation of band gaps with respect to experiments. This error can be reduced to some extent by including Hartree-Forck (HF) energy to XC energy. The calculation of HF energy

enormously increases the computational cost; however, the inclusion of exact exchange addresses the incorrect delocalization of electrons due to self-interaction error such as in the case of transition metals. Heyd, Scuseria, and Ernzerhof (HSE) proposed a XC functional of[147-148],

$$E_{\mathrm{XC}}^{\mathrm{HSE}} = \alpha E_{\mathrm{X}}^{\mathrm{HF,SR}}(\omega) + (1-\alpha)E_{\mathrm{X}}^{\mathrm{PBE,SR}}(\omega) + E_{\mathrm{X}}^{\mathrm{PBE,LR}}(\omega) + E_{\mathrm{C}}^{\mathrm{PBE}}. \quad (2.27)$$

Here, $E_{\mathrm{X}}^{\mathrm{HF,SR}}$ is the short-range HF energy and $E_{\mathrm{X}}^{\mathrm{PBE,SR}}$ and $E_{\mathrm{X}}^{\mathrm{PBE,LR}}$ represent short- and long-range PBE exchange energies, respectively. The correlation energy is determined by the PBE functional, $E_{\mathrm{C}}^{\mathrm{PBE}}$. The mixing parameter, α, decides the portion of HF energy and the screening parameter, ω, defines the separation range. The screening parameter of 0.2Å works well for solids,[147, 149] but the mixing parameter is somewhat arbitrarily determined to 0.25 in the HSE06 functional.[149] The mixing parameter is frequently tuned by fitting the band gaps calculated by hybrid functionals with various α values to that determined by the higher order calculations based on *GW methods*.[99, 102, 150-153]

2.2.3. Quasi-particle GW methods

The band-gap calculated by hybrid functionals, while improved relative to predictiosn from local and semi-loal functionals, still underestimates experiments. This is because ground state DFT calculations cannot accurately predict the excited state. Alternatively the quasi-particle concept and a Green's function method can be incorporated to close the gap between DFT calculated and experimentally observed band gaps.[154-156] Coulomb repulsion causes a negative charge depletion adjacent to a given electron and the ensemble between this electron and the positive screening charge around it forms a quasiparticle. [155] The XC energy term in the Kohn-Sham equation is replaced by the many-body self-energy operator, **Σ**;

$$\left[-\frac{\hbar^2}{2m_e}\nabla^2 + V_{\mathrm{ext}}(\mathbf{r}) + V_{\mathrm{H}}[n(\mathbf{r})]\right]\psi_i(\mathbf{r}) + \int \sum(\mathbf{r},\mathbf{r}';\varepsilon_i)\,\psi_i(\mathbf{r}')d\mathbf{r}' = \varepsilon_i\psi_i(\mathbf{r}). \quad (2.28)$$

The self-energy operator is also a function of energy, so its mathematical expression is much more complicated than for local or semi-local XC energy functionals. This makes the quasi-particle calculations even more expensive than for a hybrid functional. The self-energy operator can be approximated by the single-particle Green function, *G*, and be expanded linearly by the screened Coulomb interaction, *W*;

$$\sum \approx GW. \quad (2.29)$$

The detailed description of the self-energy operator can be found in the literature.[155] This operator is expressed by its wavefunction, so the problem can be solved self-consistently. The wavefunctions and corresponding eigenvalues can be used to update the G or W, but due to the high computational cost, an effective strategy for how to update the parameters is required. Several approaches are implemented in the Vienna *ab initio* simulation package (VASP),[157-160] which is adopted in the present study.

Chapter 3 Properties of Redox-End Members in Li-S Batteries

3.1. Introduction

In this chapter, first principles calculations are used to close some of the knowledge gaps mentioned above by predicting key thermodynamic and electronic properties of several solid-phase redox end members present in lithium-sulfur batteries. The phases examined include: Li, (hypothetical) Li_2S_2, Li_2S, α-Sulfur, and β-Sulfur. A variety of computational methods were employed, including: density functional theory (DFT) with semi-local functionals, van der Waals augmented DFT (vdW-DF), quasi-particle methods (G_0W_0), and continuum solvation techniques. First, optimized crystal structures were characterized in a comparative fashion using multiple van der Waals-aware density functionals. The vdW-DF method using the optB88 functional for electron exchange was found to yield the best agreement with experimental lattice constants and bulk moduli. The stability of the α allotrope of sulfur at low temperatures was confirmed by revisiting the sulfur phase diagram. Similarly, the stability of lithium persulfide, Li_2S_2, was assessed by comparing the energies of several hypothetical A_2B_2 crystal structures. We find that Li_2S_2 is unstable with respect to a two-phase mixture of Li_2S and α-S, suggesting that Li_2S_2 is a metastable phase. Regarding surface properties, the stable surfaces and equilibrium crystallite shapes of Li_2S and α-S were predicted in the presence and absence of a continuum solvation field intended to mimic the presence of the common electrolyte solvent, dimethoxyethane (DME). In the case of Li_2S, the equilibrium crystallites are comprised entirely of stoichiometric (111) surfaces, while for α-S a complex mixture of several facets are predicted. Finally, G_0W_0 calculations reveal that all of α-S, β-S, Li_2S, and Li_2S_2 are insulators with bandgaps greater than 2.5 eV.

3.2 Methods

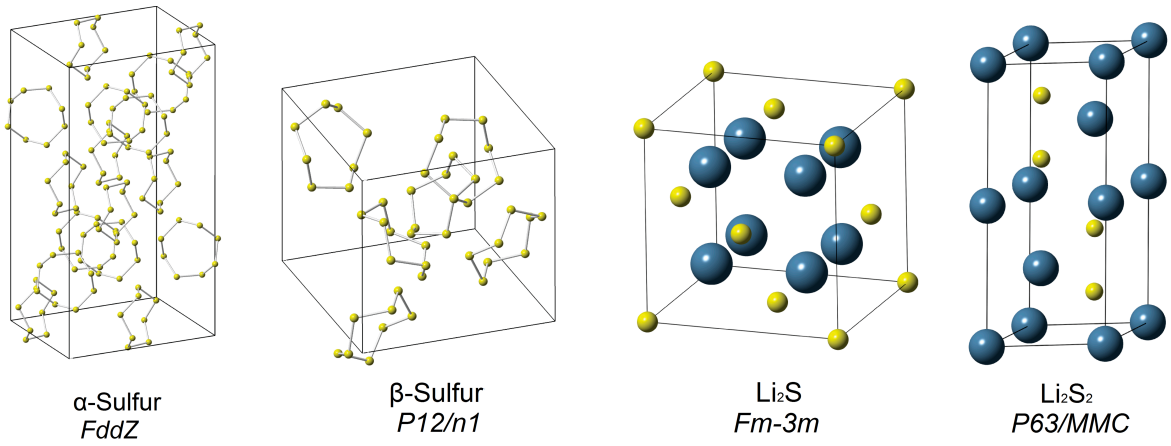

Figure 3.1 Crystal structures and respective space groups for α-Sulfur, β-Sulfur, Li_2S, and the lowest-energy structure for Li_2S_2. Blue and yellow spheres represent lithium and sulfur atoms, respectively.

First principles calculations were performed using the Vienna *ab initio* simulation package (VASP).[161-162] Five compounds were considered: BCC Li (2 atoms in the unit cell), Li_2S (3 atoms), Li_2S_2 (8 atoms), α-Sulfur (128 atoms) and β-Sulfur (48 atoms). Figure 3.1 displays the crystal structures and space groups of α-Sulfur, β-Sulfur, Li_2S, and Li_2S_2, the latter using the crystal structure that exhibits the lowest energy out of several possibilities (described below). Projector-augmented wave (PAW)[163-164] potentials were used to describe core-valence electron interactions. Valence states of *2s* were used for lithium and *3s3p* for sulfur. The planewave cutoff energy was set to 450eV; the Monkhorst-Pack[165] scheme for *k*-point sampling was used in combination with k-point meshes of: 12×12×12 (Li), 4×4×4 (Li_2S), 7×7×7 (Li_2S_2), 2×2×2 (α-S) and 2×2×2 (β-S). Two methods were used to treat exchange and correlation: (*i*.) the Perdew – Burke − Ernzerhof (PBE) generalized gradient approximation (GGA)[136] and, (*ii*.) van der Waals-augmented Density Functional Theory (vdW-DF).[139] Including van der Waals interactions is essential for describing the behavior of sulfur, as the crystal structure of both α and β allotropes consist of discrete, covalently bonded S_8 molecular units ("cycloocta") that interact through dispersion forces. Five different vdW-DF methods were tested: these include the so-called vdW-DF1 methods having exchange functionals based on revPBE[142], optPBE[145], optB88[145], optB86b[143], and also the vdW-DF2[144] method. Equilibrium cell volumes were determined by fitting energy-volume data to the Murnaghan equation of state.[166] Atom positions were relaxed to a force tolerance of 0.01eV/Å.

As previously mentioned, the existence of a persulfide phase, Li_2S_2, during discharge of a Li-S battery remains an open question. Such a phase does not appear in the equilibrium Li-S phase diagram, and its crystal structure is unknown. To examine the stability of a hypothetical Li_2S_2

phase we generated several candidate Li_2S_2 crystal structures using various A_2B_2 phases as structural templates. Here A represents an alkali metal (Li, Na, K, Rb) and B is a chalcogenide (O, S, Se). Seven structures were investigated by replacing A sites with Li and B sites with S. The template compounds included: Li_2O_2, Na_2S_2, K_2S_2, Na_2O_2, K_2O_2, Na_2Se_2 and Rb_2S_2. In all cases the unit cells (volume, shape, and atom positions) were relaxed using vdW-aware DFT.

Thermodynamic properties were evaluated within the harmonic approximation.[37] Vibrational frequencies ω_i were obtained using the direct method.[167] Vibrational contributions to the enthalpy (H_{vib}) and entropy (S_{vib}) are given by:[37]

$$H_{vib}(T) = \sum_{i}^{3N-3} \frac{1}{2}\hbar\omega_i + \hbar\omega_i \left[\exp\left(\frac{\hbar\omega_i}{k_B T}\right) - 1\right]^{-1} \tag{3.1}$$

$$S_{vib}(T) = \sum_{i}^{3N-3} \frac{\hbar\omega_i / k_B T}{\exp(\hbar\omega_i / k_B T)} + \ln\left[1 - \exp\left(-\frac{\hbar\omega_i}{k_B T}\right)\right] \tag{3.2}$$

where $\hbar$ is Plank's constant divided by 2π, k_B is the Boltzmann factor, and N refers to the number of atoms in the supercell. The enthalpy and Gibbs free energy are expressed as:

$$H(T) = H_{vib}(T) + E \tag{3.3}$$

$$G(T) = H(T) - S_{vib}(T)T \tag{3.4}$$

where E is the static (zero Kelvin) energy of a compound in its ground state.

To estimate electronic properties, the Heyd-Scuseri-Ernzerhof (HSE06) hybrid functional[149] and the non-self-consistent quasi particle G_0W_0 method[157] were used. In the case of G_0W_0 calculations, vdW-DF wave functions from an earlier self-consistent calculation were used as input. A Gamma point centered sampling scheme with 1×1×1(α, β-S), 4×4×4 (Li_2S) and 7×7×7 (Li_2S_2) k-point meshes was used. The Gaussian smearing method was applied to obtain the Density of States (DOS); the band gap was estimated using energy differences between the lowest-occupied and highest unoccupied eigenvalues.

The surface energies of 38 distinct surfaces were evaluated. These included 31 Li_2S surfaces of varying stoichiometry[168] with Miller indices (100), (110), and (111). Each surface slab consisted of at least 9 Li/S planes; approximately 20Å of vacuum was included in each surface

supercell. For Li_2S surfaces, comparisons were made using the GGA and vdW-DF (optB88) functionals. In addition, 7 sulfur surfaces were considered, with indices of (100), (010), (001), (011), (110) and (111). These surfaces were comprised of at least 3 layers of cycloocta rings, and were constructed such that no S_8 rings were broken when the surface was cleaved. For sulfur surfaces only the vdW-DF method was used. The Monkhorst-Pack scheme was used for both Li_2S and sulfur surfaces with 4×4×1 and 1×1×1 *k*-point meshes, respectively.

The energies of Li_2S and S surfaces are given by:

$$\gamma_{Li_2S} = \frac{1}{2A}\left(G_{Li_2S}^{Slab} - N_{Li}\mu_{Li} - N_S\mu_S\right) \tag{3.5}$$

$$\gamma_S = \frac{1}{2A}\left(G_S^{Slab} - N_S\mu_S\right) \tag{3.6}$$

where G^{slab} is the energy of the surface slab, N_i is the number of atoms of type i in the slab, and μ_i is the corresponding chemical potential. In the case of the Li_2S surface, the surface energy can be written in terms of the energy per formula unit of bulk Li_2S, $g_{Li_2S}^{Slab}$, and the chemical potential of sulfur:

$$\gamma_{Li_2S} = \frac{1}{2A}\left[G_{Li_2S}^{Slab} - N_{Li}g_{Li_2S}^{Slab} + \left(\frac{1}{2}N_{Li} - N_S\right)\mu_S\right]. \tag{3.7}$$

As the chemical potential of sulfur is not precisely known, surface energies were evaluated for a range of μ_S given by: $E(Li_2S) - 2\mu_{Li}$(BCC Li) $\leq \mu_S \leq \mu_S$(α-S). Here, $E(Li_2S)$ is the total energy of a Li_2S formula unit, μ_{Li}(BCC Li) is the energy per atom of BCC Li, and μ_S(α-S) refers to the same for an atom of α-S.

Cycling of a Li-S battery should result in the repeated nucleation and growth of solid phase sulfur (charging) and Li-S particles (discharging). As these processes occur in the presence of a liquid electrolyte, the relevant "surface" energies are not solid/vacuum surface energies – as is typically assumed in atomistic studies – but rather solid electrode/liquid electrolyte interface energies.

To explore the impact of solvation on surface energies, comparisons were made with and without a continuum solvation field (VASPsol)[169-170] In these calculations the dielectric constant was set to that of dimethoxyethane (DME),[171] 7.55, as common electrolytes in Li-S batteries

employ solvents based on DME[20] or mixtures of DME and dioxolane[19, 29]. (The dielectric constant of dioxolane is similar to that of DME, 7.13.)

3.3 Results

3.3.1 Structure Analysis

Low energy structures of each redox-end member were evaluated in a comparative fashion using the GGA and 5 different vdW-DF methods. Turning first to the high-temperature β-sulfur phase, Figure 3.2 plots the total energy of the β-S unit cell as a function of cell volume. In contrast to the other functionals, which show a clear minimum in the energy *vs.* volume data, the curves calculated with the GGA and the revPBE-based vdW-DF1 functional monotonically decrease as volume increases. Such behavior might be expected from the GGA, where the neglect of vdW interactions between cycloocto rings is a known omission. However, in the case of vdW-DF1, vdW contributions are explicitly accounted for; hence the poor representation of energy-volume behavior is surprising. For this reason, the GGA and revPBE-based vdW-DF1 functionals were not used in subsequent structure calculations on S-based systems.

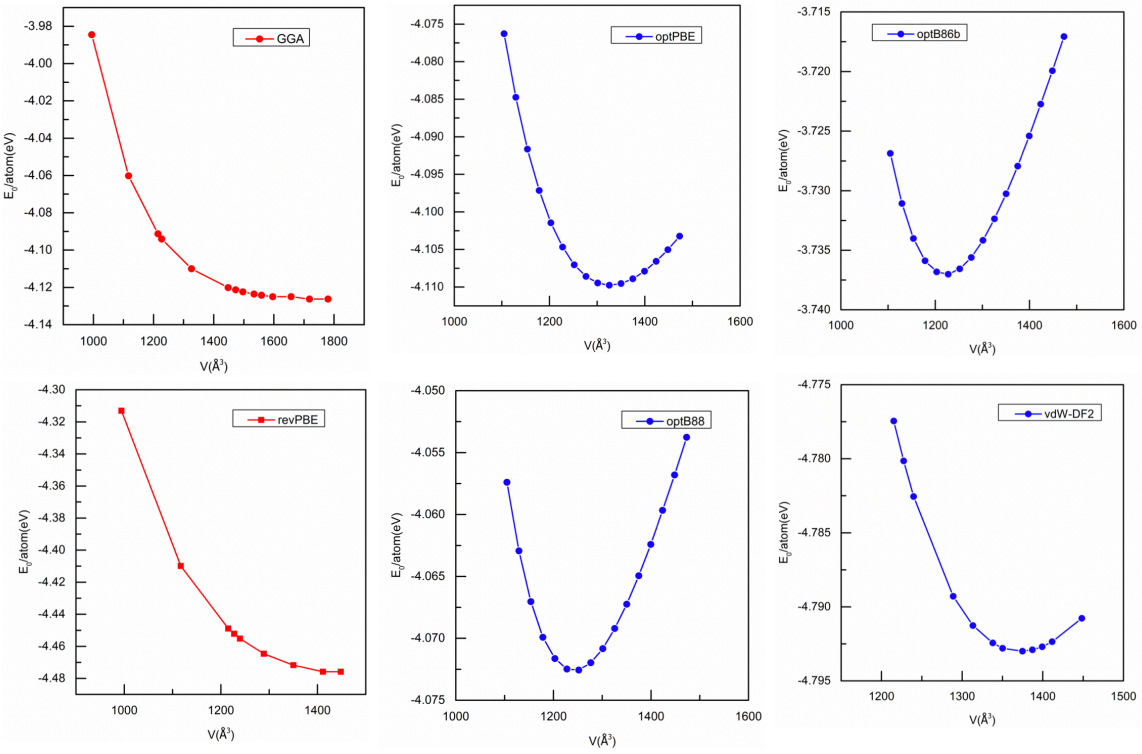

Figure 3.2 Energy per atom vs. volume data for β-S fitted to the Murnaghan equation of state using the GGA, revPBE-vdW-DF (vdW-DF1), optPBE-vdW-DF, optB88-vdW-DF, optB86b-vdW-DF, and vdW-DF2 methods.

Table 3.1 compares the calculated bulk modulus, lattice parameters, and cell volume of Li-S redox end members with experimental data. The optB88-vdW functional revealed the best for structural properties amongst 3 other functionals: optPBE-vdW, optB86b-vdW, and vdW-DF2. Typical deviations between theory and experiment were less than 1% for the optB88-vdW. The optB86b and optPBE-based functionals have slightly larger deviations (1-2%), whereas vdW-DF2 exhibits a range of 1-3%.

Table 3.1 Comparison of different vdW-DF methods to experimental data for the bulk modulus, lattice parameters, and cell volume for Li-S redox end members and BCC Li

	Functional	Bulk modulus (Gpa)	Lattice Parameters				Volume ($Å^3$)
			a (Å)	b (Å)	c (Å)	Angle (°)	
Li	GGA	13.83	3.44			90	40.61
	optPBE-vdW	13.60	3.42			90	40.10
	optB88-vdW	13.83	3.45			90	40.91
	optB86b-vdW	13.41	3.44			90	40.69
	vdW-DF2	15.02	3.38			90	38.49
	Experiment	12.90[172]	3.48[173]			90	43.24
Li_2S	GGA	42.22	5.72			90	187.50
	optPBE-vdW	42.14	5.72			90	187.28
	optB88-vdW	42.60	5.70			90	185.07
	optB86b-vdW	42.11	5.69			90	184.12
	vdW-DF2	41.32	5.75			90	190.60
	Experiment	45.70[174]	5.69[174]			90	184.22
β-S	optPBE-vdW	8.29	10.93	10.96	11.06	95.86	1318
	optB88-vdW	10.78	10.66	10.72	10.84	95.44	1233
	optB86b-vdW	10.16	10.58	10.65	10.80	95.22	1213
	vdW-DF2	10.52	11.11	11.09	11.19	95.98	1371
	Experiment	-	10.69[175]	10.72	10.81	95.75	1233
α-S	optPBE-vdW	8.35	10.61	13.10	24.90	90.00	3462
	optB88-vdW	11.26	10.33	12.76	24.45	90.00	3222
	optB86b-vdW	10.80	10.26	12.69	24.35	90.00	3171
	vdW-DF2	10.49	10.76	13.21	25.22	90.00	3587
	Experiment	14.50[176]	10.46[177]	12.87	24.49	90.00	3297

3.3.2 Thermodynamic properties

Figure 3.3(a) shows the convex hull for the Li-S system as a function of atomic percent lithium at 0 K using vdW-DF2 method. Amongst the various structure candidates considered for Li_2S_2, the one yielding the lowest energy was based on the hexagonal Li_2O_2 prototype (P63/MMC space group). This structure lies above the convex hull by approximately 67 meV/atom which is too large

to be stablized[178], and should therefore be metastable with respect to a two-phase mixture of S and Li_2S. The Li_2O_2 prototype for Li_2S_2 was used for calculations involving Li_2S_2 henceforth.

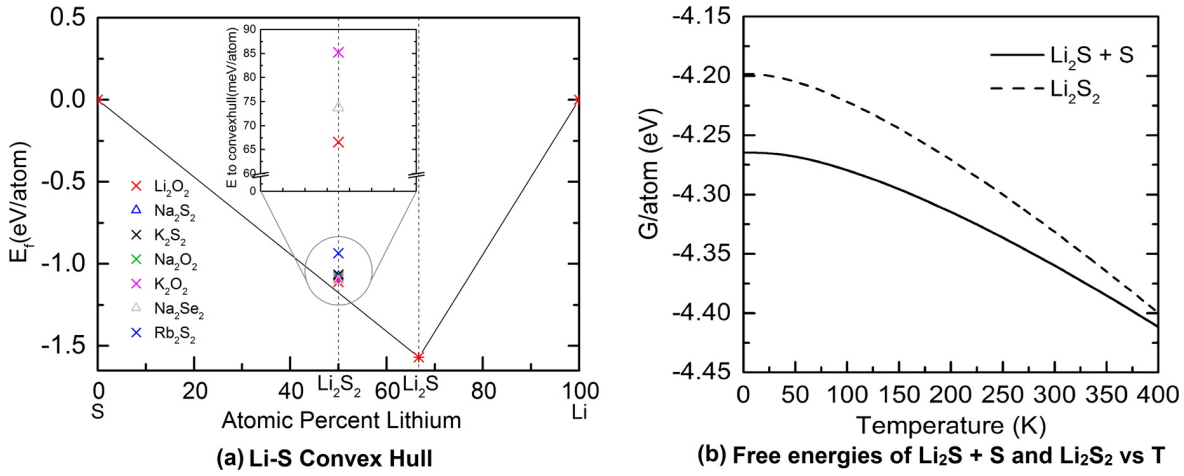

Figure 3.3 (a) Calculated convex hull for the Li-S system. The inset magnifies the energetic ordering of the different Li_2S_2 candidate phases above the hull. (b) Gibbs free energy of Li_2S + S vs. Li_2S_2 as a function of temperature.

Figure 3.3 (b) compares the Gibbs free energies of Li_2S_2 to the 2-phase mixture, Li_2S + α-S, as a function of temperature. Free energies were evaluated by combining the static electronic energy from the vdW-DF2 functional with vibrational contributions obtained from the optB88-vdW. For the entire temperature range considered (0 – 400 K), we find that the two-phase mixture of Li_2S and S has lower free energy than Li_2S_2. As previously mentioned, Li_2S_2 has not been successfully synthesized and does not appear in experimental phase diagrams[28]. The calculated thermodynamic data in Figure 2 is consistent with these observations. To aid in the identification of Li_2S_2 during discharge of Li-S batteries, Figure 3.4 plots the calculated XRD pattern for Li_2S_2 and compares to that of Li_2S. Li_2S has major peaks around 27°, 31°, 45° and 53°, which correspond well to experimental data.[29] On the other hand, the peaks of Li_2S_2 do not match data from recent experiments.[29, 179]

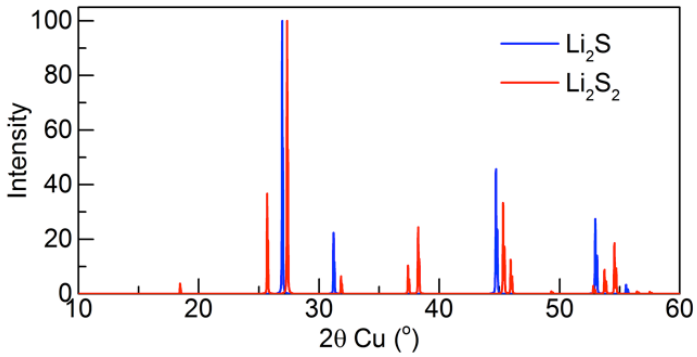

Figure 3.4 Calculated x-ray diffraction pattern for Li_2S and Li_2S_2

Table 3.2 Calculated cell potential ($E^{T=298}$), formation enthalpy ($\Delta H^{T=298}$), and Gibbs free energy of formation ($\Delta G^{T=298}$)for several vdW-DF methods compared with experimental data.

		$E^{T=298}$(V)	$\Delta H^{T=298}$(eV)	$\Delta G^{T=298}$ (eV)
Li_2S	optPBE	2.15	-4.35	-4.30
	optB88	2.20	-4.44	-4.40
	opt86b	2.10	-4.24	-4.19
	vdW-DF2	2.33	-4.70	-4.65
	Exp.	2.30[19]	-4.58[180]	-
Li_2S_2	optPBE	2.07	-4.10	-4.14
	optB88	2.13	-4.23	-4.27
	opt86b	2.04	-4.03	-4.07
	vdW-DF2	2.22	-4.40	-4.44
	Exp.	-	-	-

Table 3.2 summarizes the calculated redox potentials, formation enthalpies (ΔH), and formation free energies (ΔG) for Li_2S and Li_2S_2 at room temperature (298 K). Comparisons are made between different functionals by evaluating the static electronic energy with several vdW-DF methods. (Phonon frequencies were evaluated using the harmonic approximation and the optB88-vdW functional. We found that the optB88-vdW yields the expected number (3) of imaginary frequencies, whereas most of the other functionals did not.) The calculated ΔH values for Li_2S are in good agreement with experimental data, with an error range of 1 to 6%. The vdW-DF2 method yielded energies that were closest to experiment. For example, the calculated cell potential at 298K was found to be similar to the experimental cell voltage at the upper plateau of the discharge curve[19]. To the best of our knowledge, experimental data for ΔG for Li_2S and Li_2S_2, and ΔH for Li_2S_2, have not been reported. The formation energy data presented in Table 3.2 is consistent with the thermodynamic analysis presented in Figure 3.3: Li_2S is predicted to have a

more negative formation enthalpy/free energy than Li_2S_2 by ~0.1eV at room temperature, suggesting that Li_2S_2 generated during battery discharge should transform via a non-electrochemical pathway to a mixture of Li_2S and S. The transformation of Li_2S_2 to Li_2S via the reaction $Li_2S_2 + 2Li \rightarrow 2Li_2S$ could also be limited in the event that the reaction is starved of Li.

Regarding the phase diagram for elemental sulfur, recent experiments[19] have correlated reduced capacity fade (due to limited polysulfide shuttling) in Li-S batteries with the formation of β sulfur in the cathode. In bulk S the α phase is observed to be the stable phase at low temperatures, with a transition to the β phase at temperatures ranging from room temperature to slightly above.[18, 25, 55-56] Figure 3.5 plots the free energy difference, $G(\alpha\text{-S}) - G(\beta\text{-S})$, between the α and β allotropes of sulfur as a function temperature. The present calculations reproduce the stability trends observed in experiments, but underpredict the α/β transition temperature.

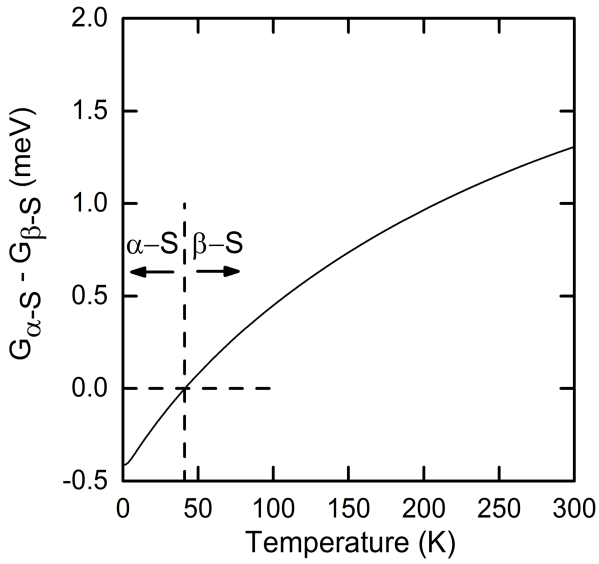

Figure 3.5 Calculated Gibbs free energy difference between α and β sulfur as a function of temperature.

3.3.3 Electronic Structure

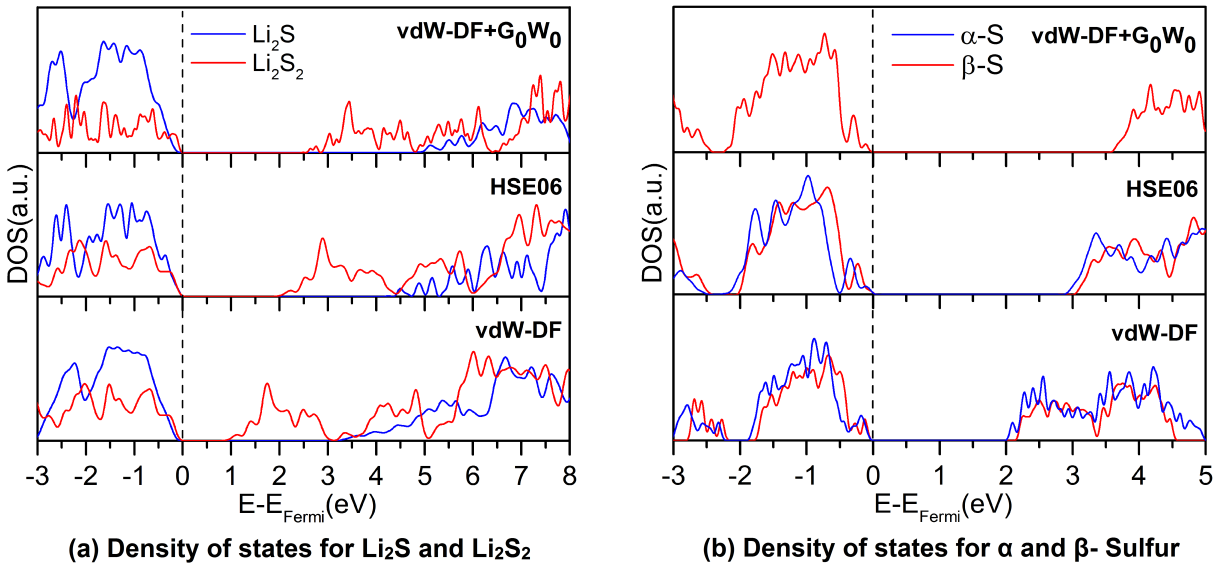

Figure 3.6 Density of states for (a) Li_2S and Li_2S_2, (b) α- and β-sulfur calculated using vdW-DF, HSE06 and vdW-DF+G_0W_0

Figure 3.6 plots the density of states (DOS) for Li_2S and Li_2S_2 (panel a), as well as for α-sulfur and β-sulfur (panel b). Several different calculation methods were compared: optB88-vdW-DF, HSE06, and G_0W_0. In the case of G_0W_0 calculations, optB88-vdW-DF wave functions were used as input; we refer to this approach as vdW-DF+G_0W_0. The DOS reveals that all of the compounds considered exhibit a sizeable bandgap. Furthermore, the DOS of the sulfur allotropes are quite similar in both shape and size of the gap. On the other hand the DOS of Li-S phases display some clear differences: for example, Li_2S_2 generally has a smaller gap than Li_2S, due to the presence of lower-lying states at the bottom of the conduction band.

Table 3.3 Calculated and experimental band gap of α, β-sulfur, Li_2S and Li_2S_2.

Method Type	Band gap			
	α - sulfur	β - sulfur	Li_2S	Li_2S_2
vdW-DF	2.20	2.34	3.46	1.07
HSE06	3.01	3.20	4.34	1.98
vdW-DF+G_0W_0	-	3.76	5.10	2.58
GGA+G_0W_0	-	-	5.11	2.70
Exp.	2.79[181], 2.61[182]	-	-	-

Table 3.3 summarizes the calculated band gaps and makes comparisons with experimental data. (The apparent gaps in Figure 3.6 appear somewhat smaller than the tabulated gaps in Table 3.3 due to the use of smearing in plotting the DOS.) Due to its large unit cell size (128 atoms), G_0W_0 calculations were not performed for α-sulfur. However, its value can be estimated based on comparisons with β-sulfur. We note that the band gaps of α and β sulfur are similar for vdW-DF and HSE06 calculations, with the gap for the β phase being larger by 0.1 to 0.2 eV. Assuming this trend holds, we can estimate the band gap for α-sulfur at the G_0W_0 level to be ~0.2 eV smaller than the corresponding value for β-sulfur, approximately 3.6 eV.

Table 3.3 shows that the calculated bandgap increases in going from the vdW-DF functional, to HSE06, to G_0W_0. Such behavior is consistent with generally known trends.[149, 160] G_0W_0 calculations based on GGA starting wavefunctions generally underestimate the experimental band gap.[160] In our calculations vdW-DF-based wavefunctions are used, which appears to result in an overestimate of the gap: in the case of the S allotropes the calculated gap of 3.6 – 3.76 eV at the G_0W_0 level is approximately 1 eV larger than the experimental values. This discrepancy could also be due to the molecular-crystal nature of sulfur.[182] We note that the temperature dependence of the sulfur band gap ($\approx$ 2meV/K)[182] is approximately 10 times higher than that of other semi-conductors (~0.1meV/K).[183] Our calculation is conducted at 0K, while the experimental values for the band gap are reported at 298K[181] and 279K[182], respectively. Accounting for this temperature dependence, the calculated band gap of sulfur at 298K ranges from 2.9 to 3.3 eV. This is in much better agreement with the measured values of 2.6 and 2.8 eV.

Regarding lithium sulfide, a prior study predicted the band gap of Li_2S to be 3.66 eV when using the GGA functional.[36] The band gap of 3.46 eV predicted here using vdW-DF is similar to that value. As expected,[23,40] the gap opens to 4.34 eV when using the HSE06 hybrid functional, and is largest for the vdW-DF+G_0W_0, 5.10 eV. These gaps indicate that Li_2S is an electronic insulator, a fact which could limit battery performance if charge transport through Li_2S is needed during charge or discharge.[20] To the best of our knowledge, an experimental value for the Li_2S band gap has not been reported.

3.3.4 Surface Energy

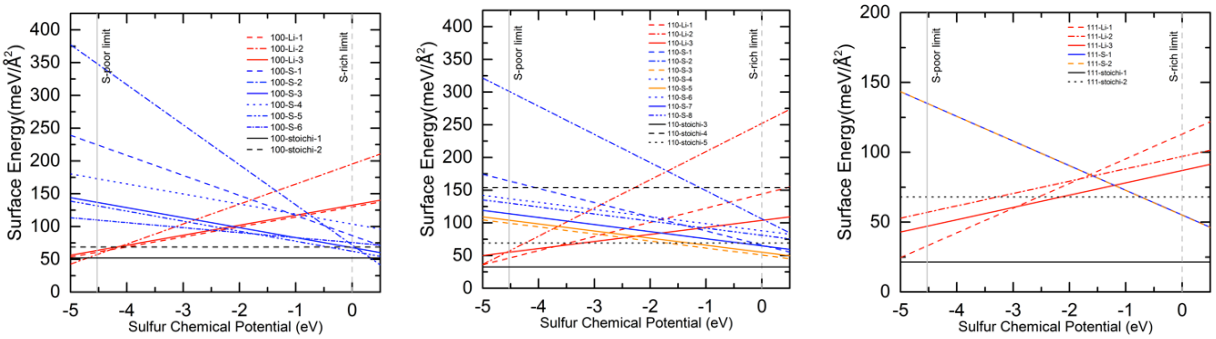

100-GGA 110-GGA 111-GGA

Figure 3.7 Calculated surface free energies for Li_2S as a function of sulfur chemical potential and surface normal using GGA functional. Vertical lines represent sulfur poor and rich limits to the S chemical potential.

Figure 3.7 shows the GGA free energies of 31 Li_2S surfaces as a function of sulfur chemical potential. The surfaces were selected from the low-index (100), (110), and (111) cleavage planes and take several different terminations into account. We adopt a naming convention wherein surfaces are identified using their respective Miller indices followed by "Li", "S", or "stoichi". These identify the stoichiometry of the slab as being either lithium-rich, sulfur-rich, or stoichiometric, respectively. As previously described, the upper "S-rich" limit of the sulfur chemical potential—defined as zero for convenience—corresponds to the chemical potential of elemental sulfur.

Comparison calculations similar to those in Figure 3.8 were also performed using the optB88-based vdW-DF functional and by combining the GGA with solvation effects. Figure 3.9 summarizes these results across all three calculation methods (Figure 3.9a: GGA, Figure 3.9b: vdW-DF, Figure 3.9c: GGA with solvation) by plotting the lowest energy terminations for each of the 3 surface normals. All calculation methods agree that a stoichiometric termination of the (111) surface (*i.e.*, the surface identified as "111-stoichi-1") has the lowest surface energy overall. Except at the extreme limits of the S chemical potential, stoichiometric surfaces are also predicted to be the most stable for (100) and (110) facets. These results agree well with a prior study of Li_2S surfaces that employed the GGA functional.[36]

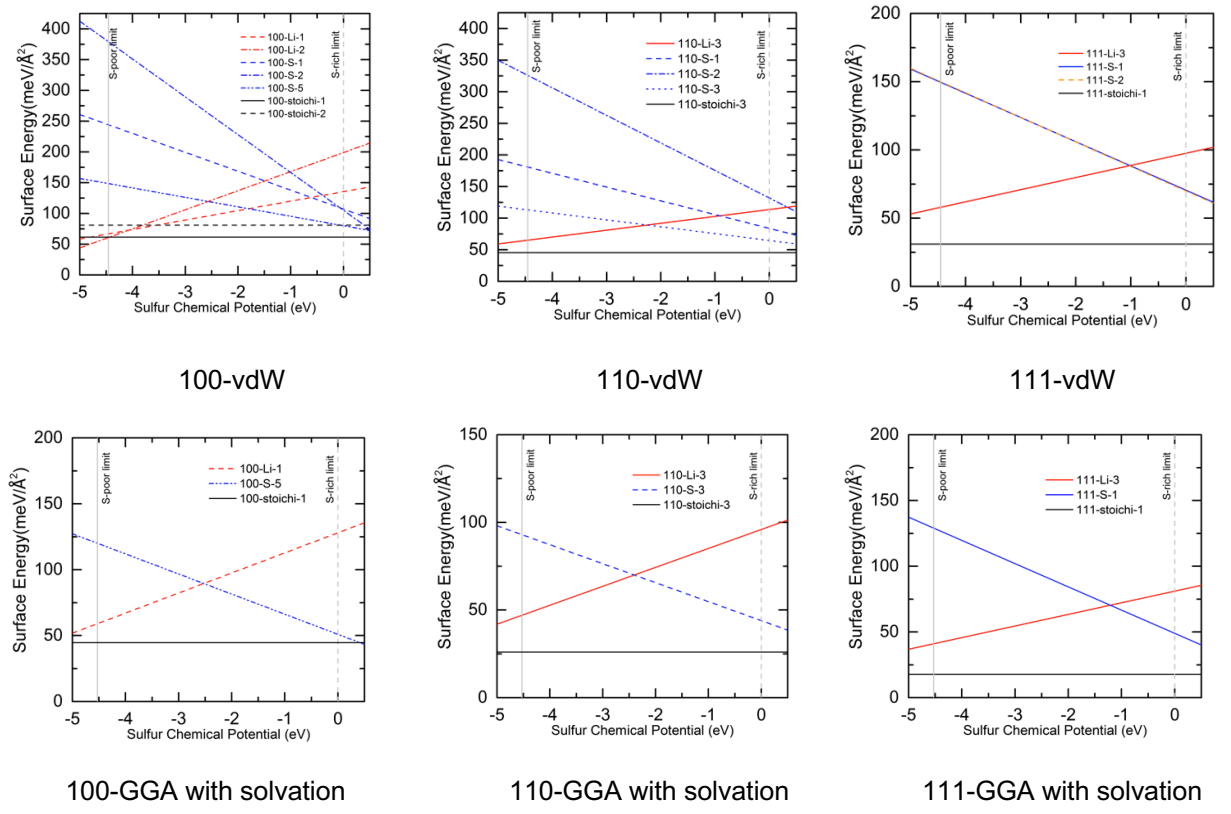

Figure 3.8 Calculated surface free energies for Li_2S as a function of sulfur chemical potential and surface normal using vdW-DF functional and GGA with solvation. Vertical lines represent sulfur poor and rich limits to the S chemical potential.

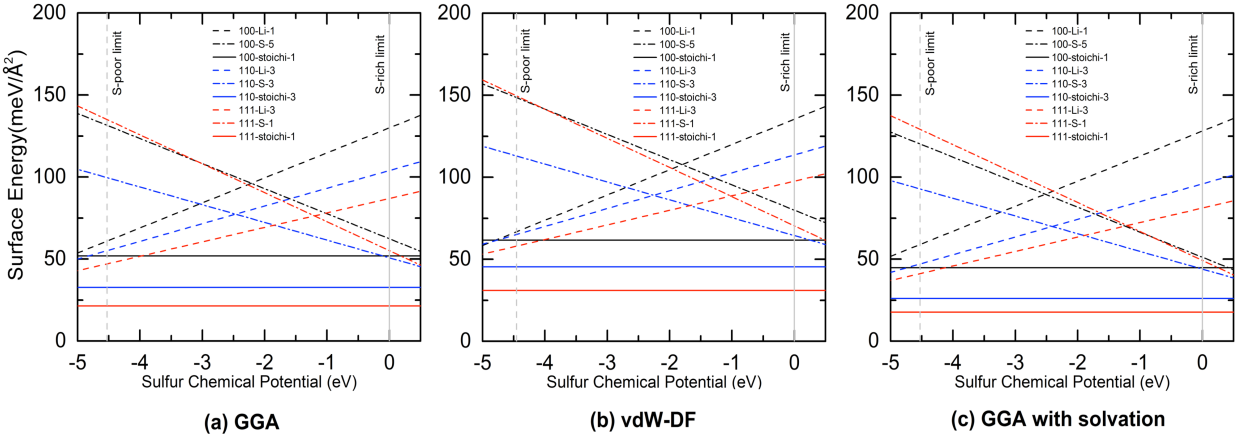

Figure 3.9 Free energies of Li_2S surfaces as a function of sulfur chemical potential and calculation method. (a) GGA, (b) vdW-DF, and (c) GGA + solvation. Vertical lines represent sulfur poor and rich limits to the S chemical potential. The three lowest energy surface normals considered: 100, 110, and 111.

Table 3.4 The most thermodynamically stable Li_2S surface for each facet ((100), (110) and (111)), and its respective surface energy, as a function of calculation method (GGA, vdW-DF and GGA + solvation).

Surface name	Surface free energy (meV/Å^2)		
	GGA	vdW-DF	GGA+solvation
100-stoichi-1	52	61	45
110-stoichi-3	33	45	26
111-stoichi-1	21	31	18

Table 3.4 summarizes the calculated surface energies for the most stable termination of each (*hkl*) facet across the 3 different calculation methods. Compared to the GGA calculations, surface energies calculated with the vdW-DF, are ~10 meV/ Å^2 larger. On the other hand, inclusion of solvation effects result in a slight reduction in surface energies by 3-7meV/ Å^2, as expected. Given that all three methods predict the same stable surface, we conclude that neither van der Waals contributions nor solvation effects has a significant impact on the termination of Li_2S surfaces.

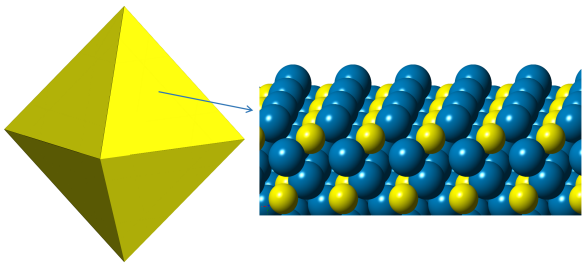

Figure 3.10 . (Left) Equilibrium shape of an Li_2S crystallite based on the Wulff construction and calculated surface energies. (Right) Stoichiometric (111) surface which comprises all faces of the crystallite; blue and yellow spheres represent lithium and sulfur atoms, respectively.

Using the calculated surface energies as input, Figure 3.10 plots the equilibrium shape of an Li_2S crystallite using the Wulff construction.[184]. All calculations methods – GGA, vdW-DF, and GGA+solvation – yield the same crystallite morphology, an octahedron whose surface is completely comprised of stoichiometric (111) surfaces. Such a shape is consistent both with a prior computational study of Li_2S surfaces[36] and with scanning electron microscopy (SEM) images of Li_2S crystallites.[185-186]

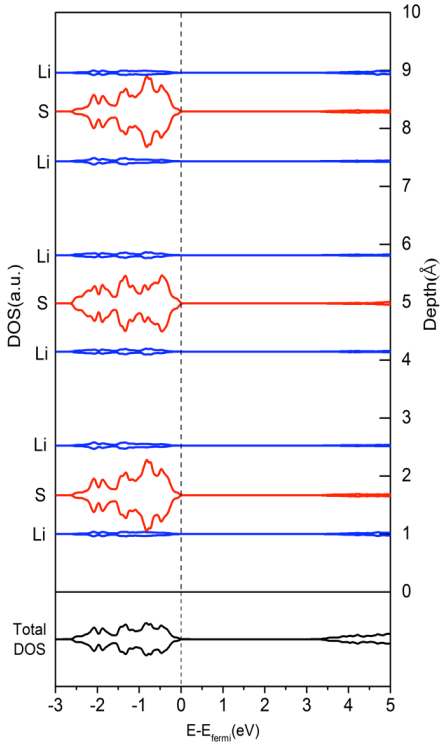

Figure 3.11 Spin-polarized layer projected density of states (LPDOS) as a function of depth into the slab for the 111-stoichi surface of Li_2S. Blue and red lines represent the lithium and sulfur DOS respectively. The blue plots at the top and the bottom correspond

Figure 3.11 shows the layer-projected density of states (DOS) for the 111-stoichiometric surface of Li_2S, calculated using the vdW-DF method. The DOS for each layer shows the presence of a significant gap separating occupied and unoccupied states, indicative of insulating behavior. This behavior is similar to that previously discussed for bulk Li_2S in Figure 3.6(a). We therefore conclude that the surface electronic structure of Li_2S does not significantly differ from that of the bulk.

Table 3.5 Calculated surface energies of α-S surfaces and their re-spective area fraction of the equilibrium crystallite shape.

Surface	Surface Energy (meV/ Å2)		Surface Area Fraction (%)	
	vdW-DF	VASPsol	vdW-DF	VASPsol
001	12	11	30.3	25.0
010	16	13	3.6	1.5
100	11	11	23.2	14.5
011	16	13	8.8	11.8
110	13	10	34.2	47.1
111	17	14	0.0	0.0

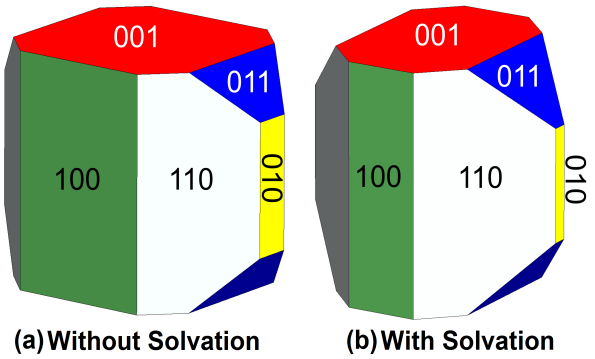

Figure 3.12 Equilibrium shape of α-S crystallites based on the Wulff construction and surface energies calculated using the optB88 vdW-DF functional. (a) Neglecting solvation ef-fects; (b) Including solvation effects. Red, yellow, green blue and white areas repres

Regarding α-sulfur, surface energies were calculated for 7 distinct surfaces (cleaved along 6 <*hkl*> directions) with the vdW-DF with and without solvation effects. Surface models were constructed without cleaving the cycloocta sulfur rings; we presume that surfaces containing broken S-S bonds would exhibit in much higher energies. Table 3.5 summarizes the calculated surface energies for the most stable terminations. In contrast to the surfaces of Li_2S, where only one low-energy termination (stoichiometric 111) dominated, in the case of S several surfaces have energies in a tightly clustered range of 10-14 meV/Å^2 (including solvation effects). (Similar behavior holds without solvation.) Consequently, the resulting Wulff plot (Figure 3.12a: Without solvation, Figure 3.12b: With solvation) is more complex, with 5 out of the 6 surfaces contributing to the area of the equilibrium crystallite (Table 3.5). For both calculation methods (110) facets cover the largest fraction of the crystallite surface area. The presence or absence of solvation effects has a minor effect on the equilibrium crystallite shape. The calculated crystallite shapes are in reasonable agreement with experimental electron microscopy images, which exhibit an hexagonal profile when viewed along a 001 direction.[85]

3.4 Conclusion

Understanding the properties of the solid-phase redox end-members, α-S, β-S, Li_2S, and Li_2S_2, is an important step in improving the performance of Lithium-Sulfur batteries. Despite the growing importance of electrical energy storage devices, the fundamental thermodynamic and electronic properties of these phases remain poorly understood. In the present chapter several computational techniques – van der Waals augmented density functional theory (vdW-DF), quasi-particle

methods (G_0W_0), and continuum solvation techniques – are employed to predict key structural, thermodynamic, spectroscopic, electronic, and surface characteristics of these phases.

The stability of the α allotrope of sulfur at low temperatures was confirmed by revisiting the sulfur phase diagram. Likewise, the stability of lithium persulfide, Li_2S_2, – a phase whose presence during discharge is believed limit capacity – was assessed by comparing the energies of several hypothetical A_2B_2 crystal structures. In all cases Li_2S_2 was predicted to be unstable with respect to decomposition into a two-phase mixture of Li_2S and α-S, suggesting that Li_2S_2 is a metastable phase.

Regarding surface properties, the stable surfaces and equilibrium crystallite shapes of Li_2S and α-S were predicted in the presence and absence of a continuum solvation field intended to mimic the effect of a dimethoxyethane (DME)-based electrolyte. In the case of Li_2S, equilibrium crystallites are comprised entirely of stoichiometric (111) surfaces, while for α-S a complex mixture of several facets is predicted.

Finally, G_0W_0 calculations reveal that all of α-S, β-S, Li_2S, and Li_2S_2 are insulators with bandgaps greater than 2.5 eV.

The properties revealed by this study provide a baseline understanding of the solid-phase redox end members in Li-S batteries. We anticipate that this data will be of value in understanding pathways associated with charge and discharge reactions in these systems, and foster development of approaches that move the Li-S chemistry closer to commercial viability.

Chapter 4 Tuning the Adsorption of Polysulfides with Metal-Organic Frameworks

4.1 Introduction

The goal of this chapter is to identify MOFs that maximize PS adsorption by combining physical encapsulation within the MOF pores with strong chemical anchoring to the MOF. Given its high density of adsorption sites and 1-D porosity, we adopt M_2(dobdc) as a prototype MOF and investigate computationally how metal substitution on the CUS impacts the adsorption of PS. More specifically, first-principles calculations are used to screen 16 metal-substituted variants of M_2(dobdc) (M=Be, Mg, Ca, Sr, Sc, Ti, V, Cr, Mn, Fe, Co, Ni, Cu, Zn, Mo, Sn) with respect to their adsorption energies for prototypical species present during the cycling of Li-S batteries: S_8, Li_2S_4, and Li_2S.

Our calculations reveal that the CUS is the dominant adsorption site for all species examined. Nevertheless, significant differences exist in the strength and nature of the adsorption across the three adsorbates. Adsorption of S_8 is generally weakest, and relatively insensitive to the composition of the CUS. On the other hand, adsorption of Li_2S_4 and Li_2S is typically much stronger, approaching ~400 kJ/mol, and is highly sensitive to CUS composition. A tendency for spontaneous decomposition of the Li_2S_4 molecule is observed for some CUS compositions, yielding very strong adsorption. Trends in the electronic structure for the different systems are examined in terms of Bader charges and spatial charge density differences.

Out of the 16 M_2(dobdc) compositions examined, compounds with M = Ti, Ni, and Mo were identified as having the largest affinities for Li_2S_4 and Li_2S. As the Ni-based variant has been synthesized previously, this MOF is proposed as a promising cathode support for Li-S batteries. An additional benefit of the "encapsulation plus adsorption" strategy is its ability to be combined with electrolyte-based tactics for minimizing PS dissolution, such as use of electrolytes that are non-solvating for PS.[187-189]

4.2 Method

Long-range dispersion interactions between polysulfides and the MOF support were accounted for using a vdW-DF2.[139, 142] In cases where the MOF CUS contained a transition metal,

a Hubbard U correction[146] was also applied to describe the localization of d-electrons more accurately.[190] The plane-wave cutoff energy was set to 500 eV, and k-point sampling was performed at the Γ-point. All calculations were spin-polarized.

Metal-substituted DOBDC crystal structures were adopted from our prior studies.[74] The internal degrees of freedom for these structures were relaxed to a force tolerance of 0.01 eV/Å using the vdW-DF2(+U) functional. Similarly, the adsorbate molecules (S_8, Li_2S_4 and Li_2S) were relaxed to a force tolerance of 0.01 eV/Å using the vdW-DF2 functional in a computational cell having the same shape and size as that for Ni_2(dobdc), but with the MOF atoms absent.

Low energy adsorption geometries for the PS were evaluated by examining several initial adsorption geometries on the MOF. For the lithium-containing molecules (Li_2S_4 and Li_2S), electrostatic considerations suggest that nominally-positive lithium in the PS will be attracted to nominally-negative oxygen atoms within the MOF. Likewise, electrostatic considerations suggest that nominally-negative sulfur will be attracted to the CUS, which exhibits a nominal positive charge (formal charge of +2). The PS+DOBDC geometries were relaxed to a force tolerance of 0.02 eV/Å, while maintaining the full periodicity of the MOF crystal structure (i.e., cluster approximations to the MOF structure were not employed).

Adsorption energies (ΔE_{ads}) were evaluated using the following equation:

$$\Delta E_{ads} = -\frac{1}{n}(E_{MOF+PS} - E_{MOF} - nE_P)\,. \tag{4.1}$$

We adopt a sign convention such that a positive ΔE_{ads} indicates exothermic adsorption. Here n is the number of adsorbed polysulfide (PS) molecules in the DOBDC computational cell. E_{MOF+PS} refers to the total energies of the adsorbed MOF+PS complex. E_{MOF} and E_{PS} refer the total energies of isolated MOF and PS, respectively. The primitive cell for M_2(dobdc) was adopted as the simulation cell; this cell contains 54 atoms. A bader charge analysis[191-192] was used to correlate adsorption energies with the amount of charge transfer between the adsorbed PS and the MOF support.

4.3 Results

4.3.1 Structure

Figure 4.1 shows the relaxed structures and bond lengths/angles of the isolated S_8, Li_2S_4, and Li_2S molecules. These structures employed initial molecular geometries reported in an earlier

study;[65] upon relaxation they maintain a high degree of similarity. The S_8 molecule adopts a cyclo-octa ring morphology, similar to that present in the bulk sulfur crystal structure.[93] In the case of Li_2S_4, the lowest energy structure exhibits a chain-like geometry with Li atoms located at both endpoints. Finally, Li_2S adopts a triangular geometry with a Li-S-Li angle of 124.6°.

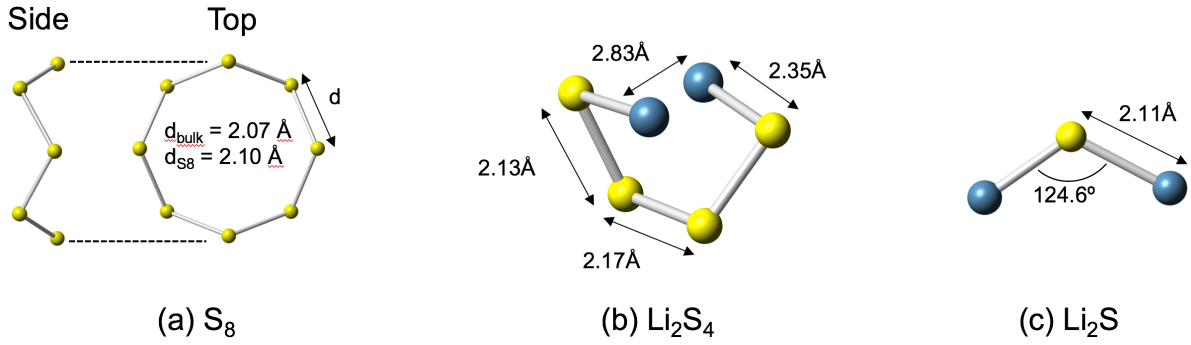

Figure 4.1 Calculated geometries for the molecular species (S_8, Li_2S_4 and Li_2S) examined in this study. Blue and yellow spheres represent lithium and sulfur respectively.

The molecules' geometries upon adsorption in Ni_2(dobdc) are shown in Figure 4.2. In all cases the lowest-energy adsorbed configurations place the molecules adjacent to the CUS. Moreover, sulfur atoms in the adsorbate are generally positioned to be closest to the CUS. In the case of S_8, Figure 4.2a, the 8-membered ring is adsorbed with an orientation such that the plane of the ring is parallel to the axis of the hexagonal pore channel.

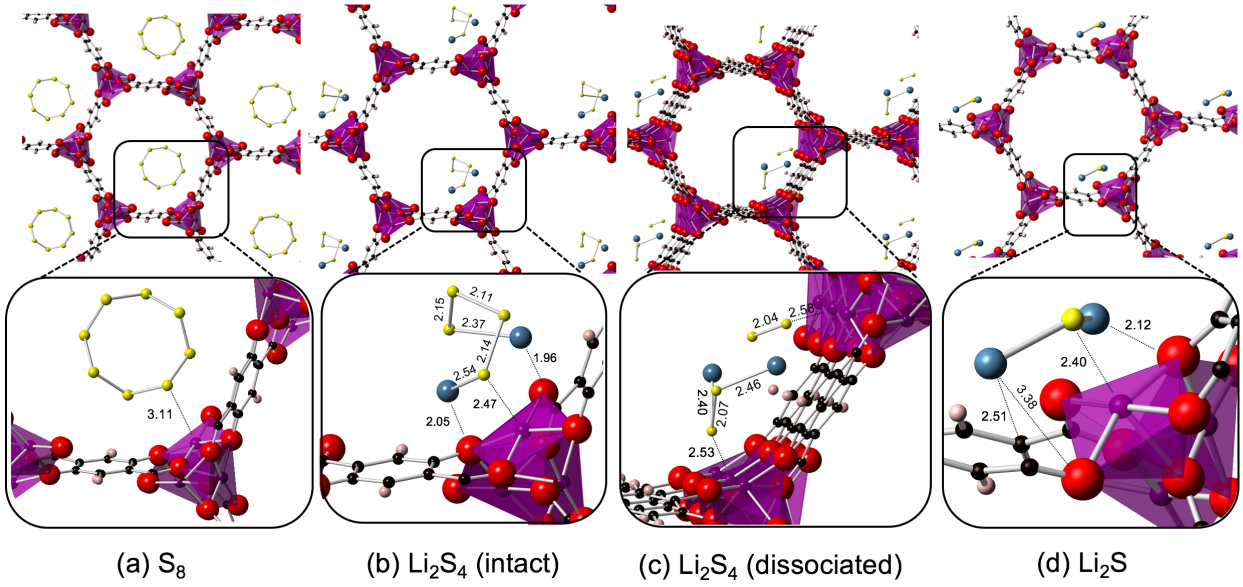

Figure 4.2 Lowest-energy structures for adsorbed (a) S_8, (b) intact and (c) dissociated Li_2S_4, and (d) Li_2S in Ni_2(dobdc). The top row shows the hexagonal pore structure of the MOF and the geometry of a single adsorbed molecule. The bottom row is a magnification o

In the case of Li_2S_4 the calculations reveal that the molecule can adsorb either intact (Figure 4.2b), or for certain CUS compositions, can spontaneously decompose (Figure 4.2c) into a Li_2S_2 molecule and a S_2 molecule. In this latter case the Li_2S_2 and S_2 fragments adsorb on neighboring CUS. The intact cases comprise the majority of the adsorbed geometries observed, corresponding to 11 of the 16 examined CUS compositions. As shown in Figure 4.2b (bottom), these geometries generally exhibit close contact between a sulfur atom in the Li_2S_4 chain with the CUS. Additionally, the terminal lithium atoms in the adsorbate tend to be positioned adjacent to oxygen anions that are nearest-neighbors to the CUS. These geometries are consistent with the expected electrostatic interactions described previously.

Li_2S_4 was observed to undergo dissociative adsorption, Figure 4.2c, on the CUS for cases where M is an early transition metal, M = Sc, Ti, V, Cr, and Mo. As discussed below, Li_2S_4 dissociation correlates with very exothermic adsorption energies. Representative adsorbed geometries for Li_2S_4 adsorption are given in Figure 4.3 for the dissociated and the intact case.

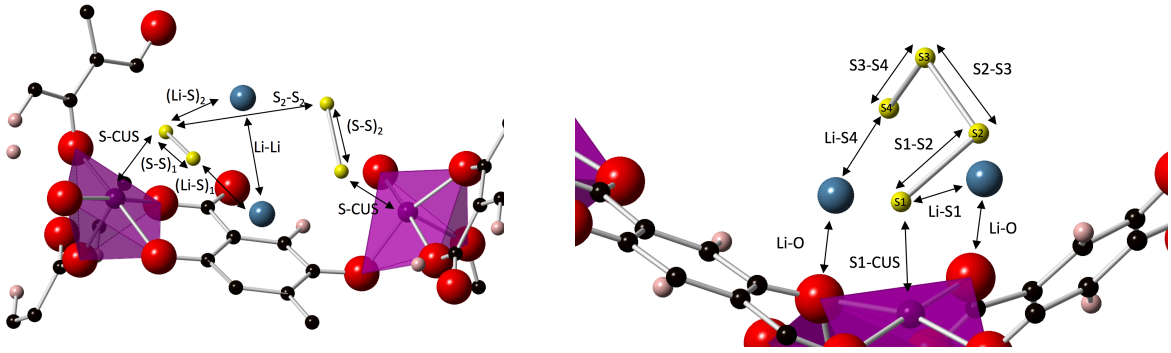

Figure 4.3 Structure of dissociated (left) and intact (right) Li_2S_4 adsorbed in the vicinity of the coordinatively unsaturated metal site in Ni-DOBDC.

Unlike the behavior of Li_2S_4, the adsorption of Li_2S occurs with an intact geometry, Figure 4.2d, which is similar to that of the isolated molecule. Consistent with an electrostatic interaction, the S atom in Li_2S is in close proximity to the CUS, while at least one of the two Li atoms is adjacent to an O anion in the MOF. A list of bond lengths and angles for Li_2S upon adsorption to various M_2(dobdc) variants is given in Table 4.1. In general, the average distance between the CUS and the nearest S atom in the adsorbate is inversely correlated with the strength of adsorption (described below). These distances are: 3.23 Å for S_8, 2.47 and 2.81 Å, respectively, for dissociated and intact Li_2S_4, and 2.58 Å for Li_2S. An illustration of the structgure of adsorbed Li_2S in the vicinity of the CUS in Ni_2(dobdc) is given in Figure 4.4.

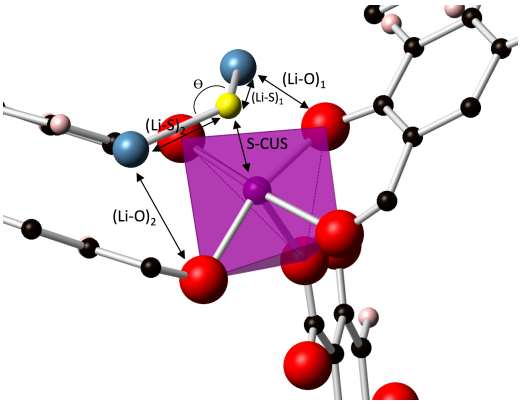

Figure 4.4 Structure of adsorbed Li_2S in the vicinity of the CUS in Ni-DOBDC.

Table 4.1 Calculated distances (in Å) and bond angles for Li_2S adsorbed on M-DOBDC, as illustrated in Figure 4.4. Bond parameters for isolated Li_2S are given in the bottom row. θ refers to the angle within the Li_2S molecule.

	S-CUS	$(Li-O)_1$	$(Li-O)_2$	$(Li-S)_1$	$(Li-S)_2$	θ (°)
Be	4.15	1.92	3.40	2.26	2.21	113.61
Mg	2.49	2.10	3.36	2.29	2.18	121.68
Ca	2.72	2.04	3.53	2.17	2.28	140.75
Sr	2.94	1.89	3.03	2.18	2.15	161.25
Sc	2.52	1.93	2.67	2.21	2.24	169.91
Ti	2.35	1.94	3.28	2.27	2.40	129.74
V	2.37	1.98	3.21	2.28	2.34	124.89
Cr	2.59	1.99	3.33	2.20	2.28	111.22
Mn	2.40	1.89	3.35	2.21	2.34	128.90
Fe	2.33	1.94	3.37	2.22	2.39	122.28
Co	2.35	1.95	3.33	2.21	2.33	120.80
Ni	2.40	2.03	3.38	2.32	2.21	117.34
Cu	2.36	1.96	3.32	2.27	2.35	108.21
Zn	2.22	1.91	1.91	2.26	2.35	146.97
Mo	2.47	2.10	3.11	2.32	2.47	94.99
Sn	2.61	1.84	3.33	2.30	2.24	110.12
Isolated Li_2S				2.11	2.11	124.60

4.3.2 Energetics

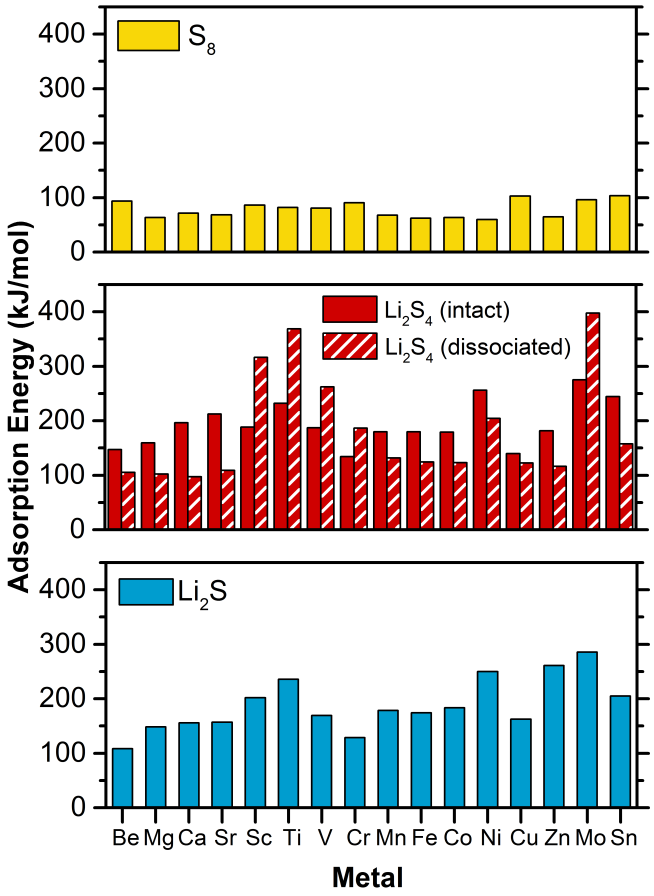

Figure 4.5 Calculated adsorption energies for S_8 (top), Li_2S_4 (middle, differentiating between intact and dissociated geometries), and Li_2S (bottom), as a function of CUS composition, M, within the MOF M2(dobdc).

The calculated adsorption energies for S_8, Li_2S_4, and Li_2S in M_2(dobdc) are plotted in Figure 4.5 as a function of the CUS composition. For Li_2S_4, separate adsorption energies were evaluated for intact and dissociated geometries. [For compositions where Li_2S_4 did not spontaneously dissociate, ΔE_{ads} for a (hypothetical) dissociated adsorbate was evaluated by initiating the relaxation from a dissociated geometry similar to that observed for the spontaneous cases.]

Averaging across the 16 CUS compositions, adsorption of S_8 is the weakest amongst all Li-S adsorbates examined, at 78 kJ/mol. At the opposite extreme, spontaneously-dissociated Li_2S_4 exhibits the most exothermic adsorption energies, 306 kJ/mol on average. Finally, Li_2S and intact Li_2S_4 have intermediate values of 189 and 188 kJ/mol, respectively. To place these values in context, we note that adsorption energies for Li_2S_4 and Li_2S are (significantly) more exothermic than those reported previously for other small molecules such as CO_2, CH_4, and SO_2 within

M_2(dobdc): for CH_4 and CO_2 ΔE_{ads} values less than 55 kJ/mol were reported.[74, 193] The calculated ΔE_{ads} of 150kJ/mol[190] for SO_2, which is a much more reactive species, also falls below the average values reported here for Li_2S_4 and Li_2S adsorption.

Turning first to the adsorption of S_8, Figure 4.5a shows that the adsorption energy is relatively insensitive to the CUS composition, with ΔE_{ads} exhibiting a standard deviation of only 15 kJ/mol across the different metal compositions. The magnitude of the adsorption energies and limited sensitivity to the metal composition are consistent with a van der Waals interaction between the adsorbate and the MOF, augmented by a slight polarization of the S_8 (see discussion of Electronic Structure below). A similar conclusion regarding the van der Waals nature of the adsorption interaction has been discussed in earlier reports.[68, 93] For example, Cui *et al.* demonstrated that the adsorption energy for S_8 on various metal chalcogenides is relatively insensitive to composition – ranging from 72 to 82 kJ/mol – in very good agreement with the adsorption energies reported here.[33]

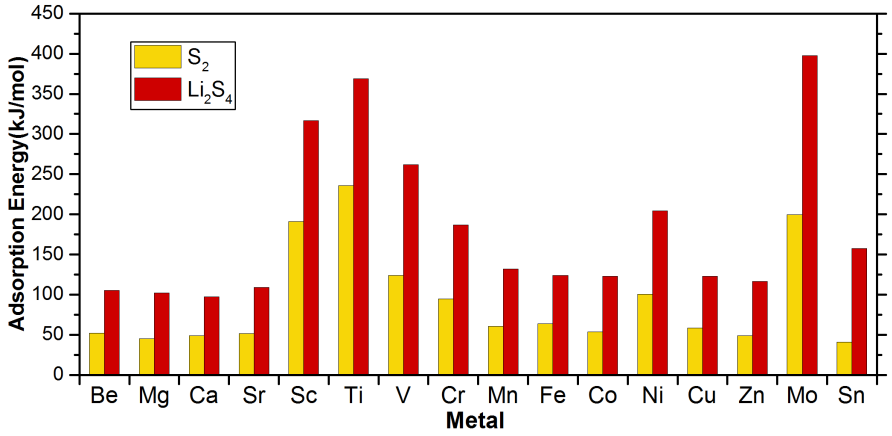

Figure 4.6 Adsorption energies for S_2 and dissociated Li_2S_4 in M-DOBDC.

Adsorption energies for the polysulfides are generally more exothermic. In the case of Li_2S_4, Figure 4.5b summarizes ΔE_{ads} for both intact and dissociative adsorption. As previously described, dissociative adsorption is preferred for the early transition metals, M = Sc, Ti, V, Cr, and Mo, whereas intact adsorption prevails when the CUS composition is an alkaline earth metal or a mid- to late-series transition metal. Dissociative adsorption correlates strongly with highly exothermic adsorption: of the five MOF compositions with the largest ΔE_{ads}, four involve Li_2S_4 dissociation. The high intact ΔE_{ads} predicted on Ni_2(dobdc) represents the lone exception to this trend. The largest adsorption energy overall occurs for M = Ti and Mo, with values of 369 kJ/mol and 398

kJ/mol. These values exceed those for Li_2S_4 adsorption on metal chalcogenides, which achieved a maximum of 360 kJ/mol on V_2O_5,[68] suggesting an even greater tendency to suppress PS dissolution in these MOFs. (Although not discussed in detail here, Figure 4.6 compares the adsorption energies of S_2 in M_2(dobdc) to that of dissociated Li_2S_4. The adsorption trend across the various metal substitutions is observed to be similar for both molecules; this is expected given that S_2 are components of dissociated Li_2S_4.)

In the case of Li_2S, intact adsorption dominates. The predicted ΔE_{ads} values – while not as uniform with respect to CUS composition as for S_8 – exhibit less variation than for Li_2S_4 adsorption. Nevertheless, some similarities with Li_2S_4 adsorption persist: for example, 4 of the top 5 most strongly-adsorbing MOF compositions are the same for Li_2S and Li_2S_4. These include Sc, Ti, Ni, and Mo. Nevertheless, even in these exceptional cases, the magnitude of ΔE_{ads} for Li_2S is significantly smaller than for Li_2S_4. For example, the maximum ΔE_{ads} for Li_2S is 286 kJ/mol in the case of Mo_2(dobdc); this is 112 kJ/mol smaller than for Li_2S_4 adsorption on the same MOF.

Our observation that the adsorption of Li_2S in M_2(dobdc) is generally less exothermic than for Li_2S_4 differs from the trend reported for the adsorption on metal chalcogenides,[68] where Li_2S adsorption was reported to be stronger. This difference can be traced to the highly exothermic nature of dissociative adsorption of Li_2S_4 in the MOF. In M_2(dobdc), dissociation can strengthen the attraction of Li_2S_4 to the MOF by more than 100 kJ/mol compared to the intact case. This is approximately twice the energy increment reported for dissociative adsorption on the metal chalcogenides.[68]

As described in the introduction, by synthesizing variants of M_2(dobdc) with different CUS metals it may be possible to tune the adsorption behavior of the PS and the redox end members (REM), S and Li_2S. The adsorption energies evaluated here allow us to identify potentially-optimal M_2(dobdc) compositions. Our assessment is based on two assumptions: (*i.*) stronger adsorption is preferred, as it will maximize the anchoring effect, and, (*ii.*) anchoring the PS is of greater importance than anchoring the REM, as the PS are more soluble, and thus more likely to "escape" from the cathode.

These factors suggest that optimal M_2(dobdc) compositions will be those having the largest adsorption energies for Li_2S_4. As shown in in Fig. 3, these compositions include M = Sc, Ti, V, Ni, and Mo. As an added benefit, 4 of these metals (Sc, Ti, Ni, and Mo) are within the top-5 compositions for adsorption of Li_2S (Fig. 3), suggesting that strong anchoring of Li_2S should also

be provided by these MOFs. The relatively weaker interaction between S_8 and all CUS compositions considered here suggests that S_8 adsorption is not a differentiating factor in identifying optimal M_2(dobdc) compositions.

Which of these compositions is most promising? Cost considerations suggest that scandium is impractical. Ease of synthesis is also an important consideration; to our knowledge M_2(dobdc) variants with M = Ti, V, and Mo have not been reported. Finally, as a member of the 4d series, Mo is the heaviest candidate on our list; this could compromise the cell's specific energy.

Thus, the process of elimination leads us to Ni_2(dobdc) as the most promising Li-S cathode support. We note that Ni_2(dobdc) has been successfully sunthesized.[194] The unique ability of this MOF to bind Li_2S_4 strongly with an intact morphology (Figure 4.5) may also yield kinetic benefits compared to metals that dissociate the PS. Our prediction that Ni_2(dobdc) is the most promising composition in the M_2(dobdc) series is consistent with the experimental measurements of Zheng *et al.,* who reported that a MOF with a Ni-based CUS outperformed the analogous Co-CUS compound in a Li-S cell.[87]

Because many MOFs are electrical insulators, conduction-enhancing additives such as carbon may be needed in MOF-based cathodes to ensure sufficient electronic transport. Recent work, however, has shown the possibility of overcoming this limitation, with conductivities of mS/cm or higher having been reported in selected MOFs.[195] Notably, a conductivity of 7 S/m was reported in HKUST-1, a CUS-containing MOF that has been infiltrated with redox-active guest molecules.[196]

4.3.3 Electronics

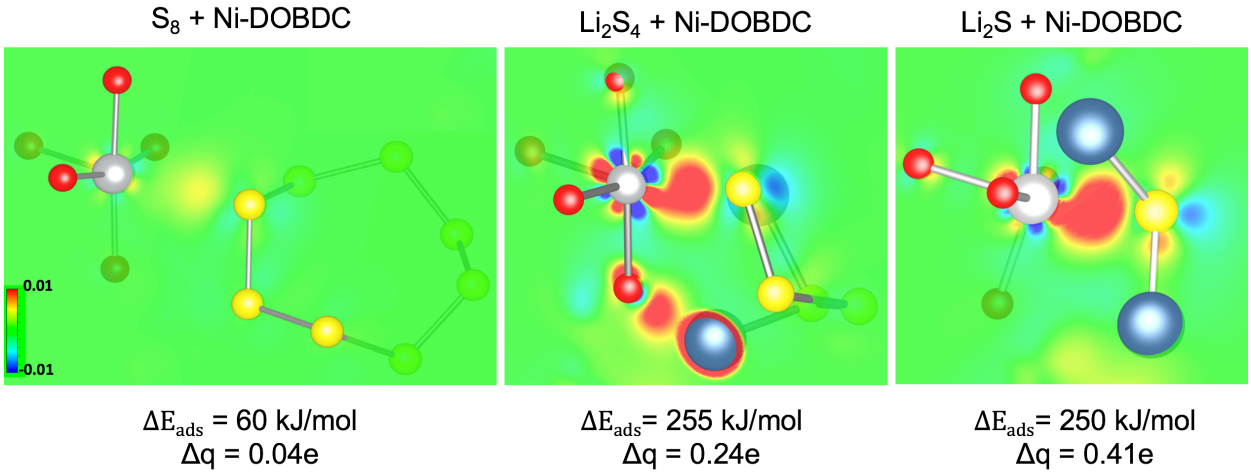

Figure 4.7 Charge density difference, $\rho_{adsorbed} - \Sigma\rho_{isolated}$, for S_8 (left), Li_2S_4 (middle), and Li_2S (right) adsorbed on Ni_2(dobdc). The plot is con-structed for a plane that intersects the CUS-S bond axis and one other bonded pair of atoms in the adsorbate. For

Figure 4.7 compares charge density differences, adsorption energies, and the amount of charge transferred (from adsorbate to MOF) for S_8, Li_2S_4, and Li_2S adsorption on Ni_2(dobdc). As expected, the degree of charge transfer generally increases from S_8 to either Li_2S_4 or Li_2S, roughly consistent with the adsorption energies. A similar trend is observed for the charge density difference maps, which indicate larger charge accumulation between the CUS cations and S atoms in Li_2S_4 and Li_2S compared to that for S_8 adsorption. Additional charge accumulation is observed between the Li ions in Li_2S_4 and Li_2S and the O atoms in the MOF nearest to the CUS (Figure 4.8).

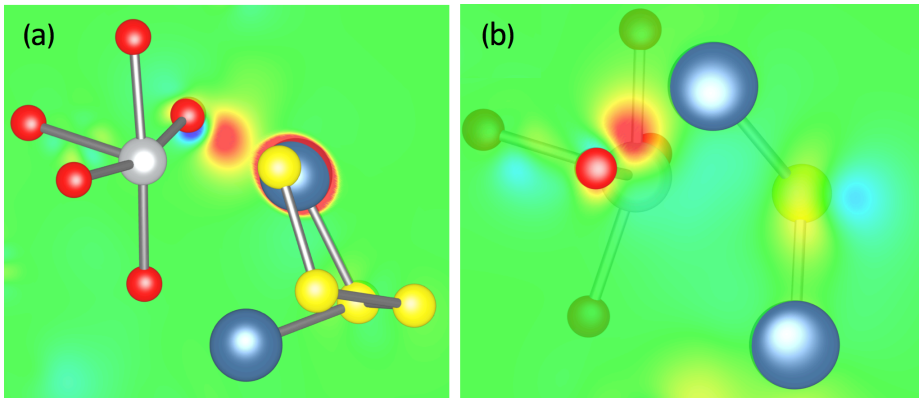

Figure 4.8 Charge density difference plot showing charge accumulation between O atoms in Ni-DOBDC and Li atoms in adsorbed (a) Li_2S_4 and (b) Li_2S.

Table 4.2 summarizes the degree of charge transfer – evaluated as the difference in summed Bader charges, before and after adsorption – associated with adsorption across the various M_2(dobdc) compositions and adsorbates. Here, positive values refer to charge accumulation on

the MOF, and *vice versa*. For the adsorption of S_8, the amount of charge transferred is negligible across the M_2(dobdc) variants, 0.04 e, on average, lending additional support to the assertion that S_8 adsorption can be described by a relatively weak van der Waals interaction.[197]

Electrostatic interactions contribute to the larger adsorption energies observed for Li_2S_4 and Li_2S. Turning first to Li_2S_4, Table 4.2 demonstrates that the amount of charge transferred on average between Li_2S_4 and the MOF is 4 (intact adsorption) to 7 (dissociative adsorption) times larger than for S_8 adsorption, consistent with the trend in adsorption energies. For intact Li_2S_4 adsorption, a relatively small amount of charge is transferred to the MOF for all metal compositions, approximately 0.25 e or less. In contrast, for dissociative Li_2S_4 adsorption involving M = Sc, Ti, V, Cr, and Mo, the charge transfer direction is reversed, with a net charge accumulation on the Li_2S_4 fragments. In these cases, the magnitude of charge transfer is also much larger, ranging from about 0.5 to 1.2 electrons.

Table 4.2 Adsorption energies (ΔEads, in kJ/mol) for intact and dissociated Li_2S_4, S_8, and Li_2S on M-DOBDC, and the corresponding charge transfer between adsorbate and MOF (Δq, in electrons) based on a Bader charge analysis. A negative (positive) value for Δq indicates charge transfer from (to) M-DOBDC to (from) the adsorbate. Average values across the metal compositions are listed at the bottom. In the case of Δq, the average absolute value is reported.

Metal	Intact Li_2S_4		Dissociated Li_2S_4		S_8		Li_2S	
	ΔE_{ads}	Δq	ΔE_{ads}	Δq	ΔE_{ads}	Δq	ΔE_{ads}	Δq
Be	147	0.13	105	0.07	93	0.01	109	0.57
Mg	160	0.07	102	-0.14	63	0.00	149	0.17
Ca	196	0.08	97	-0.20	72	0.00	156	0.20
Sr	213	0.13	109	-0.15	68	0.00	157	0.14
Sc	188	0.16	317	-1.20	86	-0.12	202	0.29
Ti	232	0.26	369	-0.91	82	-0.22	236	0.48
V	187	0.11	262	-0.63	81	-0.01	170	0.49
Cr	134	0.09	187	-0.46	90	0.00	129	0.26
Mn	180	0.18	132	-0.17	68	0.03	178	0.36
Fe	180	0.24	124	-0.07	62	0.03	174	0.38
Co	179	0.25	123	-0.02	64	0.04	184	0.42
Ni	256	0.24	205	0.03	60	0.04	250	0.41
Cu	140	0.15	123	0.10	103	0.02	163	0.56
Zn	182	0.28	117	0.04	65	0.03	261	0.55
Mo	275	0.23	398	-0.58	96	-0.03	286	0.62
Sn	244	0.03	157	0.06	103	-0.01	205	0.40
Avg.	193	0.16	183	0.30	78	0.04	188	0.39

Finally, Li_2S adsorption exhibits the largest average charge transfer with the MOF, 0.39 e. The net transfer is to the MOF for all metal compositions, and the average amount of charge transferred is approximately twice that for intact Li_2S_4 adsorption. We note that the charge transfer trends between Li_2S and intact Li_2S_4 adsorption are not reflected in their average ΔE_{ads} values, which are nearly identical (~190 kJ/mol). This apparent discrepancy can be explained by size differences between these molecules: smaller Li_2S has fewer, but stronger interactions with the MOF, whereas the larger size of Li_2S_4 allows for more numerous bonding interactions that are relatively weaker, on average.

4.4 Conclusion

A means to suppress the dissolution of polysulfides will accelerate the commercialization of Li-S batteries. Toward this goal, the present study has explored the use of MOFs as PS-constraining cathode support materials. MOFs are promising support materials because the intrinsic encapsulation afforded by MOF pores can be augmented by chemical adsorption of PS onto coordinately unsaturated metal sites (CUS).

We demonstrate that the combination of PS encapsulation and adsorption can be tuned to maximize PS anchoring *via* substitution on the CUS. Optimal compositions are pinpointed by computationally screening 16 metal-substituted variants of M_2(dobdc) for their ability to chemically anchor prototypical species (S_8, Li_2S_4, and Li_2S) present during the cycling of Li-S batteries. Importantly, the adsorption capacity of M_2(dobdc) is predicted to range from 6.6 to 13.4 mg of Li_2S_4 per 10 mg of MOF. These theoretical capacities outperform the best sulfur support material demonstrated in the literature, MnO_2, which has a capacity of ~6 mg Li_2S_4/10 mg MnO_2.

Our calculations reveal that the CUS is the dominant adsorption site for all species examined. Nevertheless, significant differences exist in the strength and nature of the adsorption across the three adsorbates. Adsorption of S_8 was observed to be relatively weak and insensitive to the composition of the CUS, consistent with a van der Waals-type interaction. In contrast, adsorption of Li_2S_4 and Li_2S is predicted to be much stronger, approaching ~400 kJ/mol, and is highly sensitive to CUS composition. A tendency for spontaneous decomposition of the Li_2S_4 molecule was observed on Sc_2, Ti_2, V_2, and Mo_2(dobdc), yielding very strong adsorption. The calculated adsorption energies can exceed those reported for Li_2S_4 adsorption on metal chalcogenides, suggesting an even greater tendency to suppress PS dissolution in M_2(dobdc). Analysis of Bader

charges and charge density difference maps reveal that electrostatic interactions contribute to the large adsorption energies observed for Li_2S_4 and Li_2S.

Finally, Ti_2, Ni_2, and Mo_2(dobdc) were identified as the compositions with the largest affinities for Li_2S_4 and Li_2S. As Ni_2(dobdc) has been synthesized previously, this MOF is proposed as a promising cathode support for Li-S batteries.

Chapter 5 Adiabatic and Nonadiabatic Charge Transport

5.1 Introduction

The goal of this chapter is to elucidate charge transport mechanisms in the S and Li_2S REMs in Li-S batteries, while carefully accounting for the (non)adiabatic nature of these processes. The calculated transport rates are used to estimate the theoretical maximum loadings (i.e., limiting film thicknesses) for S and Li_2S that are consistent with practical discharge rates. More specifically, we separately examine the ionic and electronic conductivity resulting from the formation and migration of ionic and electronic carriers in these two materials. The equilibrium concentrations of several plausible charge carriers and their respective adiabatic mobilities were evaluated at the hybrid functional level of theory,[147, 149] using a tuned fraction of exact exchange.[99] Subsequently, nonadiabatic effects were examined using the constrained DFT formalism (cDFT). The combination of these approaches allows for a rigorous understanding of how transport phenomena in Li-S cathodes can limit battery performance.

In sulfur, transitions between S_8 rings are predicted to be nonadiabatic. Consequently, conventional DFT erroneously overestimates charge transfer rates by up to 2 orders of magnitude, highlighting the importance of going beyond the Born-Oppenheimer approximation. Delocalized holes, and to a lesser extent, localized electron polarons (p^-), are predicted to be the most mobile electronic charge carriers. All carriers in sulfur exhibit extremely low equilibrium concentrations, and thus yield negligible contributions to the conductivity. Nevertheless, the mobilities of free holes and p^- are sufficient to enable the sulfur loading targets necessary for high energy densities. Based on the calculated mobility, and assuming a C/5 discharge rate, we estimate that p^- can transit S films with a thickness of approximately ~100 μm. The diffusion length for free holes is much larger, ~1 m. These thicknesses exceed the JCESR S loading target of 6 mg/cm^2,[54, 198] which correspond to a S film with an average thickness 30 μm.

In the case of Li_2S, positively charged Li interstitials and negatively charged vacancies are the dominant ionic carriers. The Li vacancy is most mobile of these carriers, with an activation energy of 0.32 eV. The most prevalent electronic carriers are hole polarons; however, these carriers are predicted to have a high formation energy (1.95 eV) and extremely low equilibrium concentrations.

Despite its low concentration, the hole polaron is highly mobile, with a maximum migration length of ~40 mm at a charging rate of C/5. In contrast, the equivalent migration length for Li vacancies is much smaller, ~240 μm. Importantly, the migration lengths for both carriers surpass the projected maximum thickness (50 μm) of a Li_2S film formed upon discharge (assuming an initial sulfur loading equal to the JCESR target).

5.2 Method

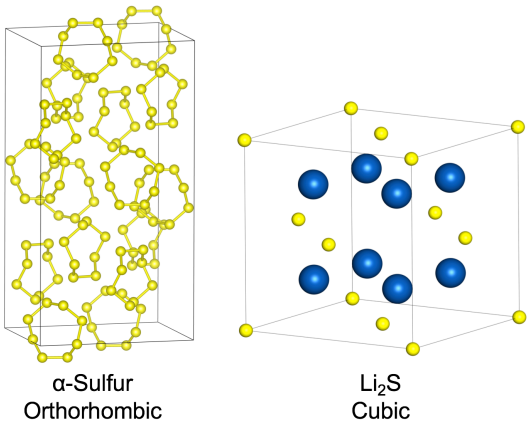

Figure 5.1 Crystal structures of α-S and Li_2S. Blue and yellow spheres represent Li and S atoms, respectively.

The formation energies and adiabatic mobilities of various charge carriers were evaluated using DFT as implemented in the VASP.[161-162] The simulation cells consisted of the conventional unit cell for α-S (128 atoms), and a 96-atom supercell constructed from a 2×2×2 replication of the Li_2S unit cell. The unit cells for both materials are shown in Figure 5.1. Calculations on the bulk properties of S and Li_2S were reported earlier.[93]

The internal degrees of freedom for both supercells were relaxed to a force tolerance of 0.04 eV/Å (α-S) and 0.01 eV/Å (Li_2S). The dimensions of the α-S supercell were previously calculated[199] using the vdW-DF functional; the following lattice constants were obtained: a = 10.33 Å, b = 12.76 Å, and c = 24.45 Å. The present defect calculations are to be performed using hybrid functionals, which do not account for van der Waals interactions between S_8 rings in α-S. Therefore the lattice constants of α-S were fixed to the experimental lattice constants,[177] a = 10.46 Å, b = 12.87 Å, and c = 24.49 Å. The lattice constant for Li_2S was determined by fitting total energies and volumes to the Murnaghan equation of state[166] using the HSE_α functional (described below). The calculated lattice constant is 5.68 Å is well matched to the experimental value,[174] 5.69 Å. K-point sampling was performed at the Γ-point for α-S and using two irreducible k-points for

Li_2S. The PAW scheme[163-164] was used to treat core-valence electron interactions. All calculations were spin-polarized with planewave cutoff energies of 450 eV (α-S) and 500 eV (Li_2S).

A total of 18 (α-S) and 24 (Li_2S) distinct defects were studied. These defects were considered both as charged and neutral species, and were comprised of vacancies, interstitials, and polarons. Formation energies were evaluated for all symmetry-distinct sites. For Li_2S, Frenkel and Schottky defects were also investigated.

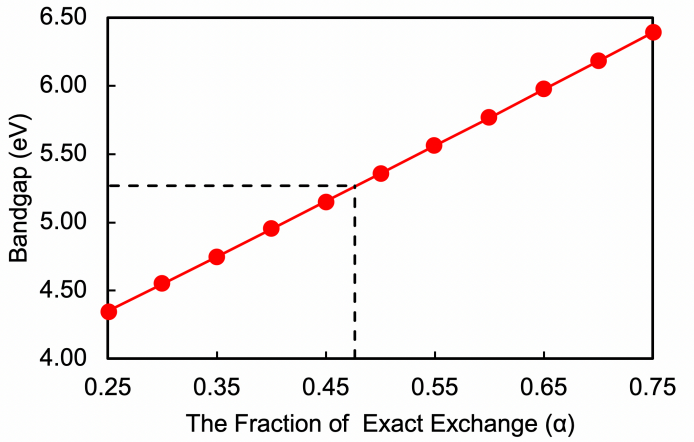

Figure 5.2 Bandgap of Li_2S calculated by the Heyd–Scuseria–Ernzerhof hybrid functional with various fractions of exact exchange (α).

Earlier studies have shown that self-interaction errors present in semi-local functionals can negatively impact the accuracy of these methods when applied to defects that are expected to exhibit localized charge distributions, such as polarons.[200-202] To minimize these errors, the Heyd–Scuseria–Ernzerhof (HSE)[147, 149] screened hybrid functional was used with the fraction of exact exchange, α, set to 0.48 (HSE_{48}). Figure 5.2 shows the bandgap of Li_2S calculated as a function of α. At α=0.48 the calculated Li_2S bandgap (5.28 eV) matches closely the value obtained from many-body G_0W_0 (5.27 eV)[93] theory. A similar approach has been used[99] to examine charge transport in several peroxides and superoxides.[99, 102, 150-152]

The formation energy (E_f) of a defect X with charge state q is given by:[203-204]

$$E_f(X^q) = E_0(X^q) - E_0(\text{bulk}) - \sum_i n_i\mu_i + q\varepsilon_F + E_{MP1} \quad . \tag{5.1}$$

Here $E_0(X^q)$ and $E_0(\text{bulk})$ correspond to the total energy of the defect-containing and pristine simulation cells, respectively. n_i is the number of atoms of the i^{th} species in the defect cell, and μ_i is that species' chemical potential. ε_F is the Fermi level referenced to the valence band maximum.$\varepsilon_F$is determined by the charge neutrality condition, $\sum_{X^q} q\ C(X^q) = 0$, where $C(X^q)$ is

the equilibrium concentration of defect X^q(defined below). E_{MPI} is the Makov–Payne finite-size correction, which was evaluated using dielectric constants of 7.9 (Li_2S) and 4.0 (S_8),[205] and which is applied to supercells containing charged defects.[203, 206] The chemical potential of S, μ_S, is given by the energy per atom of bulk α-S. The chemical potential of Li (μ_{Li}) in the cathode is given by: $\mu_{Li}(Li) = \mu_{Li}(\text{BCC Li}) - eE$, where $\mu_{Li}(\text{BCC Li})$ is the energy per atom of bulk (BCC) Li, and E = 2.3 V is the theoretical cell voltage of a Li-S cell.[99, 207]

The equilibrium concentration C of a defect X^q is given by $C(X^q) = D_X e^{-E_f(X^q)/k_B T}$, where D_X is the number of equivalent sites per unit volume.[204] The mobility (μ) and the diffusion coefficient(D) for a given carrier are given by:

$$\mu = \frac{\nu q a^2}{k_B T} e^{-\frac{E_b}{k_B T}} \text{ and } D = \frac{\mu k_B T}{q} = \nu a^2 e^{-\frac{E_b}{k_B T}} \quad . \tag{5.2}$$

where ν is the hopping attempt frequency[99] (10^{13} s^{-1}) and a is the hopping distance. In the adiabatic approximation, the migration barriers (E_b) of defects are obtained using the climbing image NEB (CI-NEB) method.[106-108] Due to electron delocalization[208] errors, semi-local functionals such as the GGA cannot accurately estimate the hopping barrier of localized electronic species, such as polarons.[99] Hence, we have used the HSE_{48} functional[99, 147] for computing migration barriers. Finally, defect concentration and mobility are used to estimate the equilibrium conductivity, σ, associated with a specific defect species, using $\sigma = qC\mu$.

To account for possible nonadiabadic effects in charge transfer reactions, polaron hopping was also studied using constrained DFT (cDFT)[209,210] as implemented[211] in the GPAW code,[212-213] using the PBE[136] exchange correlation functional (hybrid functionals have not been implemented in GPAW) and a grid basis with a spacing of 0.16 Å. As previously mentioned, GGA functionals over-delocalize charge due to self-interaction errors. However, in cDFT, charge and spin constraints are used to obtain strictly localized charge and magnetization. The cDFT energy is the written as a sum of the usual Kohn-Sham energy, plus a penalty term:

$$F[n, \{V_c\}] = E_{KS}[n] + \sum_{i,s} V_i \left[\int d\boldsymbol{r} w_i^s(\boldsymbol{r}) n^s(\boldsymbol{r}) - N_i \right]. \tag{5.3}$$

where n is electron density, i is an index specifying the constrained region, s refers to spin, N_i is the specified charge/spin to be localized in the chosen initial/final state, and V_i is the Lagrange multiplier determining the strength of the external potential. Both the Lagrange multiplier and

electron density are solved self-consistently. w_i^s is the weight function specifying the spatial extent of the constrained region. Here, the weight function is partitioned into atomic contributions using Hirschfeld partitioning with Gaussian atomic densities based on scaled covalent radii. This ensures that w_i^s correctly models localization on both atoms and fragments. The constrained charges are formed by adding (removing) one electron to create an electron (hole) polaron and requiring that the region carries a magnetization of 1. The convergence criterion for cDFT calculations is 0.01 e. (Additional details regarding cDFT can be found in the literature.[209,210,211]) In Li_2S, charge and spin are constrained on a single sulfur atom, as the polarons in this system are localized on atomic sites. In α-S the constraining regions are on two neighboring atoms, accounting for the fact that polarons occupy orbitals between S pairs.

Once the diabatic cDFT states are obtained for the initial and final states of a polaron hopping event, the hopping rate is given by the Landau-Zener equation, which captures both adiabatic and nonadiabatic transitions[214, 215, 216]:

$$\mathrm{k}_{a\to b} = v_n \kappa \exp\left[-\frac{(\Delta G^0 + \lambda)^2}{4k_B T\lambda} + \frac{\Delta}{k_B T}\right]. \tag{5.4}$$

Here v_n is the vibrational frequency (taken here as 10^{13} s^{-1}), Δ is an adiabadicity correction to the diabatic Marcus barrier, and κ is the electronic transmission coefficient computed from the Landau-Zener transition probability[214]

$$\kappa = \frac{2P_{LZ}}{1 + P_{LZ}} \quad ; \quad P_{LZ} = 1 - exp[-2\pi\gamma]\,; \tag{5.5}$$

$$2\pi\gamma = \frac{\pi^{3/2}|H_{ba}|^2}{h v_n \sqrt{k_B T\lambda}} \;;\; \lambda = E_a(\boldsymbol{R}_a) - E_b(\boldsymbol{R}_b) \tag{5.6}$$

For an adiabatic reaction $\gamma \gg 1$, $\kappa \cong 1$, and Eq. (5.4) reduces to the commonly used transition state rate. For a nonadiabatic reaction, $\gamma < 1$ and $\kappa \ll 1$, in which case the Marcus equation is obtained. λ is the reorganization energy, and is computed as the energy difference of the donor state in the final and initial state geometries $\boldsymbol{R}_a$ and $\boldsymbol{R}_b$, respectively.

5.3 Results

5.3.1 Intrinsic Defects in α-S

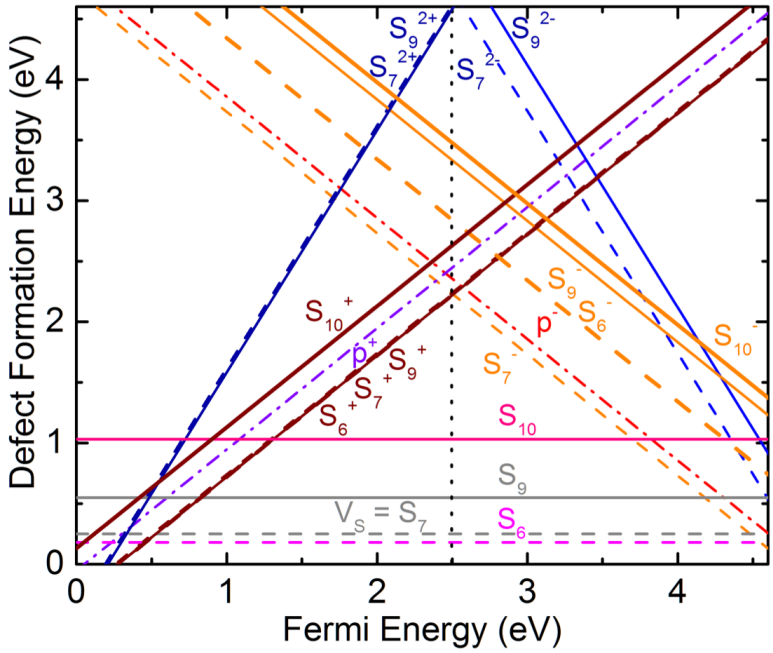

Figure 5.3 Defect formation energies of interstitials (solid lines), vacancies (dashed lines), and polarons (dash-dot lines) in α-S. The vertical dotted line gives the position of the Fermi level.

Figure 5.3 shows the calculated formation energies for the 18 distinct point defects examined in α-S. The slope of the lines corresponds to the charge of the defect; a horizontal line represents the formation energy of a neutral species, while positive (negative) sloped lines refer to defects with a positive (negative) charge. Lines with larger slopes correspond to doubly-charged defects. The charge neutrality condition establishes the position of the Fermi energy at 2.5 eV, and is shown as a vertical dotted line Figure 5.3.

Our calculations indicate that the dominant negative charge carriers in α-S are S vacancies (V_S^-, which appear as an S_7 ring with a negative charge, S_7^-) and electron polarons (p^-), with formation energies of 2.23 and 2.36 eV, respectively. A trio of defects comprise the most-prevalent positive localized charge carriers: positive S interstitials (S_i^+, equivalent to a positively charged S_9 ring, S_9^+), double S vacancies ($2V_S^+ = S_6^+$), and single S vacancies ($V_S^+ = S_7^+$). The formation energies for these carriers are 2.23, 2.23, and 2.25 eV, respectively. The hole polaron (p^+) has a slightly higher formation energy of 2.45 eV. The defect with the lowest formation energy overall

is the neutral S double vacancy ($2V_S = S_6$), with E_f = 0.18 eV. (Delocalized holes also play an important role in transport in α-S, and will be discussed separately below.)

Table 5.1 Calculated defect formation energies (E_f), equilibrium concentrations (C), hopping barriers (E_b), reorganization energies (λ), coupling integrals (H_{ab}), electronic transmission coefficients (κ), rate constants (k), mobilities (μ), and conductivities (σ) for α-S and Li_2S. Prior calculations on Li_2O_2 (Ref. 99) and Na_2O_2 (Ref.152) are also shown for comparison. †The hole polaron in *α-S* is kinetically unstable and spontaneously delocalizes. ‡Experimental data from Refs. 217-221

Defect Type	E_f (eV)	C (cm^{-3})	Adiabatic E_b (eV)	Diabatic E_b (eV)	λ (eV)	H_{ba} (eV)	κ	k (s^{-1})	μ ($cm^2/V/s$)	σ (S/cm)
					α-S					
p^- (Intra-ring)	2.36	9×10^{-18}	0.11	0.07	0.45	0.19	1	2×10^{11}	3×10^{-3}	4×10^{-39}
p^- (Inter-ring)			0.42	0.38	1.54	1×10^{-3}	0.012	4×10^{4}	2×10^{-7}	3×10^{-43}
p^+ (Intra-ring)†				0.00†	0.18	0.09				
p^+ (Inter-ring)†				0.023	0.09	1×10^{-5}	9×10^{-6}	4×10^{6}		
Delocalized hole									1-10‡	5×10^{-19}‡
S_7^-	2.23	2×10^{-15}	0.55					5×10^{3}	3×10^{-10}	7×10^{-44}
S_9^+	2.23	3×10^{-17}	1.62					6×10^{-15}	3×10^{-28}	1×10^{-63}
S_6^+	2.23	6×10^{-16}	---					---	---	---
S_7^+	2.25	1×10^{-15}	1.2					7×10^{-8}	3×10^{-21}	5×10^{-55}
					Li_2S					
p^+	1.95	4×10^{-11}	0.08	0.03	0.53	0.14	1	6×10^{10}	2×10^{-1}	2×10^{-30}
p^-				0.2	1.21	0.11	1	4×10^{8}		
V_{Li}^-	0.84	3×10^{8}	0.32					4×10^{7}	1×10^{-6}	6×10^{-17}
Li^+	0.84	1×10^{8}	0.52					2×10^{4}	1×10^{-9}	1×10^{-20}
F_{Li}	1.22	1×10^{2}								
F_S	1.45	2×10^{-2}								
Sch	2.36	1×10^{-17}								
					Li_2O_2					
p^+	0.95	1×10^{7}	0.42					7×10^{3}*	--	5×10^{-20}
V_{Li}^-	0.93	7×10^{7}	0.36					1×10^{5}*	6×10^{-9}	9×10^{-19}
					Na_2O_2					
p^+	0.9	1×10^{7}	0.47					5×10^{2}*	--	1×10^{-20}
V_{Na}^-	1.06	3×10^{4}	0.42					6×10^{3}*	9×10^{-10}	5×10^{-20}

We note that the formation energies for all of the charged defects considered are very high (greater than 2.2 eV); consequently, the concentrations of these carriers under equilibrium conditions will be negligible, as summarized in Table 5.1. For example, the highest concentration predicted for a charged defect is 2×10^{-15} cm^{-3} for S_7^-. To place this value in context, the

concentration of carriers in undoped Si (which is a poor conductor at room temperature) is 25 orders of magnitude higher.[222] In contrast, the neutral sulfur vacancy, V_S, has a relatively high concentration of 2×10^{16} cm^{-3}, yet it will not contribute to conductivity due to its neutrality.

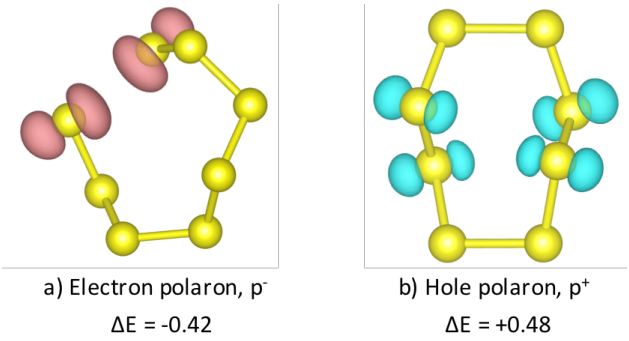

Figure 5.4 Magnetization density for (a) electron (p^-) and (b) hole (p^+) polarons in α-S. For clarity, only the S_8 molecule where the polaron localizes is shown. The localization energy, ΔE = Elocalized – Edelocalized, is shown below each polaron type.

Regarding the properties of polarons, the magnetization densities for both electron and hole polarons in α-S are shown in Figure 5.4. In the case of p^-, the extra electron localizes on one of the S-S bonds on a S_8 molecule. The shape of the occupied orbital suggests an anti-bonding σ* state. The presence of the additional electron results in an elongation of the bond from 2.05 to 2.65 Å. A comparison of the energies of localized (p^-) and delocalized electrons shows that localization is preferred by 0.42 eV. This is in very good agreement with a prior drift mobility experiment[223] that determined the p^- binding energy to be 0.48 eV.

In contrast to the more-localized nature of the electron polaron, the hole polaron (p^+) localizes on two pairs of S-S bonds, Figure 5.4b, located on opposite sides of an S_8 ring. This results in a slight distortion of the ring, wherein the S-S-S bond angles change from ~107° to ~102°, with insignificant change in the S-S bond lengths. We find that the p^+ are unstable with respect to the delocalized state by 0.48 eV.

5.3.2 Charge Carrier Mobility in α-S

The low equilibrium concentrations of charge carrying defects in α-S suggest that even a barrier-less charge hopping process will result in an extremely low conductivity. However, this conclusion assumes that *equilibrium* concentrations are established. In practice, however, battery operation involves the relatively rapid growth and decomposition of the REM at near-ambient temperatures. Such conditions may generate much higher, non-equilibrium carrier concentrations. This possibility motivates an examination of the mobility of charge carriers in α-S.

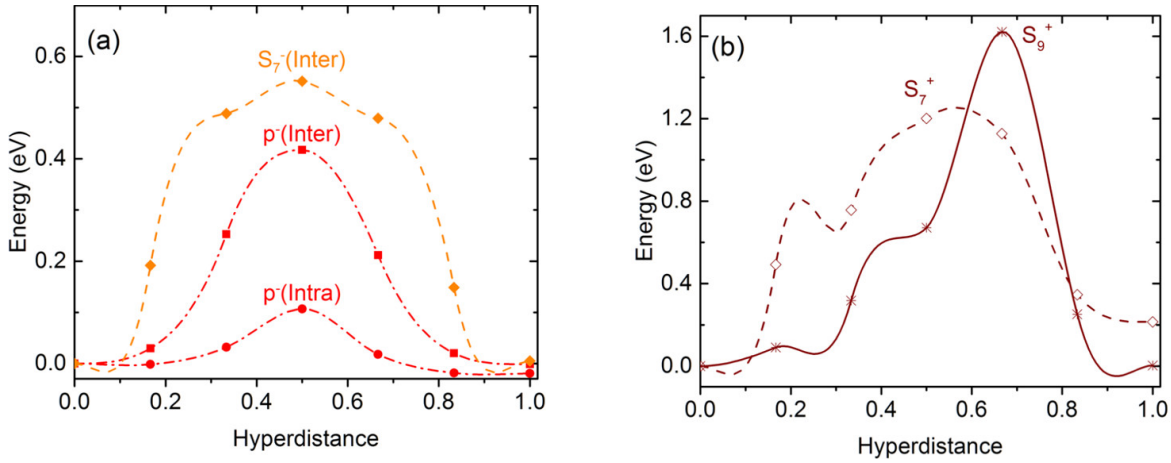

Figure 5.5 Activation energies (calculated with the CI-NEB) associated with the migration of dominant (a) negative and (b) positive charge carriers in α-S. "Inter" refers to hops between adjacent sulfur rings, while "Intra" refers to hops within the same ring. All hops in panel b are inter-ring hops.

In the adiabatic limit, mobility can be estimated from the migration energy barriers of the individual defects, calculated using the CI-NEB method.[106] Figure 5.5a shows the minimum energy pathways for the highest-concentration negatively-charged defects in α-S. For the ionic carriers, hopping was examined only between adjacent S_8 rings, i.e. inter-ring hops, as these hoping mechanisms are anticipated to be rate limiting due to their longer hopping distances (compared to intra-ring hops). In the case of S_7^-, migration occurs with an activation energy of 0.55 eV. By way of comparison, this value is 0.1 to 0.2 eV larger than the migration barrier for negative vacancies in Li_2O_2 and Na_2O_2,Table 5.1.[99, 152] Hopping of the electron polaron, p^-, has a slightly smaller inter-ring hopping barrier of 0.42 eV. Polaron hopping was also examined within a single S_8 molecule. These intra-ring hops have the lowest activation energy of any carrier considered in α-S, 0.11 eV. This value agrees well with the experimentally obtained value of 0.167 eV (assuming experiments refer to intra-ring hops).[223] Nevertheless, we emphasize that hopping via intra-ring processes alone cannot lead to charge transport over macroscopic distances; inter-ring processes constitute the rate-limiting steps.

Figure 5.5b illustrates the adiabatic hopping barriers for the two stable positively charged defects, S_7^+ and S_9^+. (Migration of p^+ was not considered due the fact that it is unstable with respect to the delocalized state.) S_9^+ exhibits a relatively high activation energy of 1.62 eV, while the predicted barrier for S_7^+ is 1.20 eV.

The calculations presented above have assumed adiabadicity of the charge transfer events. The validity of this assumption is assessed here using cDFT. All cDFT results are collected in Table 5.1, and compared with the adiabatic data previously described. We first discuss the behavior

of the electron polaron (p^-) in α-S, which our HSE_α calculations find to be stable (relative to a delocalized electron). The hopping barriers from cDFT for intra and inter ring electron polaron hops are 0.07 and 0.38 eV, respectively. As can be seen in Table 5.1, the agreement between HSE-NEB and cDFT-Marcus barriers is very good – the barriers predicted by the different methods differ by less than 40 meV.

Although the good agreement in migration barriers for p^- might suggest that all hops can be characterized as adiabatic, the value of the transmission coefficient, κ, suggests otherwise. More specifically, only the intra-ring process has a κ value of 1, which is indicative of adiabatic behavior. In contrast, the transmission coefficient for the inter-ring hop is very small (κ=0.012), indicating that diabatic effects are important. The nonadiabadicity of inter ring p^- transfer is due to the weak coupling between the initial and final states ($H_{ba} = 1\times10^{-3}$), which is consistent with the relatively large distance, 3.4 Å, between them. In total, inter-ring electron transfer exhibits a diabatic hopping rate constant k of 4×10^4 s^{-1}. This value is approximately 2 orders of magnitude smaller than the equivalent adiabatic rate constant. The values reported in Table 5.1 for the hopping rate, mobility, and conductivity of electron polarons account for the nonadiabaticity described above. The mobility estimated for intra-ring p^- migration is 3×10^{-3} $cm^2/V/s$, which is in close agreement with that determined in drift mobility experiments (6.2×10^{-4} $cm^2/V/s$), assuming the same hopping mechanism is probed experimentallly.[223]

Regarding hole polarons, the cDFT calculations confirm the results from the previously-described hybrid functional calculations, indicating that p^+ are unstable. For example, the barrier for an intra-ring hop of p^+ vanishes when charge is constrained to reside on two neighboring S-atoms. This suggests that positive charge is delocalized at least across a single sulfur ring. However, hole polaron transfer to an adjacent ring is predicted to be slow and clearly nonadiabatic, as inferred from the transmission coefficient value $\kappa\sim10^{-6}$. Nevertheless, the inter-ring hole polaron transfer barrier of 23 meV is smaller than thermal energy at room temperature and therefore the hole polaron in α-S is expected to delocalize over distances larger than that of a single S_8 ring. This hypothesis was confirmed using nonadiabatic Ehrenfest nuclear-electron dynamics, as detailed in the Supporting Information.

Conductivity in the band-like regime is mainly governed by the scattering of charge carriers by impurities and vibrational modes of the crystal, which in turn determine their mean free path

(or, equivalently, the mean free time, τ); thus, transition state and Marcus theory, are not applicable. In principle, the impact of impurities on the mean free path could be obtained through *ab initio* methods, by combining the non-equilibrium Green's function (NEGF) formalism with DFT.[224] Within this method, it is possible to derive the transmission coefficient due to scattering from each impurity type. Combining this data with the impurity concentration yields the contribution of the impurities to the mean free path. Although the presence of impurities in molecular crystals can reduce carrier mobility significantly, (e.g. up to two orders of magnitude in pentacene[225]), the mean free path in these systems is most strongly influenced by scattering from the vibrational modes of the crystal, in particular from the acoustic modes.[220, 226] These low frequency modes are derived from intermolecular forces. In principle, scattering from vibrations could be characterized through an exhaustive analysis of the electron-phonon coupling,[226-227] however, accurately describing weak intermolecular interactions (and their associated low frequency modes), remains a significant challenge, and is not practical at present. Recombination of carriers is another feature that complicates the study of mobility in α-S. As we discuss below, holes move much faster than electrons in α-S (due to band conduction of the former *vs*. hopping for the latter), making the impact of their recombination to the conductivity non-negligible.[217]

5.3.3 Conductivity and Diffusion Length in α-S

As expected from the extremely low equilibrium concentrations of charged defects, the conductivity of α-S arising from hopping mechanisms (which are generally slow processes) is negligible, Table 1. For example, the inter-ring migration of electron polarons, p^-, is the process with the highest hopping-like conductivity of those that contribute to long-range transport. Nevertheless, the value calculated for its conductivity, $\sigma = 3\times10^{-43}$ S/cm, is extremely small. Similarly, the highest hopping-type conductivity attributed to positive carriers is also vanishingly-small, and arises from vacancy migration, $V_S^+ = S_7^+$, with $\sigma = 5\times10^{-55}$ S/cm.

However, we have shown that holes in α-S are delocalized and thus migrate via a band conduction mechanism, which is faster than any hopping process. As previously mentioned, analysis of the band conductivity for charge carriers in molecular crystals is a non-accessible quantity with current *ab initio* methods. Conversely, the experimental mobility of holes in α-S has been measured through drift experiments, and is in the range μ = 1-10 $cm^2/V/s$,[217, 219-220, 228] at 300 K. This value is 7 orders of magnitude larger than for any of the hopping mechanisms considered

here. Experiments also show that the hole mobility decays with temperature as $\mu \propto T^{-n}$ with n = 1.6, 1.1, and 1.7 in the [100], [010], and [001] directions, respectively.[228] This is also consistent with a band conduction model, where the mobility is expected to decay as $\mu \propto T^{-1.5}$ due to scattering from acoustic modes (for optical modes $\mu \propto T^{-0.5}$).[229]

The calculated diffusivities and mobilities were used to establish the migration lengths for charge carriers in α-S. (In the case of delocalized holes, the experimental mobility was used.) These lengths provide an upper bound for the thickness of a S film (i.e., maximum S loading) that can be traversed by these carriers during cell operation at a given C-rate. Assuming a uniform film of α-S with density $\rho_{\alpha\text{-S}}$ = 2 g/cm^3, a loading target[198] of 6 mg/cm^2 results in a S film with a thickness of 30 μm. Based on the mobility data shown in Table 5.1, and assuming C-rates (discharge durations) of 1C (3600 sec), C/5 (18000 sec), and C/10 (36000 sec), Table 5.2 summarizes the maximum diffusion lengths, $L = \sqrt{Dt}$, for the dominant hopping-type carriers in α-S: p^-, S_7^-, S_7^+, and S_9^+. The maximum diffusion lengths for p^- are 131, 93, and 41 μm for rates of C/10, C/5 and 1C, respectively, assuming inter-ring hopping between S_8 molecules. This suggests that polarons in *α-S* have sufficient mobility to traverse typical film distances corresponding to the JCESR target S loading. In contrast, the diffusion lengths of the dominant ionic species (S_7^-, S_7^+, and $S_9^{+)}$ are all well below the thickness target.

Table 5.2 Charge carrier diffusion (L) and drift (L_d) lengths (in μm) for the predominant charge-carrying species in α-S and Li_2S as a function of rate.

Defect Type	C/10		C/5		1C	
	L	L_d	L	L_d	L	L_d
			α-S			
p^- (Inter-ring)	131	258	93	182	41	82
S_7^-	5	10	4	7	2	3
S_7^+	0	0	0	0	0	0
S_9^+	0	0	0	0	0	0
Delocalized holes		106		106		105
			Li_2S			
V_{Li}^-	345	678	244	479	109	214
Li^+	11	22	8	16	4	7
p^+	52000	100000	37000	73000	17000	33000

The estimates for the diffusion lengths provided above are based on diffusion in the presence of a concentration gradient. Alternatively, in the presence of an electric field, the *drift length*, L_d, of a charged species is a more relevant measure of a charge carrier's typical transport length. L_d is given in terms of the mobility, μ: $L_d = \sqrt{\mu V t}$. Here V is the voltage drop across the S film, for which we adopt 0.1 V as a plausible value, and t is the time. With these assumptions, our calculations reveal the drift lengths of the hopping-type carriers are roughly double their diffusion lengths, Table 5.2. Despite this increase, only p^- have sufficient mobility to transit the targeted film thickness. Application of the drift length analysis to delocalized holes in α-S, Table 5.2, shows that the high mobility of these carriers results in extremely long drift lengths, on the order of 0.1 to 1 m.

The preceding discussion indicates that the mobility of delocalized holes and p^- are sufficient to enable high S loadings (and high capacity) in Li-S cells. Nevertheless, the experimental conductivity of α-S has been reported to be extremely small, ~5×10^{-19} S/cm.[221] Taken together, these data – sufficient mobility, but poor conductivity – point to low carrier concentrations as the primary obstacle to effective charge transport in α-S. (For example, the large bandgap for α-S suggests that the concentration of free holes at room temperature will also be very small.[93]) In an earlier study, we explored electrical conductivity limitations in Li_2O_2 in the related Li-O_2 system. There, a cathode conductivity of 10^{-11} S/cm was suggested as a target for achieving efficient operation.[99] Adopting that value here, and using the calculated mobility for p^-, a carrier concentration of 10^{15} cm^{-3} is required to achieve the conductivity target. This concentration is 33 orders of magnitude larger than the equilibrium p^- concentration listed in Table 5.1. Similarly, for delocalized holes, the experimental conductivity and mobility data suggest that an increase in carrier concentration of approximately 8 orders of magnitude is required. Thus, strategies for improving transport in α-S should target increasing the concentrations of free holes and/or electron polarons.

5.3.4 Intrinsic Defects in Li_2S

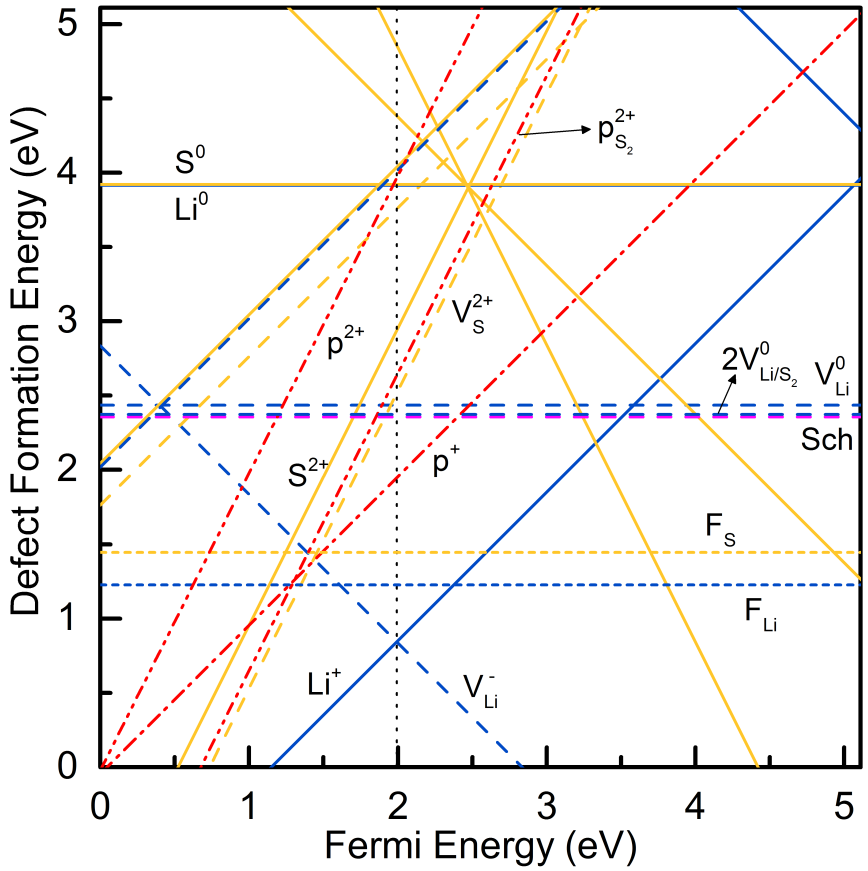

Figure 5.6 Calculated formation energies for defects in Li_2S. Yellow lines represent ionic defects on the S sublattice, blue lines correspond to ionic defects on the Li sublattice, and red lines refer to polarons. Solid lines are interstitials, while dashed lines

Figure 5.6 shows defect formation energies in Li_2S. The predominant defect species, i.e. those having the lowest formation energies, are the negatively charged Lithium vacancy (V_{Li}^-), and the positively charged Lithium interstitial (Li^+), both having formation energies of 0.84 eV. The corresponding equilibrium concentrations are 3×10^8 and 1×10^8 cm^{-3}, respectively; these values are 2 orders of magnitude lower than the carrier concentration in undoped Si.[222] The lowest-energy neutral defect is the Li Frenkel pair (comprised of a Li interstitial-vacancy pair), with a formation energy of 1.23 eV.

Our prediction that V_{Li}^- and Li^+ are the highest-concentration equilibrium charge carriers in Li_2S agrees with the findings of Moradabadi[103] *et al.*, but differs from the conclusions drawn in two other studies.[92,105] For example, Kim *et al.*[92] found that the dominant carriers are V_{Li}^- and positively two charged S vacancies (V_S^{2+}), with formation energies of 1.31 eV. Alternatively,

Mukherjee *et al.*[105] reported V_{Li}^{-} and hole polarons (p^{+}) as the predominant species, with formation energies (1.40 eV) similar to that of Kim *et al*. These differences can be explained by the omission of interstitial defects in these earlier studies. The present calculations reveal that Li^{+} interstitials are the lowest energy positive charge carrier in Li_2S. Indeed, the removal Li^{+} from our defect diagram (Figure 5.6) would shift the Fermi energy to a position similar to that reported by these earlier studies (1.3 – 1.4 eV), reflecting charge balance between V_{Li}^{-} and p^{+}/V_S^{2+}. (p^{+} and V_S^{2+} are the same positive carriers reported in Refs. [92,105].) We emphasize that an accurate accounting of charge carrier concentrations can only be achieved if a comprehensive sampling of formation energies for all relevant defects – including interstitials – is performed.

The possibility for non-equilibrium carrier concentrations induced by rapid growth/dissolution of Li_2S during battery cycling prompts us to examine carriers beyond the ionic species described above, i.e., polarons. The stability of electron and hole polarons in Li_2S were explored by adding or removing a single electron from the computational cell, and by applying initial lattice distortions consistent with the presence/absence of localized charge on a S ion. For example, the presence of a hole polaron localized on a S ion (resulting in a charge state of S^{1-}) will reduce electrostatic attraction with nearest-neighbor Li ions and thereby increase Li-S distances. In contrast, the presence of an electron polaron will result in formation of an S^{3-} ion, which will more strongly attract adjacent Li^{+}.

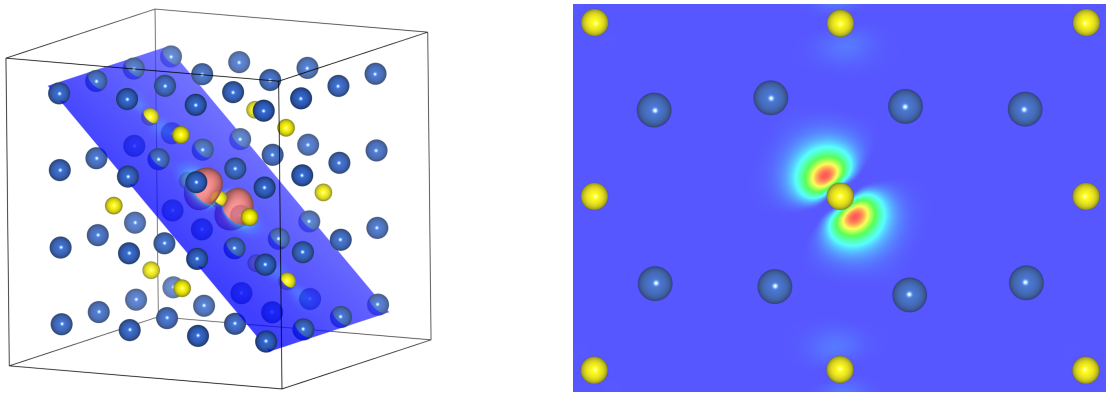

Figure 5.7 (Left) Magnetization density isosurface for the hole polaron in Li_2S. (Right) Contour plot of the magnetization density in a (110) plane. Red and blue areas represent magnetization densities of 0.06 e/bohr^3 and 0 e/bohr^3, respectively

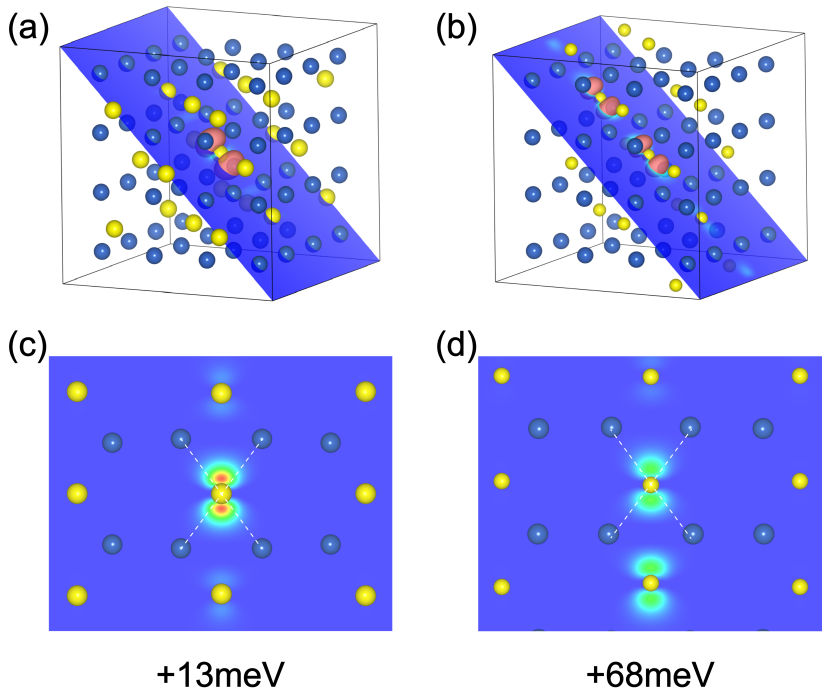

Figure 5.8 (a) and (b): Magnetization density isosurfaces for metastable hole polarons in Li_2S. (c) and (d): contour plots of the magnetization density on a (110) plane. Red and blue areas represent magnetization densities of 0.06 e/bohr^3 and 0 e/bohr^3, respectively. Energies given at the bottom represent the relative energy of these polarons with respect to that of the lowest energy polaron configuration discussed in the main text. Blue and yellow spheres represent Li and S atoms, respectively. Dotted white lines represent the symmetry-identical orientations of the lowest-energy hole polaron configuration.

Regarding electron polarons, p^-, our attempts to localize an additional electron on a nominally S^{2-} ion were not successful. Several initial lattice distortions were attempted; nevertheless, in all cases the resulting relaxed structure resembled undistorted Li_2S, with the extra electron delocalized over the entire computational cell. In contrast, hole polarons, p^+, do localize on S ions. The formation energy for p^+ is high, 1.95 eV (see Table 5.1 and Figure 5.6), with a correspondingly low equilibrium concentration of 4×10^{-11} cm^{-3}. Furthermore, the localized hole is more stable than a delocalized hole by 0.07 eV. Figure 5.6 (left) shows the magnetization density isosurface for p^+, indicating the presence of an unpaired electron localized on a S ion. The spatial distribution of this electron is consistent with that of a 3p-orbital aligned towards a pair of nearest-neighbor Li-ions, Figure 5.6 (right). The Li-ions closest to the localized charge exhibit an enlarged Li-S distance of 2.78 Å, which should be compared to 2.46 Å in the absence of p^+. (Two metastable p^+ with distinct local geometries were also identified, and are shown in Figure 5.8. These configurations are less stable by 13 and 68 meV, respectively.) The charge state of an S anion in the presence of a hole polaron was calculated using a Bader charge analysis.[191-192] As expected, the total number of

valence electrons, 7.2, is significantly smaller in the presence of p^+ than for a typical S^{2-} anion, wherein the number of electrons ranges from 7.9 to 8.0.

Our observation of self-trapping of holes on sulfur ions in Li_2S agrees with the calculations of Mukherjee *et al.*[105] Nevertheless, Ref. [92] reported a stability trend opposite to those of Mukherjee and the present calculations, with p^- being self-trapped and p^+ being unstable with respect to delocalization. Of course, the formation of p^- implies the existence of an S^{3-} anion, which our intuition suggests would be highly unstable. Moreover, the charge density plot used in Ref. [92] to substantiate the formation of S^{3-} does not show a distribution consistent with occupation of a 4s orbital, calling into question whether localization of an additional electron has occurred.

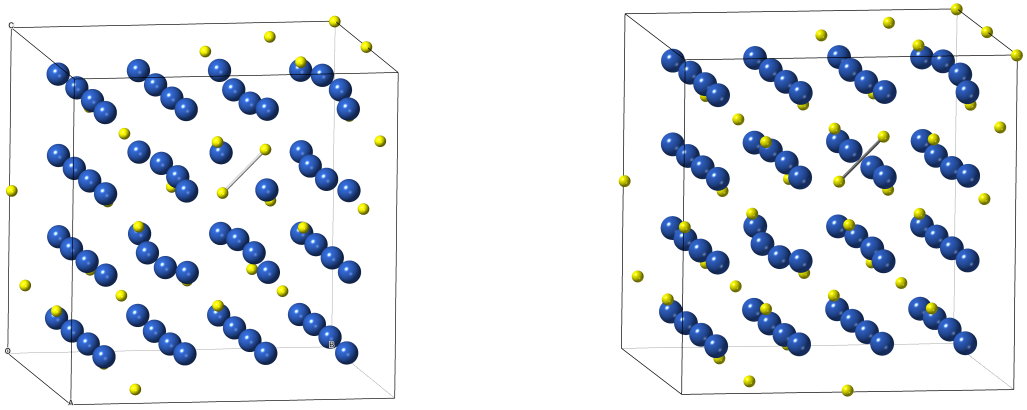

(a) S_2^{2-} formed in the presence of 2 V_{Li}^0 (b) S_2^{2-} formed from the combination of 2 p^+

Figure 5.9 Structure of the Li_2S supercell containing S_2^{2-} dimers formed from the insertion of: (a) two neutral Li vacancies, or (b) two hole polarons. Blue and yellow spheres represent Li and S atoms, respectively.

Finally, the formation of S_2^{2-} dimers was also investigated by introducing two neutral Li vacancies, V_{Li}^0, or by removing two electrons (equivalent to the introduction of two p^+) from the simulation cell. These calculations were motivated by the presence of S_2^{2-} dimers in iron pyrite, FeS_2, where the S-S distance is 2.16 Å.[230] Dimer formation was induced by initially shortening the distance between adjacent S ions. Figure 5.9 illustrates the geometries of these relaxed S_2^{2-} dimers. The resulting S_2^{2-} dimers exhibited S-S distances of 2.10 to 2.13 Å. For both scenarios, formation of S_2^{2-} was energetically preferred over the formation of pairs of isolated vacancies or hole polarons. For example, the formation energy of two V_{Li}^0 and S_2^{2-} is 2.37 eV, while the sum of two single V_{Li}^0 is much higher, 4.86 eV. Similarly, E_f for two p^+ and an S_2^{2-} is 2.62 eV, which is well below that for two p^+, 3.90 eV. These data indicate that it is energetically favorable for p^+ to localize as pairs on covalently bonded S_2^{2-} dimers. If the charging process involves an initial

delithiation step, then the formation of S_2^{-2} dimers would likely be a component of that reaction pathway.

5.3.5 Charge Carrier Mobility in Li_2S

The mobilities of Li^+, V_{Li}^-, and p^+ were evaluated in the adiabatic limit using the HSE_α functional and the CI-NEB. Figure 5.10 shows the minimum energy pathways associated with the migration of these carriers.

In the case of Li^+, two migration mechanisms were examined between neighboring interstitial sites, a simple interstitial hop, and interstitialcy diffusion. The interstitialcy mechanism corresponds to a Li^+ migrating towards an occupied Li site, while the ion occupying that site simultaneously hops to a neighboring interstitial position.[231] Our calculations predict that the interstitialcy mechanism has a much lower energy barrier (E_a = 0.52 eV) than the interstitial process (E_a = 1.86 eV). Based on these activation energies, the corresponding mobilities for these carriers are 6×10^{-10} and 2×10^{-32} $cm^2/V/s$, respectively. Moradabadi *et al.* calculated a Li^+ interstital migration barrier of 0.47eV using the PBE-GGA functional.[103]

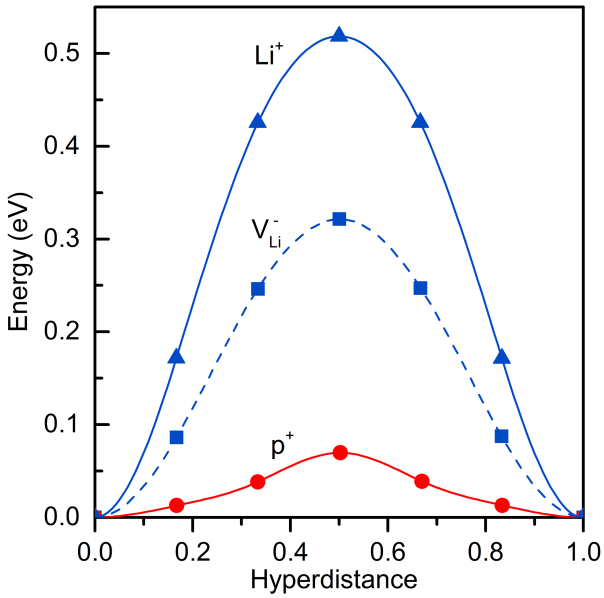

Figure 5.10 Calculated minimum energy pathways for migration of negative Li vacancies (V^{Li-}), positive lithium interstitials (Li^+), and hole polarons (p+) in Li_2S.

For V_{Li}^- migration, there is only one symmetry-distinct Li vacancy site and only one migration pathway between nearest-neighbor sites was considered. The calculated barrier for V_{Li}^- migration, 0.32 eV, is 0.2 eV smaller than that for Li interstitials. This barrier yields a mobility of 1×10^{-6}

$cm^2/V/s$, which is approximately four orders of magnitude larger than that for Li^+ mobility. Our calculated energy barrier (evaluated using the HSE_{48} functional) is in very good agreement with those reported by earlier studies employing the semi-local PBE-GGA functional (E_a = 0.29 eV and 0.27 eV)[102-103] and the HSE06 hybrid functional (E_a = 0.29 eV)[105].

For hole polarons, a very small activation energy of 0.08 eV was calculated for hopping between adjacent S ions. (The corresponding mobility is 3×10^{-2} $cm^2/V/s$.) This value is well-matched to that of a previous study that predicted a hopping barrier of 0.09eV.[105] The predicted hopping barrier is much smaller than that observed for p^+ migration in Li_2O_2, Na_2O_2, and NaO_2, where typical barriers are several tenths of an eV.[99, 152] On the other hand, the behavior of p^+ in Li_2S is similar to that of hole polarons in MgO, which were reported to have a barrier of only 0.11 eV and mobility of 6×10^{-3} $cm^2/V/s$.[151] These data suggest that hole transport in Li_2S can be more facile than in the discharge products of, e.g., metal-air batteries.

cDFT calculations confirm that both electron and hole polaron transfer reactions are adiabatic (κ=1); therefore, the results from HSE-NEB calculations can be used with confidence. Moreover, the barrier for hopping of p^+ estimated using cDFT, 0.03 eV, differs only by 50 meV from the corresponding HSE_α-NEB value described above. Aside from this small difference in the barriers, the rates, mobilities, and conductivities predicted by both approaches (either HSE_α-NEB + harmonic transition state theory or cDFT + Marcus theory) are equal.

While we were unable to localize the electron polaron using HSE_α, localization of p^- can be achieved with cDFT. [We emphasize, however, that cDFT does not allow for an estimate of the self-trapping energy of p^-, and our earlier conclusion (based on HSE calculations) that electron polarons do not prefer to localize in Li_2S remains valid.] Nevertheless, cDFT does provide an opportunity to assess the mobility of p^-: these calculations yield a hopping barrier of 0.20 eV and rate constant of 4.3×10^8 s^{-1}, Table 5.1. Comparing the barriers and charge transfer rates in Table 5.1 for hole (6.0×10^{10} s^{-1}) and electron (4.3×10^8 s^{-1}) polarons, it is apparent that hole polarons are the most mobile electronic carriers in Li_2S.

5.3.6 Conductivity and Diffusion Length in Li_2S

Table 5.2 summarizes the transport properties of the three relevant defects in Li_2S identified here – Li^+, V_{Li}^-, and p^+ – and for comparison revisits the dominant defect chemistry for the peroxides, Li_2O_2 and Na_2O_2.[99, 152] The individual contributions of these carriers to the equilibrium

ionic and electronic conductivity of Li_2S are evaluated in terms of their concentrations and mobilities, $\sigma = qC\mu$. V_{Li}^- exhibits the highest conductivity of the possible carriers in Li_2S, 6×10^{-17} S/cm. Its conductivity is 2-3 orders of magnitude larger than Li^+ interstitials, and for the analogous cation vacancies in Li_2O_2 and Na_2O_2. This higher conductivity results from a combination of relatively larger concentrations and mobilities of V_{Li}^- in Li_2S. Nevertheless, a conductivity on the order of 10^{-17} S/cm is an extremely low value. In practice, however, the presence of a higher, non-equilibrium carrier concentration may be achieved due to the rapid formation/dissolution of Li_2S during battery operation. Measurements of the ionic conductivity of Li_2S would be very helpful in identifying these non-equilibrium effects.

Regarding electronic conductivity in Li_2S, the negligible equilibrium concentration of p^+, 4×10^{-11} cm^{-3}, results in an extremely low (effectively zero) conductivity, 2×10^{-30} S/cm. This conductivity is 10 orders of magnitude smaller than in the peroxides,[99, 152] and approaches the value estimated for MgO, 3×10^{-36}.[151] Although p^+ in Li_2S have relatively high mobilities, their low concentration offsets the benefits conveyed by these mobilities. Strategies for increasing the carrier concentration could exploit the moderate mobility of p^+ to improve the electronic conductivity.[232]

We next consider whether the diffusivity and mobility of the dominant charge carriers in Li_2S are sufficient to access the full capacity of a Li-S cell. To determine this, a target S loading of 6 mg/cm^2 is adopted (as discussed above), and we further assume all S is reduced during discharge and forms a uniform film of Li_2S that covers the cathode support. Based on the density of Li_2S, such a film will have a thickness of approximately 50 μm. During charging, charge transport through this film will be necessary; Table 5.2 summarizes whether the identified carriers have sufficient mobility to transit the film, assuming charging rates of 1C, C/5, and C/10. The data reveal that both V_{Li}^- and p^+ have adequate mobility to cross the film for all rates considered (based on their respective diffusion coefficients). Similarly, the drift length (assuming a voltage drop of 0.1 V across the Li_2S film) is sufficient to accommodate a 50 μm film. (The drift length is twice larger than the diffusion length.) In contrast, for all rates considered, the mobility of Li^+ interstitials is too small to contribute to charge transport across these relatively thick films.

These data indicate that the mobility of V_{Li}^- and p^+ in Li_2S are sufficient to enable high active-material loadings (and high capacity) in Li-S cells. Thus, it is the low equilibrium concentration of carriers that is the primary limitation to effective charge transport. In an earlier study, we explored electrical conductivity limitations in Li_2O_2 in the related Li-O_2 system. There, a cathode

conductivity of 10^{-11} S/cm was suggested as a target for achieving efficient operation.[99] Adopting that value here, and using the calculated mobility for p^+, we determine that a carrier concentration of 10^8 cm^{-3} is required to achieve the conductivity target. This concentration is 19 orders of magnitude larger than the equilibrium p^+ concentration listed in Table 5.2.

5.4 Discussion

It is worthwhile to reexamine the previous experimental and theoretical studies of the electronic structure and polaron mobility in α-S. Firstly, α-S is a molecular solid formed by S_8 rings that interact weakly through van der Waals forces. Thus, many of the electronic properties of α-S can be roughly understood from the molecular S_8 vapor phase. Indeed, the photoemission data for α-S and molecular S_8 are nearly identical,[218, 233-234] apart from the broadening of the lines in the former. As expected in a molecular solid formed by such a small S_8 units, the electron-hole interactions are very large. Thus, the molecular excitonic peaks observed in optical absorption experiments in the ~3-5 eV range lie far below the photoemission gap, which is estimated to be close to 8-9 eV.[234]

Consistent with its molecular nature, the dispersion of the bands in α-S is expected to be very small. Based on optical experiments, Spear and co-workers appraised the valence band bandwidth to be 0.80 eV, while the conduction band only spanned 0.01 eV.[223, 233] Consequently, the binding energies that stabilize a polaron are negligible for electron polarons, and significantly larger for hole polarons. In fact, free hole polarons (i.e. hole polarons not bonded to any defect) have not been observed in α-S, while free electron polarons have been detected with a polaron binding energy of 0.48 eV.[218, 223] As mentioned earlier, this binding energy is in good agreement with the value calculated in the present study, 0.42 eV.

As described above, our calculations predict that hole polarons in S cannot be localized on a single bond or S_8 ring. This leads us to conclude that hole conduction in sulfur is not polaronic in nature. This conclusion is consistent with experimental conductivity studies, which show that the hole life-time in S is less than 20 nanoseconds, and that hole transfer is categorized as narrow band conduction rather than hopping.[219] In the band conduction regime, cDFT coupled with Marcus theory and DFT with transition state theory are inadequate to characterize the conduction mechanism and conductivity. Instead, hole transfer in S should be treated with nonadiabatic quantum dynamics based on the time-dependent Schrödinger equation. This approach naturally

includes all possible conduction mechanisms without predefined assumptions. Along these lines, using Ehrenfest dynamics we observed that an initially localized hole polaron (on a single S_8 ring) delocalizes within 10 fs onto p-type orbitals spread across all atoms in the simulation cell (without changes in S-S bond lengths). These calculations agree well with the experimental results that show that holes in sulfur are conducted via a band mechanism, rather than via polaron hopping.

Several groups studied electron and hole diffusion in α-S during the 1960's.[219, 223] These studies concluded that at low temperatures (below 300 K) the diffusion of holes is controlled by a trapping mechanism, i.e. the holes are trapped at intrinsic defects in the α-S crystal and can diffuse with a ~0.22 eV activation barrier.[219, 223] At higher temperatures the trapping diffusion is saturated and the hole transport changes to a lattice scattering regime (i.e. conduction through holes in the valence band).[219, 223] In the present work, we do not consider the transport of polarons bonded to any defect/trap, but instead focus on the diffusion of free polarons. In that context, it is most appropriate to compare our results to the higher temperature experiments. In this latter scenario, our prediction of delocalized holes agrees very well with the band-like conduction observed in experiments.

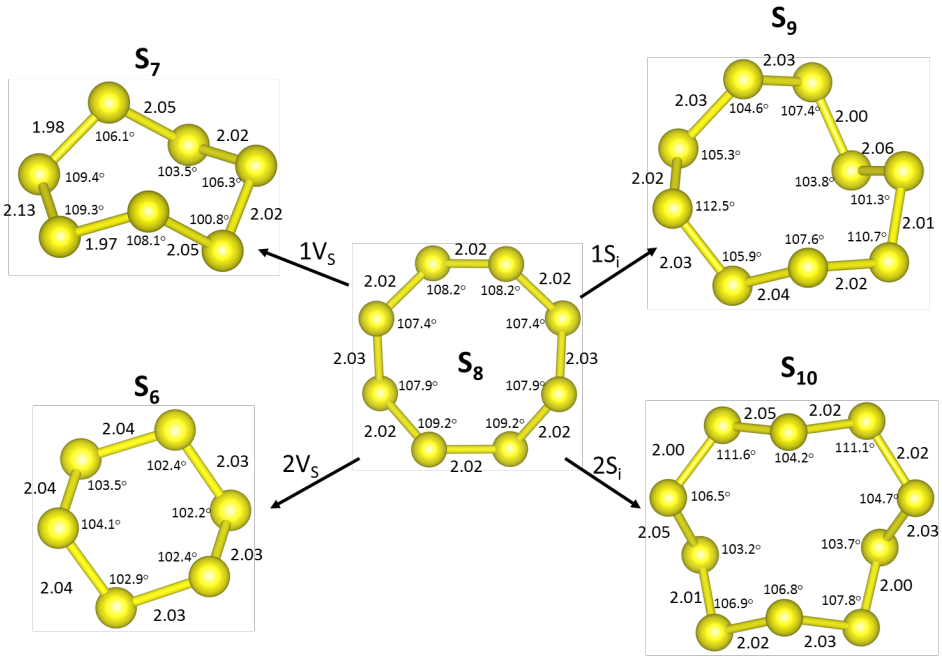

Figure 5.11 Calculated structures of various neutral S_x (x=6 to10) rings in α-S. The S_8 ring is the expected molecular unit in the defect-free crystal structure. S6 and S_7 correspond to ring structures formed upon the addition of 1 or 2 vacancies, respectively. Similarly, S_9 and S_{10} result from the addition of 1 or 2 interstitials.

We have performed an analysis of the alignment of the hole (electron) polaron states relative to the top (bottom) of the valence (conduction) band in the different S_x (x=6-10) rings in α-S. The analysis is based on the formation energies of the neutral, positively, and negatively charged rings. These formation energies are shown in Table 5.1 of the main text and repeated in Table 5.3 for convenience. The structures of the neutral S_x rings are shown in Figure 5.11.

By subtracting the formation energy of the positively (negatively) charged S_x ring from the formation energy of the neutral ring it is possible to obtain the energy for a localized hole (electron) polaron for that ring configuration. Comparing those energies to the formation energies of the delocalized holes (electrons), which are also shown in Table 5.3, allows us to determine the energy position of a localized hole (electron) polaron relative to the top (bottom) of the valence (conduction) band. These data are shown in Table 5.3 and Figure 5.12.

Table 5.3 Formation energies, E_f, of various charged and neutral S_x rings (x=6-10) in in α-S, and stabilization energies of hole and electron polarons compared to the delocalized states. All energies are in eV.

Defect Type	E_f Neutral Defect	E_f Positive Defect	E_f Negative Defect	Energy of h^+ relative to delocalized h^+ in α-S[a]	Energy of e^- relative to delocalized e^- in α-S[a]
S_6	0.18	2.22	2.84	0.08	-0.12
S_7	0.25	2.24	2.23	0.03	-0.80
S_8	-	2.44	2.36	0.48	-0.42
S_9	0.56	2.22	3.33	-0.30	-0.01
S_{10}	1.03	2.63	3.48	-0.36	-0.33
Delocalized electrons/holes	-	1.96[b]	2.78[b]	-	-

[a]The energies are calculated as previously described in the present Supplementary Material. [b]Evaluated for delocalized holes as the difference: [$E_f(S_8^+)$ – h^+ stabilization energy], and similarly for the delocalized electron, [$E_f(S_8^-)$ – e^- stabilization energy].

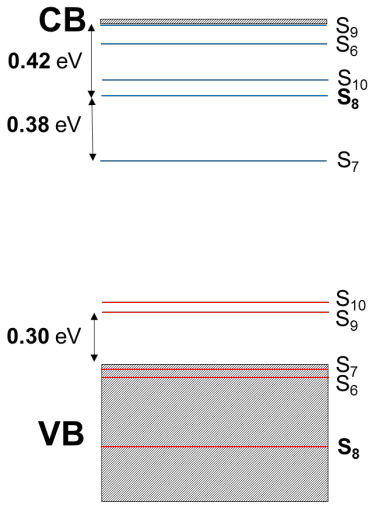

Figure 5.12 Schematic of the estimated energy levels of hole (red lines) and electron (blue lines) polarons in different Sx rings in α-S with respect to the valence (VB) and conduction (CB) bands. Hole polarons occupying the S_6, S_7, and S_8 rings have energies that lie within the VB, and thus will delocalize into band-like states.

It can be concluded that hole polarons are only stable in S_9 and S_{10} rings, implying that these rings can act as hole polaron traps. In contrast, electron polarons are stable in all the studied S_x rings. Furthermore, electron polarons are most stable in S_7 rings, which are 0.38 eV more stable than in S_8 rings, Figure 5.12. This implies that the electrons will be transported by means of polaronic hopping between S_8 rings, with S_7 rings as traps.

An analysis of the formation energies of positively charged S_x (x=6-10) rings relative to the formation energies of the neutral S_x rings (Figure 5.11) in α-S allows us to identify S_9 or S_{10} rings as the low temperature traps observed experimentally[219, 223]. In these two rings, localizing a positive charge is more favorable than the delocalized solution by 0.30 and 0.36 eV, respectively. Although the localization energy is larger for S_{10} rings, most likely the experimental signal of hole traps comes from S_9 rings, since their formation energy is much lower than that of S_{10} rings. Importantly, the calculated localization energy in S_9 rings, 0.30 eV is very close to the experimental activation barrier, 0.22 eV. [219, 223] This finding confirms the hypothesis of Gill et al., who claimed that hole traps in α-S are formed from native defects.[219] (Other authors assumed that the hole traps originate from extrinsic defects.[220])

Regarding the migration of electron polarons, two temperature regimes were again identified in experiments.[219, 223] At low temperatures (below 275 K), and similar to hole transport, a trapping mechanism with a ~0.40 eV barrier dominates. At higher temperatures, instead of passing to the lattice scatter regime, a free electron polaron hopping with a ~0.20 eV apparent activation barrier

was reported as the dominant mechanism.[219, 223] Although the experimental barrier of ~0.20 eV is relatively close to the 0.37 eV predicted barrier in our diabatic model, the discrepancy between these values warrants additional discussion. First, the apparent activation energies from experiments are derived from Arrhenius slopes; therefore, any temperature-dependence in the pre-exponential factor is included in the barrier. This is noteworthy since in Marcus theory the prefactor is (weakly) temperature-dependent. Therefore, both computed and experimental estimates for the effective or apparent barrier from an Arrhenius analysis will include the temperature dependence of the prefactor and the apparent barrier will differ slightly from the barrier values reported in Table 1. Additional factors contributing to this discrepancy are the high concentration of intrinsic defects in the samples (10^{14} electron traps per cm^{-3} in the purest vapor grown samples) and the reported 15% error in the experimental estimation of the barriers.

To identify the electron polaron traps in α-S at low temperature, a similar analysis to the one used for hole polarons was conducted. This analysis reveals that S_7 is the only S_x ring in α-S where localizing an electron is more favorable than in S_8 rings (by 0.38 eV). This energy difference is close to the estimate of 0.40 eV for the activation of electrons at low temperature made by Gill et al. based on measurements on vapor grown samples, corresponding to an electron hop from a S_7 to a S_8 ring. [219, 223]

Regarding Li_2S, our hybrid functional calculations indicate that hole polarons localized on S ions are stable, while electron polarons are not. Using cDFT, we can nevertheless force the localization of both hole and electron polarons and subsequently evaluate their migration barriers. The values reported in Table 5.1 indicate that electron polaron transfer in Li_2S is much slower than hole transfer, mainly due to the larger reorganization energy required for migration of electron polarons. Based on other recent DFT calculations, hole polaron migration is also predicted to be much faster in Li_2S_2,[104] a possible intermediate product in Li-S batteries. Taken together, these experimental and computational studies suggest that hole transport can be fast in α-S, Li_2S, and Li_2S_2; this observation implies that the performance of Li-S batteries can be improved (via enhanced electronic transport) by increasing the concentration of holes in these redox end members.

5.5 Conclusion

Understanding charge transport mechanisms in sulfur and Li_2S is a prerequisite for improving the capacity, efficiency, and cycle life of Li-S batteries. In α-S, these mechanisms have remained a matter of debate for more than 4 decades. The present study clarifies these mechanisms – in both the adiabatic and nonadiabatic charge transfer regimes – by employing a combination of hybrid-functional-based and constrained density functional theory calculations. The most significant outcomes of these calculations are summarized below.

Charged defects in both α-S and Li_2S are predicted to have high formation energies, resulting in negligible equilibrium carrier concentrations. In contrast, both compounds exhibit high mobilities for a subset of these carriers: in α-S, electron polarons and delocalized holes are the most mobile, whereas Li vacancies and hole polarons dominate in Li_2S. Importantly, analysis of the drift length for these species reveals that they have sufficient mobility to transit α-S and Li_2S films with thicknesses consistent with the JCESR sulfur loading targets. Thus, strategies to improve the conductivity of these materials should focus on increasing carrier concentrations beyond their equilibrium values.

In α-S, our calculations demonstrate that electrons can localize into polarons. Polaronic transfer within a single S_8 ring is predicted to be fast (10^{11} s^{-1}) and adiabatic. In contrast, polaron hopping between two adjacent S_8 rings is nonadiabatic, and much slower (10^4 s^{-1}). Neglecting nonadiabadicity, as is commonly done in DFT and transition state theory calculations, would overestimate these rate constants (and consequently also the mobility and the conductivity) by two orders of magnitude. This gap highlights the importance of going beyond the Born-Oppenheimer approximation by including nonadiabatic effects in computational studies of charge transfer kinetics in battery materials. Computational methods that combine cDFT with Marcus theory can treat both adiabatic and nonadiabatic charge transfer on equal footing, and are thus well-suited for these types of investigations.

Although electron polarons are stable in α-S, hole polarons are not. Instead, hole transport is expected to follow a band-like mechanism, as suggested by experiments. Furthermore, our calculations identify S_9 and S_7 rings as the defects that respectively trap holes and electrons in α-S, thus resolving a long-standing question regarding the nature of charge traps in this system.

In Li_2S, the highest-concentration carriers are ionic species, negative Li vacancies and positive Li interstitials. Of these, only vacancies have sufficient mobility to transit Li_2S films with thicknesses consistent with the JCESR S loading target. Regarding electronic carriers in Li_2S, hole polarons are predicted to form, and to be more stable and mobile than electron polarons. Their transport can be categorized as adiabatic, and their mobilities are more than two orders of magnitude larger than for vacancy migration.

Chapter 6 Charge Transfer Stability Between Sulfide Solid Electrolytes and Li Metal Anodes: Band Edge Considerations

6.1 Introduction

The study described in this chapter aims to understand interfacial charge transfer stability between sulfide SEs (SSE) and Li metal anodes. This is accomplished by predicting the absolute positions of the band edges of the SSEs and electrode using state-of-art first-principles calculations. Bandgaps and absolute band edge positions of various SEs were evaluated using many-body perturbations theory as implemented in VASP.[154, 156, 235] Band edge positions were compared to the Li/Li^+ electrochemical potential of Li metal anode to evaluate whether the reduction of SSEs is favored or not.[109, 236]

Our calculations reveal that the bandgaps of examined SSEs are larger than 4 eV, but the positions of their CBM imply that electron injection into SSEs is thermodynamically preferred. The one exception to this trend is the B containing SSEs, Li_3BS_3. More specifically, $Li_{10}GeP_2S_{12}$ (LGPS)-family SSEs ($Li_{10}GeP_2S_{12}$, $Li_{10}SnP_2S_{12}$, and $Li_{10}SiP_2S_{12}$) tend to be less stable than the LMS (M=Ge, P, Sn, B) types. Although the position of the CBM is somewhat sensitive to the surface chemical termination and hkl facet of the SSE, varying these features appears to be insufficient to prevent reduction by Li. (In the case of Li_3BS_3 charge injection depends on the surface facet; the (001) termination is predicted to be susceptible to charge injection. while (010) is not.)

The calculated charge transfer stability is compared to trends in chemical decomposition stability, the latter property calculated the using the *pymatgen* code.[237-238] We find that all the sulfide SEs are unstable to chemical decomposition when in contact with a Li metal anode. Consistent with its more stable behavior with respect to reduction, Li_3BS_3 also shows the lowest reduction potential for chemical stability. Finally, we discuss charge transfer stability in the context of intentional interfacial coatings placed between the Li anode and the SE. In this regard $Li/LiH_2PO_4/LGPS$[239] is examined, and it is shown that an LiH_2PO_4 interlayer effectively blocks charge injection to the SE. The superb interfacial stability in this system can be attributed to the presence of this barrier layer.

6.2 Method

Bandgaps and the absolute positions of the conduction and valence band edges of 10 model SSEs (LGPS, $Li_{10}SnP_2S_{12}$, $Li_{10}SiP_2S_{12}$, β- and γ- Li_3PS_4, Li_4GeS_4, Li_4SnS_4, Li_3BS_3, $Li_2B_2S_5$, and Li_2S) are evaluated using DFT[118] and quasi particle methods[154, 156, 239] as implemented in VASP.[161-162] The semilocal PBE[136] GGA or the HSE06[148-149] hybrid functional were used to predict the structural properties and wavefunctions. The planewave cut-off energy was set to 300 eV for LGPS, $Li_{10}SnP_2S_{12}$, $Li_{10}SiP_2S_{12}$, β- and γ-Li_3PS_4, Li_4GeS_4, and Li_4SnS_4, to 350 eV for Li_3BS_3 and $Li_2B_2S_5$, and to 450 eV Li_2S. Γ-centered *k*-point sampling method was used in combination with k-point grid densities of 2×2×1 (for LGPS, $Li_{10}SnP_2S_{12}$, $Li_{10}SiP_2S_{12}$, Li_4GeS_4, and Li_4SnS_4), 2×2×2 (for γ-Li_3PS_4, Li_3BS_3, and $Li_2B_2S_5$), 3×3×3 (β-Li_3PS_4), and 4×4×4 (for Li_2S).

LGPS contains partial Li occupancies; supercell models taking the partial occupancy into account were constructed using *pymatgen*.[237-238] Following this procedure 500 structures candidates for LGPS were generated consistent with the prescribed stoichiometry. The internal degrees of freedom for these structures were relaxed to a force tolerance of 0.01 eV/Å. The most stable structure (having lowest total energy) was identified. An additional bulk structure with Li occupancies chosen to allow for a compositionally-symmetric vacuum slab was also examined. Once the structure of LGPS was determined, the structures of $Li_{10}MP_2S_{12}$ (M=Sn, Si) were generarted by substituting Ge in LGPS with Sn or Si. [112] The equilibrium cell volumes of the SEs were determined by fitting the volume-energy data to the Murnaghan equation of state,[166] while relaxing the atom positions to a force tolerance of 0.01 eV/Å.

The qusi-particle GW method[154, 156, 235] was used to predict accurate bandgaps. Among the several flavors of the GW methods, we adopted the GW_0 variant which only updates the eigenvalues in the Green's function.[158] Importantly, the combination PBE+GW_0, which takes the input wavefunctions for the GW_0 calculation from a prior, converged PBE calculation, is known to accurately reproduce experimental band offsets.[240-241] In order to calculate the band edge positions accurately, a large number of empty band were used:[159] 4400 (for LGPS, $Li_{10}SnP_2S_{12}$, $Li_{10}SiP_2S_{12}$), 4200 (Li_3BS_3, $Li_2B_2S_5$), 4000 (β-Li_3PS_4), 3360 (γ-Li_3PS_4, Li_4GeS_4, Li_4SnS_4), and 528 (Li_2S). These values were determined by running a series of PBE+G_0W_0 calculations and incrementally increasing the number of bands until the band gap and band edges were converged to within 0.02-0.03 meV/band. The number of frequency points was set to 50 by the same convergence criterion (0.02-0.03 meV/frequency point).

The identification of low energy surfaces of the sulfide SE is required for establishing band edge alignments. The surface energies considered include: LGPS ([010], [110]), $Li_{10}SnP_2S_{12}$ ([010], [110]), $Li_{10}SiP_2S_{12}$ ([010], [110]), β- Li_3PS_4 ([100], [010], [001]), γ-Li_3PS_4 ([100], [010]), Li_4GeS_4 ([100], [010]), Li_4SnS_4 ([100], [010]), $Li_2B_2S_5$ ([100], [001], [110]), Li_3BS_3 ([001], [010],[100]) and Li_2S ([111]). The low energy surface of Li_2S was adopted from our previous work.[93] The surface energies were calculated as a function of the Li chemical potential. The chemical potential of Li (μ_{Li}) in a SSE in contact with Li metal is assumed to be set by the energy per atom in bulk BCC Li (μ_{Li}(BCC Li)) (i.e., equilibrium with Li metal is assumed), while μ_{Li} at the cathode is given by $\mu_{Li}(Li) = \mu_{Li}(BCC\ Li) - eE$, where E is the cell voltage.[242] The surface energies of SSE (γ_{SSE}) are given by

$$\gamma_{SSE}(\mu_{Li}) = E_{slab} - n_{Li}\mu_{Li} - \sum_i n_i\mu_i \qquad (6.1)$$

where, E_{slab} is the total energy surface slab; n_i is the number of atoms of type i in the slab (excluding Li); and μ_i is their corresponding chemical potential. The chemical potentials of elements that comprise SSEs are evaluated with an assumption that each SSE are equilibrium with their decomposed phases. Due to their structural similarity, the surfaces of $Li_{10}SnP_2S_{12}$ and $Li_{10}SiP_2S_{12}$ adopted the same structures as for the low energy surfaces of LGPS.

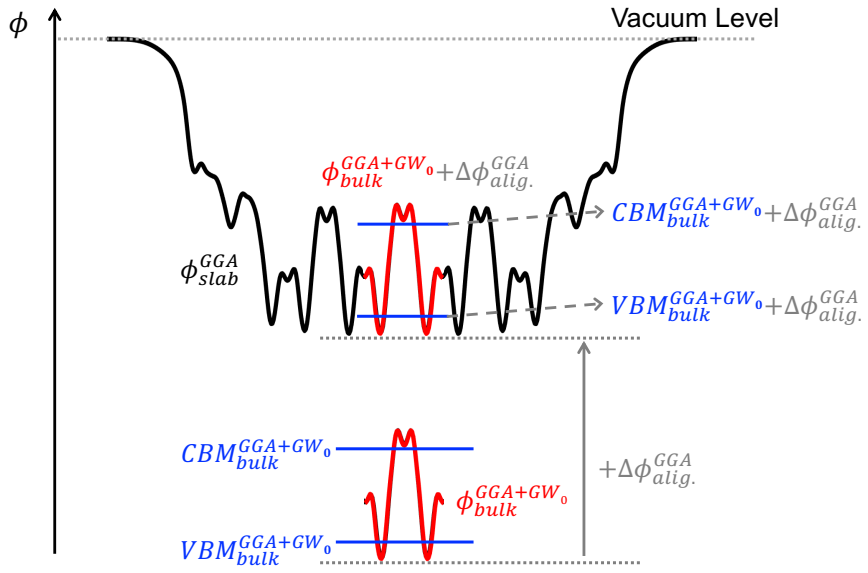

Figure 6.1 Schematic of the band edge alignment procedure. The ordinate represents the energy level of electron (ϕ) and the horizontal dotted grey line at the top is the electrostatic energy level in vacuum. Black and red corrugations represent planar-averaged electrostatic potentials of the surface slab and of the bulk, respectively. By matching the red and black corrugations, we can estimate the alignment energy ($\Delta\phi_{alig.}^{GGA}$) which allows to calculate the electron energy with respect to the vacuum level. The sold blue lines represent the band edges of SSEs and we can obtain their positions with respect to the vacuum level by adding the alignment energy to the bulk band edge positions.

The position of the band edges with respect to the vacuum level can be determined using a surface slab supercell containing a vacuum region. Figure 6.1 illustrates the band edge alignment procedure using a surface slab and a separate bulk calculation. Here, the planar-averaged electrostatic potential, ϕ_{slab}^{GGA}, of SSE slab was calculated. The electrostatic potential within the central region of the slab (assuming the slab is of sufficient thickness) will be identical to that in the bulk region of the same SSE, $\phi_{bulk}^{GGA+GW_0}$. Because orbitals of the GW_0 calculations were fixed to the ground state GGA calculation, the electrostatic calculation of bulk from GW_0 method is compatible with that of the slab model obtained by GGA. So, one can obtain the energy difference between the vacuum level and the VBM via electrostatic potential alignment between the bulk region inside of the slab surface and the bulk. The electrostatic potential alignment energy, $\Delta\phi_{alig.}^{GGA}$, is added to the bulk CBM and VBM level calculated by GGA+GW_0 in order to find the absolute positions of the band edges with respect to the vacuum level. Here, the CBM ($CBM_{bulk}^{GGW+GW_0}|_{wrt\ VAC}$) and VBM ($VBM_{bulk}^{GGW+GW_0}|_{wrt\ VAC}$) levels with respect to the vacuum level are given by the following equations:

$$\Delta\phi_{alig.}^{GGA} = \phi_{slab}^{GGA}|_{bulk\ region} - \phi_{bulk}^{GGA+GW_0} \tag{6.2}$$

$$VBM_{bulk}^{GGW+GW_0}|_{wrt\ VAC} = VBM_{bulk}^{GGW+GW_0} + \Delta\phi_{alig.}^{GGA} \tag{6.3}$$

$$CBM_{bulk}^{GGW+GW_0}|_{wrt\ VAC} = CBM_{bulk}^{GGW+GW_0} + \Delta\phi_{alig.}^{GGA}. \tag{6.4}$$

6.3 Results

6.3.1 Structure

Figure 6.2 shows the energy per atom of the 500 candidate structures for LGPS (blue dots). The lowest energy structure agrees with that of a recent DFT study;[243] in this structrure LiS_6 polyhedral edges are shared by different ions (Ge and P). Also, the 14 Li atoms present in the cell are located in four channels with three or four ions in each channel. Figure 6.3a illustrates the Li atom distribution in the conducting channel (taken as the z-direction) of LGPS.

Unfortunately, the presence of partial occupancies of Li in the LGPS structure results in a non-symmetric distribution of Li that complicates the construction of vacuum slabs that have identical compositions on both surfaces. Identical compositions are needed to unambiguously identify the band edge positions relative to the vacuum level. Surfaces having different compositions will result in the formation of an undesirable dipole within the simulation cell. A

structure that enables symmetric surface slabs was constructed by arranging the Li atoms within the conducting channels symmetrically with respect to (010) and (110) planes (Figure 6.3.b) The total energy of this structure is higher than the lowest one identified (out of the 500 structure candidates) only by 2meV/atom. This structures energy is identified by the red line in Figure 6.2. Given its low energy and favorable symmetry properties, this structure was used in subsequent surface calculations involving SE from the LGPS-family.

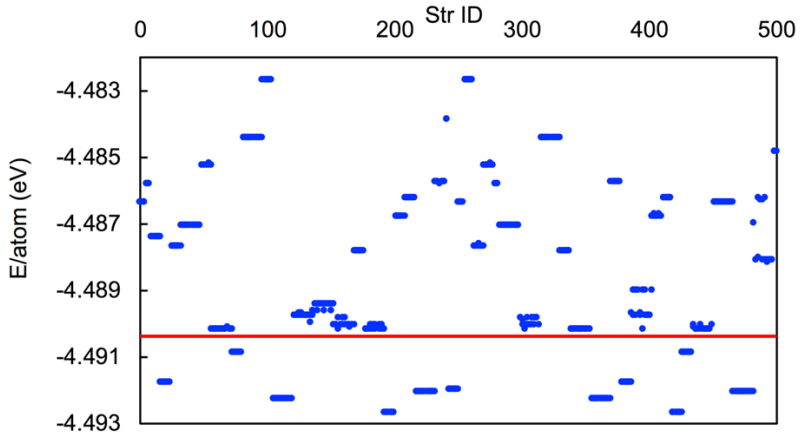

Figure 6.2 Energies of 500 candidate structures of $Li_{10}GeP_2S_{12}$ (blue dots), and the energy of a symmetrized structure that enables construction of (010) and (110) supercell slabs, each having identical surface compositions on both exposed surfaces.

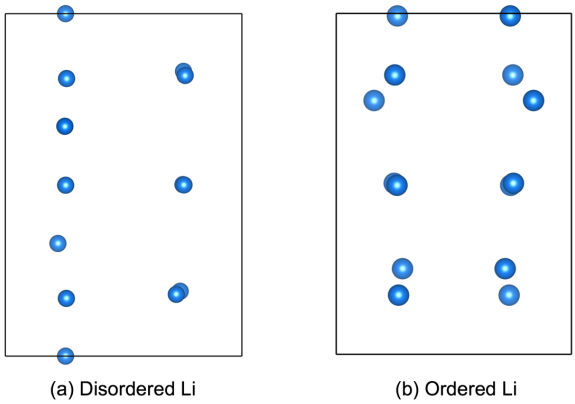

Figure 6.3 Distributions of Li atoms in the conducting channel of the lowest-energy disordered (a) and model ordered (b) LGPS structures.

6.3.1 Bandgaps

Table 6.1 summarizes bandgaps, and measured ionic conductivities of tested SSEs. The bandgaps were determined with the PBE+GW_0 approach. In comparison, the band gaps calculated with different GW methods (G_0W_0 or GW) and wavefunction inputs are presented in **Error! Reference source not found.**. As expected, larger band gaps were obtained when the input wavefunctions were generated from a HSE06 calculation; similarly, the magnitude of the bandgaps

also increased as the GW method is varied from G_0W_0 to GW_0 or GW. From these various possible calculation metnods, we adopted the PBE+GW_0 approach because it is known to accurately predict the absolute positions of band edges of semi-conductor materials.[28]

Table 6.1 Band gaps of several SSEs using the PBE wavefunction based GW_0 method. As a reference, conductivities of the SSEs are also reported.

	Energy Gap (eV)	Conductivity (S/cm)[a]
LGPS	4.09	1.2×10^{-1}
$Li_{10}SnP_2S_{12}$	4.02	4.0×10^{-2}
$Li_{10}SiP_2S_{12}$	4.28	6.4×10^{-4}
γ-Li_3PS_4	4.82	3.0×10^{-7}
β-Li_3PS_4	5.04	1.0×10^{-4}
Li_4GeS_4	4.50	7.5×10^{-4}
Li_4SnS_4	4.03	7.0×10^{-5}
Li_3BS_3	5.03	$\sim10^{-3}$ (glass)
$Li_2B_2S_5$	4.24	2.4×10^{-1} (computed)
Li_2S	5.52	

[a] Experimentally measured ionic conductivities of LGPS[ref. 244], $Li_{10}SnP_2S_{12}$[ref. 245], $Li_{10}SiP_2S_{12}$[ref. 246], β- [ref. 247] and γ- Li_3PS_4[ref. 248], Li_4GeS_4[ref.249], Li_4SnS_4[ref.250], Li_3BS_3[ref.251], and $Li_2B_2S_5$[ref.252]

The data in Tables 6.1 and 6.2 show that all of the examined SSEs exhibit large bandgaps greater than 4 eV when evaluated using the PBE+ GW_0 method. This indicates that SSEs are excellent electronic insulators with respect to thermal excitation of carriers in their intrinsic compositions.

Compounds containing BS_3 or PS_4 complex anions, such as Li_3BS_3 and β-Li_3PS_4, exhibit the largest bandgaps, typically greater than 5 eV. The polymorphs of Li_3PS_4 (β- and γ-), have similar large band gaps. $Li_2B_2S_5$, which has a similar chemical composition as Li_3BS_3 exhibits a much smaller band gap by 0.6 eV. This is because Li_3PS_4 polymorphs have the same tetrahedral PS_4 complex anion, so the band gap properties are similar. However, the anion unit in Li_3BS_3, BS_3^{3-}, is different from that in $Li_2B_2S_5$, $B_2S_5^{2-}$, and it exhibits a significant difference in its bandgap.

Another noteworthy observation is that the Sn-containing compounds, $Li_{10}SnP_2S_{12}$ and Li_4SnS_4, exhibit a very similar band gap (4.02 eV and 4.03 eV), which is the smallest among the

examined SSEs. The addition of P to Li_4SnS_4 does not change the band gap value, while the addition of P to Li_4GeS_4 decreases the band gap by nearly half an eV (4.50eV(Li_4GeS_4) → 4.09eV(LGPS)).

Table 6.2 Calculated bandgaps of SSEs using various choices for input wavefunctions (GGA vs. HSE06) and many body methods (G_0W_0, GW_0, and GW).

Name	Wavefunction calculating method	Bandgaps (eV)		
		G_0W_0	GW_0	GW
$Li_{10}GeP_2S_{12}$	GGA	3.77	4.09	4.52
	HSE	4.37	4.49	4.75
$Li_{10}SnP_2S_{12}$	GGA	3.71	4.04	4.44
	HSE	4.19	4.37	4.55
$Li_{10}SiP_2S_{12}$	GGA	3.96	4.28	-
	HSE	-	-	-
γ-Li_3PS_4	GGA	4.48	4.82	5.28
	HSE	4.96	5.14	5.37
β-Li_3PS_4	GGA	4.71	5.04	-
	HSE	-	-	-
Li_4GeS_4	GGA	4.19	4.50	-
	HSE	-	-	-
Li_4SnS_4	GGA	3.75	4.03	-
	HSE	-	-	-
$Li_2B_2S_5$	GGA	3.92	4.24	-
	HSE	-	-	-
Li_3BS_3	GGA	5.03	5.38	-
	HSE	-	-	-
Li_2S	GGA	5.18	5.52	6.03
	HSE	5.79	5.99	6.29

6.3.2 Absolute Band Edge Positions

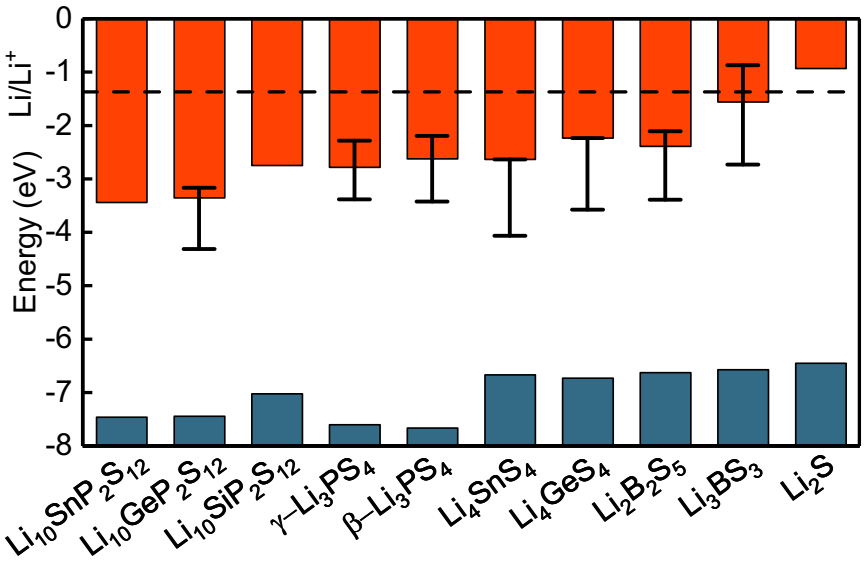

Figure 6.4 Calculated absolute band edge positions with respect to the vacuum level of several SSEs. The red and blue bars represent the conduction and valence bands, respectively. Black solid lines represent the range of CBM obtained by varying surface facets and compositions. The horizontal dashed line is the Li/Li^+ level.

Figure 6.4 illustrates the absolute band edge positions of SSEs with respect to Li/Li+. Red and blue boxes represent the conduction band and the valence band, respectively, calculated using the lowest energy surface for each compound. Although not a fast Li-ion conductor, the band edges of Li_2S are plotted for reference. The fact that the CBM lies at a higher energy than does the Li/Li+ level suggests that Li_2S will not be reduced by a Li metal anode, in agreement with experimental observations.[253]

The LGPS family SSEs, LGPS and $Li_{10}SnP_2S_{12}$, have CBMs that are much lower (by ~2.5eV) than the Li/Li+ level, indicating a strong energetic driving force for reduction of these SEs by Li., in agreement with experiments.[253] Furthermore, the CBM of LGPS and $Li_{10}SnP_2S_{12}$ are observed to be very similar regardless of surface normal ((110), (010), implying that substituting Sn for Ge does not change the electronic structure significantly. Si substitution for Ge in LGPS influences the electronic structure more than does Sn substitution: Si substitution increases the CBM position by ~1eV in both (010) and (110) facets. The CBM levels of $Li_{10}SiP_2S_{12}$ are comparable to those of the LPS polymorphs, however, the relative CBM positions with respect to the Li/Li+ level still facilitate charge injection to the SSEs.

The CBM level of LPS polymorphs are closer to Li/Li^+ level than LGPS family SSEs, but they are still lower by ~1.5eV than Li/Li^+ level. Varying the surface cleavage alters the CBM level, but

it does not affect stability trend. The CBM levels of Li_4GeS_4 and Li_4SnS_4 are comparable to that of the LPS polymorphs, even their band gaps are lower than LPS. This because CBMs of Li_4GeS_4($\Delta\phi_{alig.}^{GGA}$ = -6.7eV) and Li_4SnS_4($\Delta\phi_{alig.}^{GGA}$ = -6.9eV) are more shifted than that of LPS($\Delta\phi_{alig.}^{GGA}$ =-7.5eV) during the band edge alignment process, which compensate the lower bandgap.

The Li-B-S containing solid electrolytes (LBS) show a different band alignment trend from the previously-discussed compounds. $Li_2B_2S_5$ has a CBM level that allows for charge injection into the SE regardless of surface facets and compositions. On the other hand, the CBM level of Li_3BS_3 is very close to the Li/Li^+ level for the (100) facet, which is the lowest energy surface. It is still lower that the Li/Li^+ level, but only by 0.1eV. At the (010) facet, the trend is reversed, so the CBM level of Li_3BS_3 is higher than the Li/Li^+ by 0.52eV. The surface energy difference between (010) and (100) is only by 0.07 J/m^2 (~15%), so (010) the facet still comprises some area in the equilibrium crystallite shape. Even though both $Li_2B_2S_5$ and Li_3BS_3 contain B, their different anion configurations ($B_2S_5^{2-}$ vs. BS_3^{3-}) significantly alter their band edge positions; hence atomic structure and not chemical composition alone can affect stability. Also, a recent study claimed that $Li_2B_2S_5$ has exceptionally high ionic conductivity of ~10^{-1} S/cm based on *ab initio* molecular dynamics;[252] nudged elastic band calculations of the activation energy for Li migration in Li_3BS_3 found values less than 0.25eV.[254]

The band edge analysis suggests that Li_3BS_3 is the most stable SE with respect to charge injection amongst all of the SEs studied here. All of the other SSEs are expected to be reduced by a Li metal anode.

6.3.3 Chemically Stable Potential Range

Figure 6.5 shows the chemical stability windows of SSEs as a function of cell voltage. The SSEs do not chemically decompose at the voltage range between the top and bottom of the yellow box. Stable windows of some of the SSEs ($Li_{10}SnP_2S_{12}$, LGPS, $Li_{10}SiP_2S_{12}$, Li_3PS_4 polymorphs, Li_4GeS_4, and Li_2S) examined here have been reported elsewhere[255] and they are very similar to our results. However, stable windows of the B containing SEs and Li_4SnS_4 have not been reported to our knowledge. In particular, Li_4SnS_4 does not exist in *materials project* data base, so the DFT energy of Li_4SnS_4 was calculated with the same pseudopotential, plane wave energy cut-off, and

k-point scheme as used in the in *materials projects* and incorporated via *pymatgen* to determine the potential window.

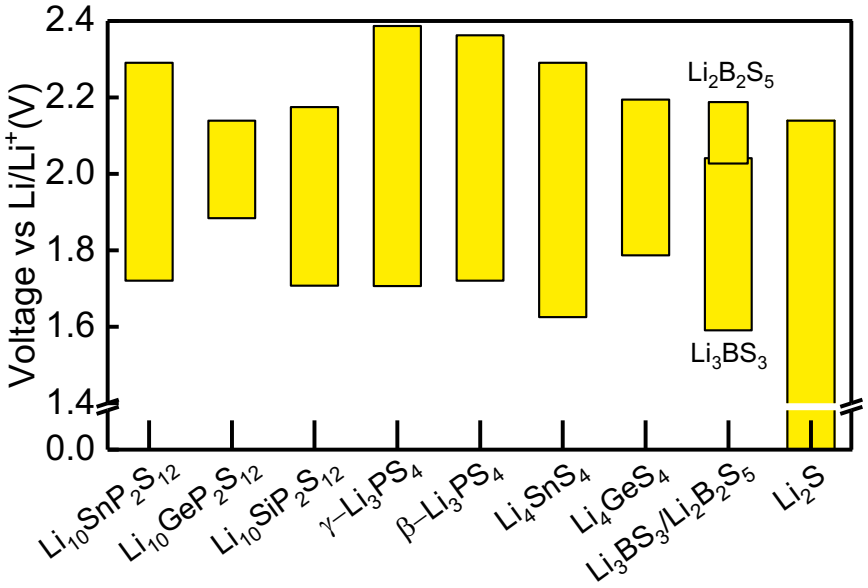

Figure 6.5 The chemical stability windows of SSEs as a function of cell voltage.

The chemical decomposition of SSEs is favored at 0V vs. Li/Li+ for all cases except Li_2S. This behavior is similar to what was predicted for charge transfer stability in Fig. 6.4. Other than Li_2S, Li_3BS_3 has the next-lowest voltage at which chemical stability is maintained. Conversely, the upper limit of its stability (2.04V) is the smallest amongst the materials examined. At this potentials Li_3BS_3 transforms into $Li_2B_2S_5$, a compounds which has also been reported to be a fast Li ion conductor.[252] This phase transformation may partially compensate for the lower stability Li_3BS_3 to some extent.

6.4 Discussion

The preceding band edge analysis was also applied to test coating materials that can potentially stabilize the interface between Li metal and sulfide SEs. We examine the coating material, $Li_2H_2PO_4$ (LHPO), exhibits a stable interface between Li and LGPS, as shown experimentally.[239]

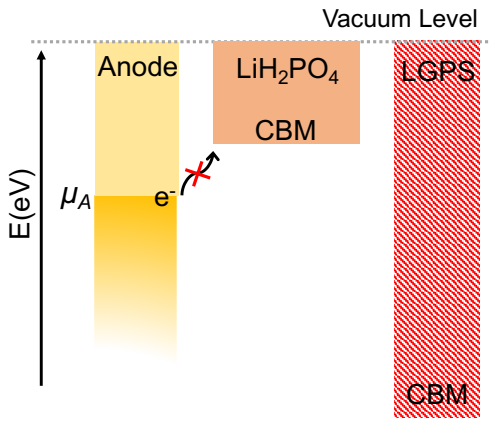

Figure 6.6 The positions of the Li/Li^+ (μ_A) and; the CBM levels of LHPO, and LGPS.

Figure 6.6 illustrates the absolute positions of the Li/Li^+, and the CBMs of LHPO and LGPS. The CBM level of LHPO was calculated using the same computational approach are used for the SEs calculations. The experiments do not observe decomposition of LHPO when it directly contacts Li metal.[239] However, the Li grand potential phase diagram approach used in the *materials project* predicts that LHPO should decompose itto Li_2O, Li_3P, and LiH.

Our band edge calculation is in accordance with the experimental observation that Li/LHPO/LGPS forms a stable interface.[239] Our calculations predict that the Li/Li^+ level is lower than the CBM of LHPO by 0.84 eV. Thus, reduction of LHPO by Li is energetically unfavorable. Furthermore, the CBM of LHPO is higher than that of LGPS by 0.84 eV, so the reduction of LGPS by LHPO is also unlikely.

Based on this analysis, it is desirable to consider both chemical stability and band alignment effects when seeking to achieve stable interfaces. An artificial SEI layer whose role is to block electron transfer from Li metal should have a CBM level that is higher than the Li/Li^+ level.

6.5 Conclusion

The stability between a Li metal anode and various sulfide SEs was evaluated by calculating and comparing their band edge positions. The absolute positions of band edges were predicted by combining quasi-particle GW methods and DFT calculations. The calculations reveal that the band gaps of SSEs are large (> 4eV), but their relative CBM positions are lower than the Li/Li^+ level, which implies that a driving force for the reduction of SEs by Li metal exists. Although, the CBM positions are sensitive to the selection of surface facets and compositions, most SSEs have CBM levels lower than the Li/Li^+ level, with the possible exception of Li_3BS_3. Li_3BS_3 a CBM that is

higher than the Li/Li^+ level by 0.52 eV for the (010) facet; this implies that charge injection from Li metal to this SE should be energetically unfavorable.

We also explored the chemical stability of the tested SSEs. Here we find that Li_3BS_3 has the lowest decomposition potential of the examined sulfide SEs. Finally, we demonstrate how band edge analysis can be used to clarify the role of artificial SEI layers that have been reported to stabilize the interface between Li and sulfide SEs. The case of an LHPO interlayer (between Li and LGPS) was considered. According the Li grand potential phase diagram, LHPO should decompose when contact with Li metal. However, experimentally, no such decomposition was observed, and the Li/LHPO/LGPS system appears to form a stable interface. We argue that the stability of the interface could be attributed to favorable band edge alignment: the CBM of LHPO is predicted to be 0.84 eV higher in energy than that of Li/Li+, suggesting limited driving force for electron transfer from Li to the interlayer. Thus, LHPO is expected to block charge injection to SEs. This design rule – identifying for compounds with high absolute CMB levels – can be used for the selection of artificial SEIs that can prevent charge injection into SEs.

Chapter 7 Conclusions and Next Steps

The increasing demand for EVs has created a need for electrical energy storage systems with high capacity and low cost. The Li-S chemistry is one promising candidate. However, the commercialization of this battery chemistry is impeded by several challenges, namely, lack of understanding of the basic properties of its redox-end members (S and Li_2S), the absence of effective strategies for regulating polysulfide dissolution, the insulating nature of S_8 and Li_2S, and the implementation of a Li metal anode. This dissertation has examined these challenges using atomistic modeling. The goal is to gain knowledge that can be useful for the development of design strategies that could accelerate the commercialization of Li-S batteries.

The calculations presented in Chapter 3 on the thermodynamic, electronic, and surface properties of redox-end members improve our understanding of the phases present during the operation of Li-S batteries. Free energy calculations on allotropes of S confirm that α-S is the stable phase at low temperature. However, since the energy difference between α- and β-, the latter being a higher temperature phase, is very small (< 1meV/atom), which phase is present does not significantly impact the redox potential. Similarly, the electronic structure was found to be insensitive to the phase of S that is present in the cathode. These observations imply that the enhanced performance observed from β-S-based cells in experiments[19] is unlikely to have a thermodynamic origin; rather, kinetic differences between these phases might be responsible.

Calculations on Li_2S_2 reveal that this phase is metastable and prefers to decompose into a mixture of Li_2S and S_8. A recent experiment observed Li_2S_2 during Li-S battery cycling by x-ray diffraction: the persulfide phase was reported to be present in the first and second cycles, but disappeared in subsequent cycles.[256] Regarding surface properties, the equilibrium crystalites of Li_2S are comprised entirely of stoichiometric (111) facets, while α-S crystallites are a mixture of (001), (010), (100), (011), (110), and (111) facets. This surface data provides a reference to experiments and the simulations regarding surface phenomena.

It is well known that Li-S cells undergo capacity fade during cycling due to the dissolution of polysulfide species. In Chapter 4 we have described an ‘additive approach’ to preventing the

dissolution of PS by combining encapsulation and adsorption of PS in MOFs.[257] In this approach the MOF would serve as a cathode support material. The MOF's affinity for PS can be tuned and maximized via metal substitution on the coordinatively unsaturated sites (CUS) in a MOF. We screened 16 metal-substituted variants of the open-metal-site MOF M_2(dobdc) for their ability to anchor model PS species (S_8, Li_2S_4, and Li_2S) present during Li-S cycling. Our study identified metal-substituted M_2(dobdc) compositions that exhibit large exothermic energies for PS adsorption. The trend in adsorption energies were correlated with the charge transfer between the MOF and the PS. Considering cost and ease of synthesis, Ni_2(dobdc) was proposed as the most promising cathode support.

The insulating nature of the charge and discharge products of Li-S batteries requires sufficient charge transport within the cathode; otherwise these cells will exhibit limited capacity or undergo sudden death. Most MOFs are electrical insulators, which implies that conducting additives will be needed in a MOF-supported Li-S cathode. However, some MOFs have been reported to exhibit a moderate conductivity.[195] For example, a recent DFT study confirmed that Cu-BHT is electrically conducting and also shows high affinity for PS species.[258] So, the application of electrically conducting porous MOFs as a cathode support can concurrently address slow transport and PS dissolution issues. Opportunities exist for further computational studies aimed at improving the electrical conductivity of MOFs. Furthermore, a large number ~10^5 of real and hypothetical MOFs[79] have been reported/proposed. Through high throughput computing, it may be possible to pinpoint the optimal MOFs having pore sizes that that allow the passage of/access to the electrolyte, yet blocks PS diffusion.

In Chapter 5 we explored the charge transport mechanisms in S_8 and Li_2S. Achieving sufficient charge transfer rates in the cathode of a Li-S cell is a critical factor for enhancing performance. Both adiabatic and non-adiabatic transport mechanisms were considered . In both S_8 and Li_2S, the predicted equilibrium defect concentrations were extremely small, so the corresponding conductivities are expected to be negligible, especially in S_8. Delocalized (S_8) and localized (Li_2S) holes are predicted to be the main electronic charge carriers. The mobilities of these species were predicted to be high enough to satisfy sulfur loading targets of 6 mg/cm^2. What is needed is a strategy to increase the concentrations of these carriers. Concentrations can in principle be increased by introducing dopants. Computational screening of dopants for their degree of increase in hole concentration will be helpful. However, the redox participation of dopants could detrimentally affect the electrochemical performance, so the redox stability of dopant should be

addressed. Recent experiments in which the sulfur cathode was doped with Te yielded high energy density and Coulombic efficiency.[259] The superior performance was argued to arise from the Te inclusions' increasing the mobility of the Li defects and the lithiation/delithiation kinetics which contribute to higher conductivities.

Nonadiabatic charge transport dominates for larger hopping distances (*e.g.* between S_8 rings, where the distance is ~3.4 Å). Long distance polaron hopping is also observed in battery discharge products such as lithium/sodium peroxide/superoxide in metal-air batteries or lithium persulfide in Li-S batteries However, current literature reports generally examine polaron hopping only in the adiabatic regime.[99, 150, 152] So, revisiting the charge transport properties of those materials in the nonadiabatic regime may result in more accurate predictions of conductivities associated with these hopping mechanisms.

Finally, the charge transfer stability between sulfide SEs and the Li metal anode was examined in Chapter 6. Reduction or oxidation of SEs by the electrodes is undesirable because these processes can inject electrons or holes into the SE. These carriers can subsequently allow for the self-discharge or short-circuiting of the cell. The likelihood for charge injection was determined by comparing the position of the conduction band minimum in SEs to the Li/Li+ level of a Li anode. We predicted the CBM position for several model sulfide SEs; all compounds examined were found to be susceptible to electron injection by Li metal. Among the tested SEs, Li_3BS_3 has a CBM that is closest to the Li/Li+ level, implying that it is the 'least unstable' of the systems examined. The band edge positions are found to be sensitive to the choice of surface facet and surface composition. For most SSEs, altering these features was insufficient to prevent charge injection, the one exception being Li_3BS_3. The CBM level of Li_3BS_3 determined for the (100) facet is predicted to be higher than the Li/Li^+ level, so steering the surface structure of Li_3BS_3 towards exhibiting (100) facets could possibly stabilize this interface.

A chemical interfacial stability analysis was found to closely follow the trend obtained for charge transfer stability. Li_3BS_3 exhibits the lowest decomposition potential, but still decomposes when directly contact with Li metal. These results suggest that B containing sulfides are promising sulfide SEs in terms of their stability. Also, recent computational studies provide evidence for high ionic conductivities in B containing SEs such as Li_3BS_3,[254] $Li_2B_3S_5$,[252] and $Li_5B_7S_{13}$.[252] Moreover, amorphous Li_2S-B_2S_3, exhibits an ionic conductivity of 1 mS/cm experimentally.[251] Although there are several indications of high ionic conductivities in B containing sulfides, less attention has

been paid to these materials as solid electrolytes. Therefore, more effort examining B-based sulfides is called for.

Bibliography

(1) Chu, S.; Majumdar, A., Opportunities and challenges for a sustainable energy future. *Nat.* **2012,** *488*, 294.

(2) da Rosa, A. V., Chapter 1 - Generalities. In *Fundamentals of Renewable Energy Processes (Second Edition)*, da Rosa, A. V., Ed. Academic Press: Boston, 2009; pp 1-57.

(3) Stern, N. *Stern review: the economics of climate change*; United Kingdom, 2006-10-30, 2006.

(4) Spe; Wpc; Aapg; Spee; Seg; Spwla; Eage, Petroleum Resources Management System (2018 version). Society of Petroleum Engineers: 2018; pp 1-52.

(5) Ming, Y.; Purewal, J.; Yang, J.; Xu, C.; Veenstra, M.; Gaab, M.; Müller, U.; Siegel, D. J., Stability of MOF-5 in a hydrogen gas environment containing fueling station impurities. *Int. J. Hydrogen Energy* **2016,** *41* (22), 9374-9382.

(6) Cano, Z. P.; Banham, D.; Ye, S.; Hintennach, A.; Lu, J.; Fowler, M.; Chen, Z., Batteries and fuel cells for emerging electric vehicle markets. *Nat. Energy* **2018,** *3* (4), 279-289.

(7) Whittingham, M. S., Lithium Batteries and Cathode Materials. *Chem. Rev. (Washington, DC, U. S.)* **2004,** *104* (10), 4271-4302.

(8) Bruce, P. G.; Freunberger, S. A.; Hardwick, L. J.; Tarascon, J.-M., Li-O_2 and Li-S batteries with high energy storage. *Nat. Mater.* **2012,** *11* (1), 19-29.

(9) Chiang, Y.-M., Building a Better Battery. *Science* **2010,** *330* (6010), 1485-1486.

(10) Goodenough, J. B.; Park, K.-S., The Li-Ion Rechargeable Battery: A Perspective. *J. Am. Chem. Soc.* **2013,** *135* (4), 1167-1176.

(11) Kang, K.; Song, K.; Heo, H.; Yoo, S.; Kim, G.-S.; Lee, G.; Kang, Y.-M.; Jo, M.-H., Kinetics-driven high power Li-ion battery with a-Si/NiSix core-shell nanowire anodes. *Chem. Sci.* **2011,** *2* (6), 1090-1093.

(12) Kang, B.; Ceder, G., Battery materials for ultrafast charging and discharging. *Nat.* **2009,** *458* (7235), 190-193.

(13) Seh, Z. W.; Zhang, Q.; Li, W.; Zheng, G.; Yao, H.; Cui, Y., Stable cycling of lithium sulfide cathodes through strong affinity with a bifunctional binder. *Chem. Sci.* **2013,** *4* (9), 3673-3677.

(14) Cairns, E. J.; Albertus, P., Batteries for Electric and Hybrid-Electric Vehicles. *Annu. Rev. Chem. Biomol. Eng.* **2010,** *1* (1), 299-320.

(15) Li, W.; Long, R.; Chen, H.; Geng, J., A review of factors influencing consumer intentions to adopt battery electric vehicles. *Renew. Sustain. Energy Rev* **2017,** *78*, 318-328.

(16) Olivetti, E. A.; Ceder, G.; Gaustad, G. G.; Fu, X., Lithium-Ion Battery Supply Chain Considerations: Analysis of Potential Bottlenecks in Critical Metals. *Joule* **2017,** *1* (2), 229-243.

(17) Armand, M.; Tarascon, J. M., Building better batteries. *Nat.* **2008,** *451*, 652.

(18) *MINERAL COMMODITY SUMMARIES 2018*; U.S. Geological Survey: Reston, VA, 2018; pp 160-161.

(19) Moon, S.; Jung, Y. H.; Jung, W. K.; Jung, D. S.; Choi, J. W.; Kim, D. K., Encapsulated Monoclinic Sulfur for Stable Cycling of Li–S Rechargeable Batteries. *Adv. Mater.* **2013,** *25* (45), 6547-6553.

(20) Ji, X.; Lee, K. T.; Nazar, L. F., A highly ordered nanostructured carbon-sulphur cathode for lithium-sulphur batteries. *Nat. Mater.* **2009,** *8* (6), 500-506.

(21) Fu, Y.; Su, Y.-S.; Manthiram, A., Sulfur–Carbon Nanocomposite Cathodes Improved by an Amphiphilic Block Copolymer for High-Rate Lithium–Sulfur Batteries. *ACS Appl. Mater. Interfaces* **2012,** *4* (11), 6046-6052.

(22) Xin, S.; Gu, L.; Zhao, N.-H.; Yin, Y.-X.; Zhou, L.-J.; Guo, Y.-G.; Wan, L.-J., Smaller Sulfur Molecules Promise Better Lithium–Sulfur Batteries. *J. Am. Chem. Soc.* **2012,** *134* (45), 18510-18513.

(23) Yang, Y.; Zheng, G.; Cui, Y., Nanostructured sulfur cathodes. *Chem. Soc. Rev.* **2013,** *42* (7), 3018-3032.

(24) Mikhaylik, Y. V.; Akridge, J. R., Polysulfide Shuttle Study in the Li/S Battery System. *J. Electrochem. Soc.* **2004,** *151* (11), A1969-A1976.

(25) Zhang, Z.; Shao, Y.; Lotsch, B.; Hu, Y.-S.; Li, H.; Janek, J.; Nazar, L. F.; Nan, C.-W.; Maier, J.; Armand, M.; Chen, L., New horizons for inorganic solid state ion conductors. *Energy Environ. Sci.* **2018**.

(26) Villevieille, C.; Novak, P., A metastable b-sulfur phase stabilized at room temperature during cycling of high efficiency carbon fibre-sulfur composites for Li-S batteries. *J. Mater. Chem. A* **2013,** *1* (42), 13089-13092.

(27) Yamin, H.; Gorenshtein, A.; Penciner, J.; Sternberg, Y.; Peled, E., Lithium Sulfur Battery: Oxidation/Reduction Mechanisms of Polysulfides in THF Solutions. *J. Electrochem. Soc.* **1988,** *135* (5), 1045-1048.

(28) Cunningham, P. T.; Johnson, S. A.; Cairns, E. J., Phase Equilibria in Lithium-Chalcogen Systems: II . Lithium-Sulfur. *J. Electrochem. Soc.* **1972,** *119* (11), 1448-1450.

(29) Cuisinier, M.; Cabelguen, P.-E.; Evers, S.; He, G.; Kolbeck, M.; Garsuch, A.; Bolin, T.; Balasubramanian, M.; Nazar, L. F., Sulfur Speciation in Li–S Batteries Determined by Operando X-ray Absorption Spectroscopy. *J. Phys. Chem. Lett.* **2013,** *4* (19), 3227-3232.

(30) Hagen, M.; Schiffels, P.; Hammer, M.; Dörfler, S.; Tübke, J.; Hoffmann, M. J.; Althues, H.; Kaskel, S., In-Situ Raman Investigation of Polysulfide Formation in Li-S Cells. *J. Electrochem. Soc.* **2013,** *160* (8), A1205-A1214.

(31) Okamoto, H., The Li-S (lithium-sulfur) system. *J. Phase Equilib.* **1995,** *16* (1), 94-97.

(32) Radin, M. D.; Rodriguez, J. F.; Tian, F.; Siegel, D. J., Lithium Peroxide Surfaces Are Metallic, While Lithium Oxide Surfaces Are Not. *J. Am. Chem. Soc.* **2011,** *134* (2), 1093-1103.

(33) Wang, L.; Zhang, T.; Yang, S.; Cheng, F.; Liang, J.; Chen, J., A quantum-chemical study on the discharge reaction mechanism of lithium-sulfur batteries. *J. Energy Chem.* **2013,** *22* (1), 72-77.

(34) Yang, Y.; McDowell, M. T.; Jackson, A.; Cha, J. J.; Hong, S. S.; Cui, Y., New Nanostructured Li2S/Silicon Rechargeable Battery with High Specific Energy. *Nano Lett.* **2010,** *10* (4), 1486-1491.

(35) Lin, Z.; Liu, Z.; Dudney, N. J.; Liang, C., Lithium Superionic Sulfide Cathode for All-Solid Lithium–Sulfur Batteries. *ACS Nano* **2013,** *7* (3), 2829-2833.

(36) Chen, Y.-X.; Kaghazchi, P., Metalization of Li2S particle surfaces in Li-S batteries. *Nanoscale* **2014,** *6* (22), 13391-13395.

(37) Wallace, D. C., *Thermodynamics of crystals*. Wiley: 1972.

(38) Albertus, P.; Girishkumar, G.; McCloskey, B.; Sánchez-Carrera, R. S.; Kozinsky, B.; Christensen, J.; Luntz, A. C., Identifying Capacity Limitations in the Li/Oxygen Battery Using Experiments and Modeling. *J. Electrochem. Soc.* **2011,** *158* (3), A343-A351.

(39) Radin, M.; Tian, F.; Siegel, D., Electronic structure of Li_2O_2 {0001} surfaces. *J. Mater. Sci.* **2012,** *47* (21), 7564-7570.

(40) Xiao, L.; Cao, Y.; Xiao, J.; Schwenzer, B.; Engelhard, M. H.; Saraf, L. V.; Nie, Z.; Exarhos, G. J.; Liu, J., A Soft Approach to Encapsulate Sulfur: Polyaniline Nanotubes for Lithium-Sulfur Batteries with Long Cycle Life. *Adv. Mater.* **2012,** *24* (9), 1176-1181.

(41) Zheng, J.; Lv, D.; Gu, M.; Wang, C.; Zhang, J.-G.; Liu, J.; Xiao, J., How to Obtain Reproducible Results for Lithium Sulfur Batteries? *J. Electrochem. Soc.* **2013,** *160* (11), A2288-A2292.

(42) Wang, L.; Liu, J.; Yuan, S.; Wang, Y.; Xia, Y., To mitigate self-discharge of lithium-sulfur batteries by optimizing ionic liquid electrolytes. *Energy Environ. Sci.* **2016,** *9* (1), 224-231.

(43) Deng, Z.; Zhang, Z.; Lai, Y.; Liu, J.; Li, J.; Liu, Y., Electrochemical Impedance Spectroscopy Study of a Lithium/Sulfur Battery: Modeling and Analysis of Capacity Fading. *J. Electrochem. Soc.* **2013,** *160* (4), A553-A558.

(44) Zhou, W.; Wang, C.; Zhang, Q.; Abruña, H. D.; He, Y.; Wang, J.; Mao, S. X.; Xiao, X., Tailoring Pore Size of Nitrogen-Doped Hollow Carbon Nanospheres for Confining Sulfur in Lithium–Sulfur Batteries. *Adv. Energy Mater.* **2015,** *5* (16), 1401752.

(45) Zhou, G.; Zhao, Y.; Manthiram, A., Dual-Confined Flexible Sulfur Cathodes Encapsulated in Nitrogen-Doped Double-Shelled Hollow Carbon Spheres and Wrapped with Graphene for Li–S Batteries. *Adv. Energy Mater.* **2015,** *5* (9), 1402263-n/a.

(46) Zhou, G.; Paek, E.; Hwang, G. S.; Manthiram, A., Long-life Li/polysulphide batteries with high sulphur loading enabled by lightweight three-dimensional nitrogen/sulphur-codoped graphene sponge. *Nat. Commun.* **2015,** *6*, 7760.

(47) Zhang, S. S., Heteroatom-doped carbons: synthesis, chemistry and application in lithium/sulphur batteries. *Inorg. Chem. Front.* **2015,** *2* (12), 1059-1069.

(48) Song, J.; Gordin, M. L.; Xu, T.; Chen, S.; Yu, Z.; Sohn, H.; Lu, J.; Ren, Y.; Duan, Y.; Wang, D., Strong Lithium Polysulfide Chemisorption on Electroactive Sites of Nitrogen-Doped Carbon Composites For High-Performance Lithium–Sulfur Battery Cathodes. *Angew. Chem. Int. Ed.* **2015,** *54* (14), 4325-4329.

(49) Pang, Q.; Tang, J.; Huang, H.; Liang, X.; Hart, C.; Tam, K. C.; Nazar, L. F., A Nitrogen and Sulfur Dual-Doped Carbon Derived from Polyrhodanine@Cellulose for Advanced Lithium–Sulfur Batteries. *Adv. Mater.* **2015,** *27* (39), 6021-6028.

(50) Song, J.; Xu, T.; Gordin, M. L.; Zhu, P.; Lv, D.; Jiang, Y.-B.; Chen, Y.; Duan, Y.; Wang, D., Nitrogen-Doped Mesoporous Carbon Promoted Chemical Adsorption of Sulfur and Fabrication of High-Areal-Capacity Sulfur Cathode with Exceptional Cycling Stability for Lithium-Sulfur Batteries. *Adv. Funct. Mater.* **2014,** *24* (9), 1243-1250.

(51) Rong, J.; Ge, M.; Fang, X.; Zhou, C., Solution Ionic Strength Engineering As a Generic Strategy to Coat Graphene Oxide (GO) on Various Functional Particles and Its Application in High-Performance Lithium–Sulfur (Li–S) Batteries. *Nano Lett.* **2014,** *14* (2), 473-479.

(52) Qiu, Y.; Li, W.; Zhao, W.; Li, G.; Hou, Y.; Liu, M.; Zhou, L.; Ye, F.; Li, H.; Wei, Z.; Yang, S.; Duan, W.; Ye, Y.; Guo, J.; Zhang, Y., High-Rate, Ultralong Cycle-Life Lithium/Sulfur Batteries Enabled by Nitrogen-Doped Graphene. *Nano Lett.* **2014,** *14* (8), 4821-4827.

(53) He, G.; Hart, C. J.; Liang, X.; Garsuch, A.; Nazar, L. F., Stable Cycling of a Scalable Graphene-Encapsulated Nanocomposite for Lithium–Sulfur Batteries. *ACS Appl. Mater. Interfaces* **2014,** *6* (14), 10917-10923.

(54) Song, M.-K.; Zhang, Y.; Cairns, E. J., A Long-Life, High-Rate Lithium/Sulfur Cell: A Multifaceted Approach to Enhancing Cell Performance. *Nano Lett.* **2013,** *13* (12), 5891-5899.

(55) Zhang, L.; Ji, L.; Glans, P.-A.; Zhang, Y.; Zhu, J.; Guo, J., Electronic structure and chemical bonding of a graphene oxide-sulfur nanocomposite for use in superior performance lithium-sulfur cells. *Phys. Chem. Chem. Phys.* **2012,** *14* (39), 13670-13675.

(56) Wang, H.; Yang, Y.; Liang, Y.; Robinson, J. T.; Li, Y.; Jackson, A.; Cui, Y.; Dai, H., Graphene-Wrapped Sulfur Particles as a Rechargeable Lithium–Sulfur Battery Cathode Material with High Capacity and Cycling Stability. *Nano Lett.* **2011,** *11* (7), 2644-2647.

(57) Ji, L.; Rao, M.; Zheng, H.; Zhang, L.; Li, Y.; Duan, W.; Guo, J.; Cairns, E. J.; Zhang, Y., Graphene Oxide as a Sulfur Immobilizer in High Performance Lithium/Sulfur Cells. *J. Am. Chem. Soc.* **2011,** *133* (46), 18522-18525.

(58) Strubel, P.; Thieme, S.; Biemelt, T.; Helmer, A.; Oschatz, M.; Brückner, J.; Althues, H.; Kaskel, S., ZnO Hard Templating for Synthesis of Hierarchical Porous Carbons with Tailored Porosity and High Performance in Lithium-Sulfur Battery. *Adv. Funct. Mater.* **2015,** *25* (2), 287-297.

(59) Li, Z.; Jiang, Y.; Yuan, L.; Yi, Z.; Wu, C.; Liu, Y.; Strasser, P.; Huang, Y., A Highly Ordered Meso@Microporous Carbon-Supported Sulfur@Smaller Sulfur Core–Shell Structured Cathode for Li–S Batteries. *ACS Nano* **2014,** *8* (9), 9295-9303.

(60) He, G.; Evers, S.; Liang, X.; Cuisinier, M.; Garsuch, A.; Nazar, L. F., Tailoring Porosity in Carbon Nanospheres for Lithium–Sulfur Battery Cathodes. *ACS Nano* **2013,** *7* (12), 10920-10930.

(61) Jayaprakash, N.; Shen, J.; Moganty, S. S.; Corona, A.; Archer, L. A., Porous Hollow Carbon@Sulfur Composites for High-Power Lithium–Sulfur Batteries. *Angew. Chem.* **2011,** *123* (26), 6026-6030.

(62) Pang, Q.; Liang, X.; Kwok, C. Y.; Nazar, L. F., Advances in lithium–sulfur batteries based on multifunctional cathodes and electrolytes. *Nat. Energy* **2016,** *1*, 16132.

(63) Hart, C. J.; Cuisinier, M.; Liang, X.; Kundu, D.; Garsuch, A.; Nazar, L. F., Rational design of sulphur host materials for Li-S batteries: correlating lithium polysulphide adsorptivity and self-discharge capacity loss. *Chem. Commun. (Cambridge, U. K.)* **2015,** *51* (12), 2308-2311.

(64) Ji, X.; Evers, S.; Black, R.; Nazar, L. F., Stabilizing lithium–sulphur cathodes using polysulphide reservoirs. *Nat. Commun.* **2011,** *2*, 325.

(65) Evers, S.; Yim, T.; Nazar, L. F., Understanding the Nature of Absorption/Adsorption in Nanoporous Polysulfide Sorbents for the Li–S Battery. *J. Phys. Chem. C* **2012,** *116* (37), 19653-19658.

(66) Seh, Z. W.; Li, W.; Cha, J. J.; Zheng, G.; Yang, Y.; McDowell, M. T.; Hsu, P.-C.; Cui, Y., Sulphur–TiO_2 yolk–shell nanoarchitecture with internal void space for long-cycle lithium–sulphur batteries. *Nat. Commun.* **2013,** *4*, 1331.

(67) Seh, Z. W.; Yu, J. H.; Li, W.; Hsu, P.-C.; Wang, H.; Sun, Y.; Yao, H.; Zhang, Q.; Cui, Y., Two-dimensional layered transition metal disulphides for effective encapsulation of high-capacity lithium sulphide cathodes. *Nat. Commun.* **2014,** *5*, 5017.

(68) Zhang, Q.; Wang, Y.; Seh, Z. W.; Fu, Z.; Zhang, R.; Cui, Y., Understanding the Anchoring Effect of Two-Dimensional Layered Materials for Lithium–Sulfur Batteries. *Nano Lett.* **2015,** *15* (6), 3780-3786.

(69) Kim, H.; Lee, J. T.; Lee, D.-C.; Magasinski, A.; Cho, W.-i.; Yushin, G., Plasma-Enhanced Atomic Layer Deposition of Ultrathin Oxide Coatings for Stabilized Lithium–Sulfur Batteries. *Adv. Energy Mater.* **2013,** *3* (10), 1308-1315.

(70) Tao, X.; Wang, J.; Ying, Z.; Cai, Q.; Zheng, G.; Gan, Y.; Huang, H.; Xia, Y.; Liang, C.; Zhang, W.; Cui, Y., Strong Sulfur Binding with Conducting Magnéli-Phase TinO2n–1 Nanomaterials for Improving Lithium–Sulfur Batteries. *Nano Lett.* **2014,** *14* (9), 5288-5294.

(71) Yao, H.; Zheng, G.; Hsu, P.-C.; Kong, D.; Cha, J. J.; Li, W.; Seh, Z. W.; McDowell, M. T.; Yan, K.; Liang, Z.; Narasimhan, V. K.; Cui, Y., Improving lithium–sulphur batteries through spatial control of sulphur species deposition on a hybrid electrode surface. *Nat. Commun.* **2014,** *5*, 3943.

(72) Jiang, J.; Zhu, J.; Ai, W.; Wang, X.; Wang, Y.; Zou, C.; Huang, W.; Yu, T., Encapsulation of sulfur with thin-layered nickel-based hydroxides for long-cyclic lithium–sulfur cells. *Nat. Commun.* **2015,** *6*, 8622.

(73) Xiao, Z.; Yang, Z.; Wang, L.; Nie, H.; Zhong, M. e.; Lai, Q.; Xu, X.; Zhang, L.; Huang, S., A Lightweight TiO2/Graphene Interlayer, Applied as a Highly Effective Polysulfide Absorbent for Fast, Long-Life Lithium–Sulfur Batteries. *Adv. Mater.* **2015,** *27* (18), 2891-2898.

(74) Koh, H. S.; Rana, M. K.; Hwang, J.; Siegel, D. J., Thermodynamic screening of metal-substituted MOFs for carbon capture. *Phys. Chem. Chem. Phys.* **2013,** *15* (13), 4573-4581.

(75) Bae, Y.-S.; Liu, J.; Wilmer, C. E.; Sun, H.; Dickey, A. N.; Kim, M. B.; Benin, A. I.; Willis, R. R.; Barpaga, D.; LeVan, M. D.; Snurr, R. Q., The effect of pyridine modification of Ni-DOBDC on CO_2 capture under humid conditions. *Chem. Commun. (Cambridge, U. K.)* **2014,** *50* (25), 3296-3298.

(76) Rana, M. K.; Koh, H. S.; Hwang, J.; Siegel, D. J., Comparing van der Waals Density Functionals for CO_2 Adsorption in Metal Organic Frameworks. *J. Phys. Chem. C* **2012,** *116* (32), 16957-16968.

(77) Peng, Y.; Krungleviciute, V.; Eryazici, I.; Hupp, J. T.; Farha, O. K.; Yildirim, T., Methane Storage in Metal–Organic Frameworks: Current Records, Surprise Findings, and Challenges. *J. Am. Chem. Soc.* **2013,** *135* (32), 11887-11894.

(78) Koh, H. S.; Rana, M. K.; Wong-Foy, A. G.; Siegel, D. J., Predicting Methane Storage in Open-Metal-Site Metal–Organic Frameworks. *J. Phys. Chem. C* **2015,** *119* (24), 13451-13458.

(79) Goldsmith, J.; Wong-Foy, A. G.; Cafarella, M. J.; Siegel, D. J., Theoretical Limits of Hydrogen Storage in Metal–Organic Frameworks: Opportunities and Trade-Offs. *Chem. Mater.* **2013,** *25* (16), 3373-3382.

(80) Purewal, J.; Liu, D.; Sudik, A.; Veenstra, M.; Yang, J.; Maurer, S.; Müller, U.; Siegel, D. J., Improved Hydrogen Storage and Thermal Conductivity in High-Density MOF-5 Composites. *J. Phys. Chem. C* **2012,** *116* (38), 20199-20212.

(81) Caskey, S. R.; Wong-Foy, A. G.; Matzger, A. J., Dramatic Tuning of Carbon Dioxide Uptake via Metal Substitution in a Coordination Polymer with Cylindrical Pores. *J. Am. Chem. Soc.* **2008,** *130* (33), 10870-10871.

(82) Kapelewski, M. T.; Geier, S. J.; Hudson, M. R.; Stück, D.; Mason, J. A.; Nelson, J. N.; Xiao, D. J.; Hulvey, Z.; Gilmour, E.; FitzGerald, S. A.; Head-Gordon, M.; Brown, C. M.; Long, J. R., M_2(m-dobdc) (M = Mg, Mn, Fe, Co, Ni) Metal–Organic Frameworks Exhibiting Increased Charge Density and Enhanced H_2 Binding at the Open Metal Sites. *J. Am. Chem. Soc.* **2014,** *136* (34), 12119-12129.

(83) Demir-Cakan, R.; Morcrette, M.; Nouar, F.; Davoisne, C.; Devic, T.; Gonbeau, D.; Dominko, R.; Serre, C.; Férey, G.; Tarascon, J.-M., Cathode Composites for Li–S Batteries via the Use of Oxygenated Porous Architectures. *J. Am. Chem. Soc.* **2011,** *133* (40), 16154-16160.

(84) Zhou, J.; Li, R.; Fan, X.; Chen, Y.; Han, R.; Li, W.; Zheng, J.; Wang, B.; Li, X., Rational design of a metal-organic framework host for sulfur storage in fast, long-cycle Li-S batteries. *Energy Environ. Sci.* **2014,** *7* (8), 2715-2724.

(85) Wang, Z.; Li, X.; Cui, Y.; Yang, Y.; Pan, H.; Wang, Z.; Wu, C.; Chen, B.; Qian, G., A Metal–Organic Framework with Open Metal Sites for Enhanced Confinement of Sulfur and Lithium–Sulfur Battery of Long Cycling Life. *Cryst. Growth Des.* **2013,** *13* (11), 5116-5120.

(86) Wang, Z.; Wang, B.; Yang, Y.; Cui, Y.; Wang, Z.; Chen, B.; Qian, G., Mixed-Metal–Organic Framework with Effective Lewis Acidic Sites for Sulfur Confinement in High-Performance Lithium–Sulfur Batteries. *ACS Appl. Mater. Interfaces* **2015,** *7* (37), 20999-21004.

(87) Zheng, J.; Tian, J.; Wu, D.; Gu, M.; Xu, W.; Wang, C.; Gao, F.; Engelhard, M. H.; Zhang, J.-G.; Liu, J.; Xiao, J., Lewis Acid–Base Interactions between Polysulfides and Metal Organic Framework in Lithium Sulfur Batteries. *Nano Lett.* **2014,** *14* (5), 2345-2352.

(88) Wiers, B. M.; Foo, M.-L.; Balsara, N. P.; Long, J. R., A Solid Lithium Electrolyte via Addition of Lithium Isopropoxide to a Metal–Organic Framework with Open Metal Sites. *J. Am. Chem. Soc.* **2011,** *133* (37), 14522-14525.

(89) Bai, S.; Liu, X.; Zhu, K.; Wu, S.; Zhou, H., Metal–organic framework-based separator for lithium–sulfur batteries. *Nat. Energy* **2016,** *1*, 16094.

(90) Helen, M.; Reddy, M. A.; Diemant, T.; Golla-Schindler, U.; Behm, R. J.; Kaiser, U.; Fichtner, M., Single step transformation of sulphur to Li2S2/Li2S in Li-S batteries. *Sci. Rep.* **2015,** *5*, 12146.

(91) Cheng, L.; Curtiss, L. A.; Zavadil, K. R.; Gewirth, A. A.; Shao, Y.; Gallagher, K. G., Sparingly Solvating Electrolytes for High Energy Density Lithium–Sulfur Batteries. *ACS Energy Lett.* **2016,** *1* (3), 503-509.

(92) Kim, B. S. D.-H.; Lee, M. S. B.; Park, K.-Y.; Kang, K., First-principles Study on the Charge Transport Mechanism of Lithium Sulfide (Li2S) in Lithium-Sulfur Batteries. *Chem. - Asian J.* **2016,** *11* (8), 1288-1292.

(93) Park, H.; Koh, H. S.; Siegel, D. J., First-Principles Study of Redox End Members in Lithium–Sulfur Batteries. *J. Phys. Chem. C* **2015,** *119* (9), 4675-4683.

(94) Chen, J.; Hummelshøj, J. S.; Thygesen, K. S.; Myrdal, J. S. G.; Nørskov, J. K.; Vegge, T., The role of transition metal interfaces on the electronic transport in lithium–air batteries. *Catal. Today* **2011**, Medium: X; Size: p. 2-9.

(95) Viswanathan, V.; Thygesen, K. S.; Hummelshøj, J. S.; Nørskov, J. K.; Girishkumar, G.; McCloskey, B. D.; Luntz, A. C., Electrical conductivity in Li_2O_2 and its role in determining capacity limitations in non-aqueous Li-O2 batteries. *J. Chem. Phys.* **2011,** *135* (21), 214704.

(96) Das, S. K.; Xu, S.; Emwas, A.-H.; Lu, Y. Y.; Srivastava, S.; Archer, L. A., High energy lithium-oxygen batteries - transport barriers and thermodynamics. *Energy Environ. Sci.* **2012,** *5* (10), 8927-8931.

(97) Lu, Y.-C.; Shao-Horn, Y., Probing the Reaction Kinetics of the Charge Reactions of Nonaqueous Li–O_2 Batteries. *J. Phys. Chem. Lett.* **2013,** *4* (1), 93-99.

(98) Luntz, A. C.; Viswanathan, V.; Voss, J.; Varley, J. B.; Nørskov, J. K.; Scheffler, R.; Speidel, A., Tunneling and Polaron Charge Transport through Li2O2 in Li–O2 Batteries. *J. Phys. Chem. Lett.* **2013,** *4* (20), 3494-3499.

(99) Radin, M. D.; Siegel, D. J., Charge transport in lithium peroxide: relevance for rechargeable metal-air batteries. *Energy Environ. Sci.* **2013,** *6* (8), 2370-2379.

(100) Viswanathan, V.; Nørskov, J. K.; Speidel, A.; Scheffler, R.; Gowda, S.; Luntz, A. C., Li–O_2 Kinetic Overpotentials: Tafel Plots from Experiment and First-Principles Theory. *J. Phys. Chem. Lett.* **2013,** *4* (4), 556-560.

(101) Fan, F. Y.; Carter, W. C.; Chiang, Y.-M., Mechanism and Kinetics of Li_2S Precipitation in Lithium–Sulfur Batteries. *Adv. Mater.* **2015,** *27* (35), 5203-5209.

(102) Lee, B.; Kim, J.; Yoon, G.; Lim, H.-D.; Choi, I.-S.; Kang, K., Theoretical Evidence for Low Charging Overpotentials of Superoxide Discharge Products in Metal–Oxygen Batteries. *Chem. Mater.* **2015,** *27* (24), 8406-8413.

(103) Moradabadi, A.; Kaghazchi, P., Thermodynamics and kinetics of defects in Li_2S. *Appl. Phys. Lett.* **2016,** *108* (21), 213906.

(104) Liu, Z.; Balbuena, P. B.; Mukherjee, P. P., Revealing Charge Transport Mechanisms in Li_2S_2 for Li–Sulfur Batteries. *J. Phys. Chem. Lett.* **2017,** *8* (7), 1324-1330.

(105) Liu, Z.; Balbuena, P. B.; Mukherjee, P. P., Hole Polaron Diffusion in the Final Discharge Product of Lithium–Sulfur Batteries. *J. Phys. Chem. C* **2017,** *121* (32), 17169-17175.

(106) Henkelman, G.; Jonsson, H., Improved tangent estimate in the nudged elastic band method for finding minimum energy paths and saddle points. *J. Chem. Phys.* **2000,** *113* (22), 9978-9985.

(107) Henkelman, G.; Uberuaga, B. P.; Jónsson, H., A climbing image nudged elastic band method for finding saddle points and minimum energy paths. *J. Chem. Phys.* **2000,** *113* (22), 9901-9904.

(108) Sheppard, D.; Terrell, R.; Henkelman, G., Optimization methods for finding minimum energy paths. *J. Chem. Phys.* **2008,** *128* (13), 134106.

(109) Thompson, T.; Yu, S.; Williams, L.; Schmidt, R. D.; Garcia-Mendez, R.; Wolfenstine, J.; Allen, J. L.; Kioupakis, E.; Siegel, D. J.; Sakamoto, J., Electrochemical Window of the Li-Ion Solid Electrolyte $Li_7La_3Zr_2O_{12}$. *ACS Energy Lett.* **2017,** *2* (2), 462-468.

(110) Manthiram, A.; Yu, X.; Wang, S., Lithium battery chemistries enabled by solid-state electrolytes. *Nat. Rev. Mater.* **2017,** *2*, 16103-16103.

(111) Chen, S.; Xie, D.; Liu, G.; Mwizerwa, J. P.; Zhang, Q.; Zhao, Y.; Xu, X.; Yao, X., Sulfide solid electrolytes for all-solid-state lithium batteries: Structure, conductivity, stability and application. *Energy Storage Mater.* **2018,** *14*, 58-74.

(112) Ong, S. P.; Mo, Y.; Richards, W. D.; Miara, L.; Lee, H. S.; Ceder, G., Phase stability, electrochemical stability and ionic conductivity of the $Li_{10\pm1}MP_2X_{12}$ (M = Ge, Si, Sn, Al or P, and X = O, S or Se) family of superionic conductors. *Energy Environ. Sci.* **2013,** *6* (1), 148-156.

(113) Goodenough, J. B.; Kim, Y., Challenges for rechargeable Li batteries. *Chem. Mater.* **2010,** *22*, 587-603.

(114) The absolute electrode potential: an explanatory note (Recommendations 1986). *J. Electroanal. Chem. Interfacial Electrochem.* **1986,** *209* (2), 417-428.

(115) Mishra, U. K.; Singh, J., *Semiconductor Device Physics and Design*. Springer: Dordrecht, 2007.

(116) Nolan, A. M.; Zhu, Y.; He, X.; Bai, Q.; Mo, Y., Computation-Accelerated Design of Materials and Interfaces for All-Solid-State Lithium-Ion Batteries. *Joule* **2018**.

(117) Peljo, P.; Girault, H. H., Electrochemical potential window of battery electrolytes: the HOMO–LUMO misconception. *Energy Environ. Sci.* **2018,** *11* (9), 2306-2309.

(118) Hohenberg, P.; Kohn, W., Inhomogeneous Electron Gas. *Phys. Rev.* **1964,** *136* (3B), B864-B871.

(119) Kohn, W.; Sham, L. J., Self-Consistent Equations Including Exchange and Correlation Effects. *Phys. Rev.* **1965,** *140* (4A), A1133-A1138.

(120) Perdew, J. P.; Ruzsinszky, A.; Tao, J.; Staroverov, V. N.; Scuseria, G. E.; Csonka, G. I., Prescription for the design and selection of density functional approximations: More constraint satisfaction with fewer fits. *J. Chem. Phys.* **2005,** *123* (6), 062201.

(121) Vosko, S. H.; Wilk, L.; Nusair, M., Accurate spin-dependent electron liquid correlation energies for local spin density calculations: a critical analysis. *Can. J. Phys.* **1980,** *58* (8), 1200-1211.

(122) Perdew, J. P.; Zunger, A., Self-interaction correction to density-functional approximations for many-electron systems. *Phys. Rev. B* **1981,** *23* (10), 5048-5079.

(123) Perdew, J. P.; Wang, Y., Accurate and simple analytic representation of the electron-gas correlation energy. *Phys. Rev. B* **1992,** *45* (23), 13244-13249.

(124) Ceperley, D. M.; Alder, B. J., Ground State of the Electron Gas by a Stochastic Method. *Phys. Rev. Lett.* **1980,** *45* (7), 566-569.

(125) Grossman, J. C.; Mitas, L.; Raghavachari, K., Structure and Stability of Molecular Carbon: Importance of Electron Correlation. *Phys. Rev. Lett.* **1996,** *76* (6), 1006-1006.

(126) Zupan, A.; Blaha, P.; Schwarz, K.; Perdew, J. P., Pressure-induced phase transitions in solid Si, SiO_2 and Fe: Performance of local-spin-density and generalized-gradient-approximation density functionals. *Phys. Rev. B* **1998,** *58* (17), 11266-11272.

(127) Langreth, D. C.; Mehl, M. J., Beyond the local-density approximation in calculations of ground-state electronic properties. *Phys. Rev. B* **1983,** *28* (4), 1809-1834.

(128) Becke, A. D., Density-functional exchange-energy approximation with correct asymptotic behavior. *Phys. Rev. A* **1988,** *38* (6), 3098-3100.

(129) Lee, C.; Yang, W.; Parr, R. G., Development of the Colle-Salvetti correlation-energy formula into a functional of the electron density. *Phys. Rev. B* **1988,** *37* (2), 785-789.

(130) Becke, A. D., Density functional calculations of molecular bond energies. *J. Chem. Phys.* **1986,** *84* (8), 4524-4529.

(131) Perdew, J. P.; Yue, W., Accurate and simple density functional for the electronic exchange energy: Generalized gradient approximation. *Phys. Rev. B* **1986,** *33* (12), 8800-8802.

(132) Perdew, J. P.; Chevary, J. A.; Vosko, S. H.; Jackson, K. A.; Pederson, M. R.; Singh, D. J.; Fiolhais, C., Atoms, molecules, solids, and surfaces: Applications of the generalized gradient approximation for exchange and correlation. *Phys. Rev. B* **1992,** *46* (11), 6671-6687.

(133) Perdew, J. P.; Burke, K.; Wang, Y., Generalized gradient approximation for the exchange-correlation hole of a many-electron system. *Phys. Rev. B* **1996,** *54* (23), 16533-16539.

(134) Perdew, J. P.; Burke, K.; Wang, Y., Erratum: Generalized gradient approximation for the exchange-correlation hole of a many-electron system [Phys. Rev. B 54, 16 533 (1996)]. *Phys. Rev. B* **1998,** *57* (23), 14999-14999.

(135) Perdew, J. P.; Chevary, J. A.; Vosko, S. H.; Jackson, K. A.; Pederson, M. R.; Singh, D. J.; Fiolhais, C., Erratum: Atoms, molecules, solids, and surfaces: Applications of the generalized gradient approximation for exchange and correlation. *Phys. Rev. B* **1993,** *48* (7), 4978-4978.

(136) Perdew, J. P.; Burke, K.; Ernzerhof, M., Generalized Gradient Approximation Made Simple. *Phys. Rev. Lett.* **1996,** *77* (18), 3865-3868.

(137) Staroverov, V. N.; Scuseria, G. E.; Tao, J.; Perdew, J. P., Tests of a ladder of density functionals for bulk solids and surfaces. *Phys. Rev. B* **2004,** *69* (7), 075102.

(138) Staroverov, V. N.; Scuseria, G. E.; Tao, J.; Perdew, J. P., Comparative assessment of a new nonempirical density functional: Molecules and hydrogen-bonded complexes. *J. Chem. Phys.* **2003,** *119* (23), 12129-12137.

(139) Dion, M.; Rydberg, H.; Schröder, E.; Langreth, D. C.; Lundqvist, B. I., Van der Waals Density Functional for General Geometries. *Phys. Rev. Lett.* **2004,** *92* (24), 246401.

(140) Zhang, Y.; Yang, W., Comment on ``Generalized Gradient Approximation Made Simple". *Phys. Rev. Lett.* **1998,** *80* (4), 890-890.

(141) Klimeš, J.; Bowler, D. R.; Michaelides, A., Chemical accuracy for the van der Waals density functional. *J. Phys.: Condens. Matter* **2010,** *22* (2), 022201.

(142) Lee, K.; Murray, É. D.; Kong, L.; Lundqvist, B. I.; Langreth, D. C., Higher-accuracy van der Waals density functional. *Phys. Rev. B* **2010,** *82* (8), 081101.

(143) Klimeš, J.; Bowler, D. R.; Michaelides, A., Van der Waals density functionals applied to solids. *Phys. Rev. B* **2011,** *83* (19), 195131.

(144) Hamada, I., van der Waals density functional made accurate. *Phys. Rev. B* **2014,** *89* (12), 121103.

(145) Liechtenstein, A. I.; Anisimov, V. I.; Zaanen, J., Density-functional theory and strong interactions: Orbital ordering in Mott-Hubbard insulators. *Phys. Rev. B* **1995,** *52* (8), R5467-R5470.

(146) Dudarev, S. L.; Botton, G. A.; Savrasov, S. Y.; Humphreys, C. J.; Sutton, A. P., Electron-energy-loss spectra and the structural stability of nickel oxide: An LSDA+U study. *Phys. Rev. B* **1998,** *57* (3), 1505-1509.

(147) Heyd, J.; Scuseria, G. E.; Ernzerhof, M., Hybrid functionals based on a screened Coulomb potential. *J. Chem. Phys.* **2003,** *118* (18), 8207-8215.

(148) Heyd, J.; Scuseria, G. E., Efficient hybrid density functional calculations in solids: Assessment of the Heyd–Scuseria–Ernzerhof screened Coulomb hybrid functional. *J. Chem. Phys.* **2004,** *121* (3), 1187-1192.

(149) Krukau, A. V.; Vydrov, O. A.; Izmaylov, A. F.; Scuseria, G. E., Influence of the exchange screening parameter on the performance of screened hybrid functionals. *J. Chem. Phys.* **2006,** *125* (22), 224106.

(150) Li, S.; Liu, J.; Liu, B., First-Principles Study of the Charge Transport Mechanisms in Lithium Superoxide. *Chem. Mater.* **2017,** *29* (5), 2202-2210.

(151) Smith, J. G.; Naruse, J.; Hiramatsu, H.; Siegel, D. J., Intrinsic Conductivity in Magnesium-Oxygen Battery Discharge Products: MgO and MgO2. *Chem. Mater.* **2017**.

(152) Yang, S.; Siegel, D. J., Intrinsic Conductivity in Sodium–Air Battery Discharge Phases: Sodium Superoxide vs Sodium Peroxide. *Chem. Mater.* **2015,** *27* (11), 3852-3860.

(153) Park, H.; Kumar, N.; Melander, M.; Vegge, T.; Garcia Lastra, J. M.; Siegel, D. J., Adiabatic and Nonadiabatic Charge Transport in Li–S Batteries. *Chem. Mater.* **2018,** *30* (3), 915-928.

(154) Hybertsen, M. S.; Louie, S. G., Electron correlation in semiconductors and insulators: Band gaps and quasiparticle energies. *Phys. Rev. B* **1986,** *34* (8), 5390-5413.

(155) Aulbur, W. G.; Jönsson, L.; Wilkins, J. W., Quasiparticle Calculations in Solids. In *Solid State Physics*, Ehrenreich, H.; Spaepen, F., Eds. Academic Press: 2000; Vol. 54, pp 1-218.

(156) Hedin, L., New Method for Calculating the One-Particle Green's Function with Application to the Electron-Gas Problem. *Phys. Rev.* **1965,** *139* (3A), A796-A823.

(157) Shishkin, M.; Kresse, G., Implementation and performance of the frequency-dependent *GW* method within the PAW framework. *Phys. Rev. B: Condens. Matter Mater. Phys.* **2006,** *74* (3), 035101.

(158) Shishkin, M.; Kresse, G., Self-consistent GW calculations for semiconductors and insulators. *Phys. Rev. B: Condens. Matter Mater. Phys.* **2007,** *75* (23), 235102-235102.

(159) Shishkin, M.; Marsman, M.; Kresse, G., Accurate quasiparticle spectra from self-consistent GW calculations with vertex corrections. *Phys. Rev. Lett.* **2007,** *99* (24), 246403-246403.

(160) Fuchs, F.; Furthmüller, J.; Bechstedt, F.; Shishkin, M.; Kresse, G., Quasiparticle band structure based on a generalized Kohn-Sham scheme. *Phys. Rev. B* **2007,** *76* (11), 115109.

(161) Kresse, G.; Furthmuller, J., Efficient iterative schemes for ab initio total-energy calculations using a plane-wave basis set. *Phys. Rev. B* **1996,** *54* (16), 11169-11186.

(162) Kresse, G.; Furthmuller, J., Efficiency of ab-initio total energy calculations for metals and semiconductors using a plane-wave basis set. *Comput. Mater. Sci.* **1996,** *6* (1), 15-50.

(163) Kresse, G.; Joubert, D., From ultrasoft pseudopotentials to the projector augmented-wave method. *Phys. Rev. B* **1999,** *59* (3), 1758-1775.

(164) Blöchl, P. E., Projector augmented-wave method. *Phys. Rev. B* **1994,** *50* (24), 17953-17979.

(165) Monkhorst, H. J.; Pack, J. D., Special points for Brillouin-zone integrations. *Phys. Rev. B* **1976,** *13* (12), 5188-5192.

(166) Murnaghan, F. D., The Compressibility of Media under Extreme Pressures. *Proc. Natl. Acad. Sci.* **1944,** *30* (9), 244-247.

(167) Wei, S.; Chou, M. Y., *Ab initio* calculation of force constants and full phonon dispersions. *Phys. Rev. Lett.* **1992,** *69* (19), 2799-2802.

(168) Reuter, K.; Scheffler, M., Composition, structure, and stability of RuO_2(110) as a function of oxygen pressure. *Phys. Rev. B* **2001,** *65* (3), 035406.

(169) Mathew, K.; Sundararaman, R.; Letchworth-Weaver, K.; Arias, T. A.; Hennig, R. G., Implicit solvation model for density-functional study of nanocrystal surfaces and reaction pathways. *J. Chem. Phys.* **2014,** *140* (8), 084106.

(170) Fishman, M.; Zhuang, H. L.; Mathew, K.; Dirschka, W.; Hennig, R. G., Accuracy of exchange-correlation functionals and effect of solvation on the surface energy of copper. *Phys. Rev. B* **2013,** *87* (24), 245402.

(171) Wohlfarth, C., Dielectric constant of 1,2-dimethoxyethane. In *Supplement to IV/6*, Lechner, M. D., Ed. Springer Berlin Heidelberg: 2008; Vol. 17, pp 263-268.

(172) Slotwinski, T.; Trivisonno, J., Temperature dependence of the elastic constants of single crystal lithium. *J. Phys. Chem. Solids* **1969,** *30* (5), 1276-1278.

(173) Berliner, R.; Fajen, O.; Smith, H. G.; Hitterman, R. L., Neutron powder-diffraction studies of lithium, sodium, and potassium metal. *Phys. Rev. B* **1989,** *40* (18), 12086-12097.

(174) Buehrer, W.; Altorfer, F.; Mesot, J.; Bill, H.; Carron, P.; Smith, H. G., Lattice dynamics and the diffuse phase transition of lithium sulphide investigated by coherent neutron scattering. *J. Phys.: Condens. Matter* **1991,** *3* (9), 1055.

(175) David, W. I. F.; Ibberson, R. M.; Cox, S. F. J.; Wood, P. T., Order-disorder transition in monoclinic sulfur: a precise structural study by high-resolution neutron powder diffraction. *Acta Crystallogr. Sect. B* **2006,** *62* (6), 953-959.

(176) Luo, H.; Ruoff, A., X-ray-diffraction study of sulfur to 32 GPa: Amorphization at 25 GPa. *Phys. Rev. B* **1993,** *48* (1), 569-572.

(177) Rettig, S. J.; Trotter, J., Refinement of the structure of orthorhombic sulfur, α-S8. *Acta Crystallogr. Sect. C* **1987,** *43* (12), 2260-2262.

(178) Hautier, G.; Ong, S. P.; Jain, A.; Moore, C. J.; Ceder, G., Accuracy of density functional theory in predicting formation energies of ternary oxides from binary oxides and its implication on phase stability. *Phys. Rev. B* **2012,** *85* (15), 155208.

(179) Cañas, N. A.; Wolf, S.; Wagner, N.; Friedrich, K. A., In-situ X-ray diffraction studies of lithium–sulfur batteries. *J. Power Sources* **2013,** *226* (0), 313-319.

(180) Wangman, D. D.; Evans, Q. H.; Parker, V. B.; Schumm, R. H.; Halow, I.; Bailey, S. M.; Churney, K. L.; Nuttall, R. L., The NBS Tables of Chemical Thermodynamic Properties. Selected Values for Inorganic and C 1 and C 2 Organic Substances in SI Units. *J. Phys. Chem. Ref. Data* **1982,** *11(Supplement No.2)*.

(181) Liu, G.; Niu, P.; Yin, L.; Cheng, H.-M., α-Sulfur Crystals as a Visible-Light-Active Photocatalyst. *J. Am. Chem. Soc.* **2012,** *134* (22), 9070-9073.

(182) Abass, A. K.; Ahmad, N. H., Indirect band gap investigation of orthorhombic single crystals of sulfur. *J. Phys. Chem. Solids* **1986,** *47* (2), 143-145.

(183) Sze, S. M.; Ng, K. K., Appendix F Properties of Important Semiconductors. In *Physics of Semiconductor Devices*, John Wiley & Sons, Inc.: 2006; pp 789-789.

(184) Wulff, G., On the question of the rate of growth and dissolution of crystal surfaces. *Z Krystallogr. Mineral.* **1901,** *34*, 449.

(185) Nagao, M.; Hayashi, A.; Tatsumisago, M., High-capacity Li2S-nanocarbon composite electrode for all-solid-state rechargeable lithium batteries. *J. Mater. Chem.* **2012,** *22* (19), 10015-10020.

(186) Cai, K.; Song, M.-K.; Cairns, E. J.; Zhang, Y., Nanostructured Li2S–C Composites as Cathode Material for High-Energy Lithium/Sulfur Batteries. *Nano Lett.* **2012,** *12* (12), 6474-6479.

(187) Cuisinier, M.; Cabelguen, P. E.; Adams, B. D.; Garsuch, A.; Balasubramanian, M.; Nazar, L. F., Unique behaviour of nonsolvents for polysulphides in lithium-sulphur batteries. *Energy Environ. Sci.* **2014,** *7* (8), 2697-2705.

(188) Suo, L.; Hu, Y.-S.; Li, H.; Armand, M.; Chen, L., A new class of Solvent-in-Salt electrolyte for high-energy rechargeable metallic lithium batteries. *Nat. Commun.* **2013,** *4*, 1481.

(189) Dokko, K.; Tachikawa, N.; Yamauchi, K.; Tsuchiya, M.; Yamazaki, A.; Takashima, E.; Park, J.-W.; Ueno, K.; Seki, S.; Serizawa, N.; Watanabe, M., Solvate Ionic Liquid Electrolyte for Li–S Batteries. *J. Electrochem. Soc.* **2013,** *160* (8), A1304-A1310.

(190) Lee, K.; Howe, J. D.; Lin, L.-C.; Smit, B.; Neaton, J. B., Small-Molecule Adsorption in Open-Site Metal–Organic Frameworks: A Systematic Density Functional Theory Study for Rational Design. *Chem. Mater.* **2015,** *27* (3), 668-678.

(191) Henkelman, G.; Arnaldsson, A.; Jónsson, H., A fast and robust algorithm for Bader decomposition of charge density. *Comput. Mater. Sci.* **2006,** *36* (3), 354-360.

(192) Tang, W.; Sanville, E.; Henkelman, G., A grid-based Bader analysis algorithm without lattice bias. *J. Phys.: Condens. Matter* **2009,** *21* (8), 084204.

(193) Rana, M. K.; Koh, H. S.; Zuberi, H.; Siegel, D. J., Methane Storage in Metal-Substituted Metal–Organic Frameworks: Thermodynamics, Usable Capacity, and the Impact of Enhanced Binding Sites. *J. Phys. Chem. C* **2014,** *118* (6), 2929-2942.

(194) Dietzel, P. D. C.; Panella, B.; Hirscher, M.; Blom, R.; Fjellvag, H., Hydrogen adsorption in a nickel based coordination polymer with open metal sites in the cylindrical cavities of the desolvated framework. *Chem. Commun. (Cambridge, U. K.)* **2006,** (9), 959-961.

(195) Sun, L.; Campbell, M. G.; Dincă, M., Electrically Conductive Porous Metal–Organic Frameworks. *Angew. Chem. Int. Ed.* **2016,** *55* (11), 3566-3579.

(196) Talin, A. A.; Centrone, A.; Ford, A. C.; Foster, M. E.; Stavila, V.; Haney, P.; Kinney, R. A.; Szalai, V.; El Gabaly, F.; Yoon, H. P.; Léonard, F.; Allendorf, M. D., Tunable Electrical Conductivity in Metal-Organic Framework Thin-Film Devices. *Science* **2014,** *343* (6166), 66-69.

(197) Lee, L.-H., *Fundamentals of Adhesion*. Plenum Publishing Corporation: Webster, NY, 1991.

(198) Eroglu, D.; Zavadil, K. R.; Gallagher, K. G., Critical Link between Materials Chemistry and Cell-Level Design for High Energy Density and Low Cost Lithium-Sulfur Transportation Battery. *J. Electrochem. Soc.* **2015,** *162* (6), A982-A990.

(199) Adams, A. R.; Gibbons, D. J.; Spear, W. E., Electron hopping transport in orthorhombic S crystals. *Solid State Commun.* **1964,** *2* (12), 387-389.

(200) Pacchioni, G., Modeling doped and defective oxides in catalysis with density functional theory methods: Room for improvements. *J. Chem. Phys.* **2008,** *128* (18), 182505.

(201) Alkauskas, A.; Broqvist, P.; Pasquarello, A., Defect levels through hybrid density functionals: Insights and applications. *Phys. Status Solidi B* **2011,** *248* (4), 775-789.

(202) Lambrecht, W. R. L., Which electronic structure method for the study of defects: A commentary. *Phys. Status Solidi B* **2011,** *248* (7), 1547-1558.

(203) Komsa, H.-P.; Rantala, T. T.; Pasquarello, A., Finite-size supercell correction schemes for charged defect calculations. *Phys. Rev. B* **2012,** *86* (4), 045112.

(204) Walle, C. G. V. d.; Neugebauer, J., First-principles calculations for defects and impurities: Applications to III-nitrides. *J. Appl. Phys.* **2004,** *95* (8), 3851-3879.

(205) Sulfur (S) dielectric constant, refractive index, orthorhombic alpha-modification. In *Non-Tetrahedrally Bonded Elements and Binary Compounds I*, Madelung, O.; Rössler, U.; Schulz, M., Eds. Springer Berlin Heidelberg: Berlin, Heidelberg, 1998; pp 1-5.

(206) Makov, G.; Payne, M. C., Periodic boundary conditions in ab initio calculations. *Phys. Rev. B* **1995,** *51* (7), 4014-4022.

(207) Hummelshøj, J. S.; Luntz, A. C.; Nørskov, J. K., Theoretical evidence for low kinetic overpotentials in Li-O2 electrochemistry. *J. Chem. Phys.* **2013,** *138* (3), 034703.

(208) Loftager, S.; García-Lastra, J. M.; Vegge, T., A Density Functional Theory Study of the Ionic and Electronic Transport Mechanisms in $LiFeBO_3$ Battery Electrodes. *J. Phys. Chem. C* **2016,** *120* (33), 18355-18364.

(209) Wu, Q.; Van Voorhis, T., Direct optimization method to study constrained systems within density-functional theory. *Phys. Rev. A* **2005,** *72* (2), 024502.

(210) Kaduk, B.; Kowalczyk, T.; Van Voorhis, T., Constrained Density Functional Theory. *Chem. Rev. (Washington, DC, U. S.)* **2012,** *112* (1), 321-370.

(211) Melander, M.; Jónsson, E. O.; Mortensen, J. J.; Vegge, T.; García Lastra, J. M., Implementation of Constrained DFT for Computing Charge Transfer Rates within the Projector Augmented Wave Method. *J. Chem. Theory Comput.* **2016,** *12* (11), 5367-5378.

(212) Mortensen, J. J.; Hansen, L. B.; Jacobsen, K. W., Real-space grid implementation of the projector augmented wave method. *Phys. Rev. B* **2005,** *71* (3), 035109.

(213) Enkovaara, J.; Rostgaard, C.; Mortensen, J. J.; Chen, J.; Dułak, M.; Ferrighi, L.; Gavnholt, J.; Glinsvad, C.; Haikola, V.; Hansen, H. A.; Kristoffersen, H. H.; Kuisma, M.; Larsen, A. H.; Lehtovaara, L.; Ljungberg, M.;

Lopez-Acevedo, O.; Moses, P. G.; Ojanen, J.; Olsen, T.; Petzold, V.; Romero, N. A.; Stausholm-Møller, J.; Strange, M.; Tritsaris, G. A.; Vanin, M.; Walter, M.; Hammer, B.; Häkkinen, H.; Madsen, G. K. H.; Nieminen, R. M.; Nørskov, J. K.; Puska, M.; Rantala, T. T.; Schiøtz, J.; Thygesen, K. S.; Jacobsen, K. W., Electronic structure calculations with GPAW: a real-space implementation of the projector augmented-wave method. *J. Phys.: Condens. Matter* **2010,** *22* (25), 253202.

(214) Kuznetsov, A. M.; Ulstrup, J., Electron transfer in chemistry and biology: an introduction to the theory. **1999**.

(215) Marcus, R. A., On the theory of oxidation-reduction reactions involving electron transfer. I. *J. Chem. Phys.* **1956,** *24* (5), 966-978.

(216) Marcus, R. A.; Sutin, N., Electron transfers in chemistry and biology. *Biochim. Biophys. Acta, Rev. Bioenerg.* **1985,** *811* (3), 265-322.

(217) Dolezalek, F. K.; Spear, W. E., Carrier recombination in orthorhombic sulphur. *J. Phys. Chem. Solids* **1975,** *36* (7), 819-825.

(218) Nitzki, V.; Stössel, W., Anisotropy of Electron and Hole Mobilities in Orthorhombic Sulphur Crystals. *Phys. Status Solidi B* **1970,** *39* (1), 309-316.

(219) Gill, W. D.; Street, G. B.; Macdonald, R. E., Transport properties of vapor grown orthorhombic sulfur crystals. *J. Phys. Chem. Solids* **1967,** *28* (8), 1517-1518.

(220) Adams, A. R.; Spear, W. E., The charge transport in orthorhombic sulphur crystals. *J. Phys. Chem. Solids* **1964,** *25* (10), 1113-1118.

(221) Neumann, H., Leitfähigkeit und dielektrische Hysteresis einiger Isolatoren und ihre Beeinflussung durch Röntgen- undγ-Strahlen. *Eur. Phys. J. A* **1927,** *45* (9), 717-748.

(222) Sproul, A. B.; Green, M. A., Improved value for the silicon intrinsic carrier concentration from 275 to 375 K. *J. Appl. Phys.* **1991,** *70* (2), 846-854.

(223) Gibbons, D. J.; Spear, W. E., Electron hopping transport and trapping phenomena in orthorhombic sulphur crystals. *J. Phys. Chem. Solids* **1966,** *27* (11), 1917-1925.

(224) Garcia-Lastra, J. M.; Mowbray, D. J.; Thygesen, K. S.; Rubio, A.; Jacobsen, K. W., Modeling nanoscale gas sensors under realistic conditions: Computational screening of metal-doped carbon nanotubes. *Phys. Rev. B* **2010,** *81* (24), 10.

(225) Jurchescu, O. D.; Baas, J.; Palstra, T. T. M., Effect of impurities on the mobility of single crystal pentacene. *Appl. Phys. Lett.* **2004,** *84* (16), 3061-3063.

(226) Munn, R. W.; Siebrand, W., Theory of electron-phonon interactions in organic crystals. Effect on charge carrier transport. *Discuss. Faraday Soc.* **1971,** *51* (0), 17-23.

(227) Silbey, R.; Munn, R. W., General theory of electronic transport in molecular crystals. I. Local linear electron–phonon coupling. *J. Chem. Phys.* **1980,** *72* (4), 2763-2773.

(228) Nitzki, V.; Stössel, W., Anisotropy of Electron and Hole Mobilities in Orthorhombic Sulphur Crystals. *Phys. Status Solidi (b)* **1970,** *39* (1), 309-316.

(229) Ashcroft, N. W.; Mermin, N. D., *Solid State Physics*. Holt, Rinehart and Winston: 1976.

(230) Stevens, E. D.; DeLucia, M. L.; Coppens, P., Experimental observation of the effect of crystal field splitting on the electron density distribution of iron pyrite. *Inorg. Chem.* **1980,** *19* (4), 813-820.

(231) Tilley, R. J. D., Defects and Diffusion. In *Defects in Solids*, John Wiley & Sons, Inc.: 2008; pp 205-250.

(232) Radin, M. D.; Monroe, C. W.; Siegel, D. J., How Dopants Can Enhance Charge Transport in Li2O2. *Chem. Mater.* **2015,** *27* (3), 839-847.

(233) Cook, B. E.; Spear, W. E., The optical properties of orthorhombic sulphur crystals in the vacuum ultraviolet. *J. Phys. Chem. Solids* **1969,** *30* (5), 1125-1134.

(234) Coppens, P.; Yang, Y. W.; Blessing, R. H.; Copper, W. F.; Larsen, F. K., The experimental charge distribution in sulfur containing molecules. Analysis of cyclic octasulfur at 300 and 100 K. *J. Am. Chem. Soc.* **1977,** *99* (3), 760-766.

(235) Shishkin, M.; Kresse, G., Implementation and performance of the frequency-dependent GW method within the PAW framework. *Phys. Rev. B* **2006,** *74* (3), 35101-35101.

(236) Kumar, N.; Siegel, D. J., Interface-Induced Renormalization of Electrolyte Energy Levels in Magnesium Batteries. *J. Phys. Chem. Lett.* **2016,** *7* (5), 874-881.

(237) Ong, S. P.; Wang, L.; Kang, B.; Ceder, G., Li−Fe−P−O_2 Phase Diagram from First Principles Calculations. *Chem. Mater.* **2008,** *20* (5), 1798-1807.

(238) Ong, S. P.; Jain, A.; Hautier, G.; Kang, B.; Ceder, G., Thermal stabilities of delithiated olivine MPO_4 (M=Fe, Mn) cathodes investigated using first principles calculations. *Electrochem. Commun.* **2010,** *12* (3), 427-430.

(239) Zhang, Z.; Chen, S.; Yang, J.; Wang, J.; Yao, L.; Yao, X.; Cui, P.; Xu, X., Interface Re-Engineering of Li10GeP2S12 Electrolyte and Lithium anode for All-Solid-State Lithium Batteries with Ultralong Cycle Life. *ACS Appl. Mater. Interfaces* **2018,** *10* (3), 2556-2565.

(240) Grüneis, A.; Kresse, G.; Hinuma, Y.; Oba, F., Ionization Potentials of Solids: The Importance of Vertex Corrections. *Phys. Rev. Lett.* **2014,** *112* (9), 96401-96401.

(241) Hinuma, Y.; Grüneis, A.; Kresse, G.; Oba, F., Band alignment of semiconductors from density-functional theory and many-body perturbation theory. *Phys. Rev. B* **2014,** *90* (15), 155405-155405.

(242) Hummelshøj, J. S.; Luntz, A. C.; Nørskov, J. K., Theoretical evidence for low kinetic overpotentials in Li-O2 electrochemistry. *J. Chem. Phys.* **2013,** *138* (3), 34703-34703.

(243) Oh, K.; Chang, D.; Lee, B.; Kim, D.-H.; Yoon, G.; Park, I.; Kim, B.; Kang, K., Native Defects in Li10GeP2S12 and Their Effect on Lithium Diffusion. *Chem. Mater.* **2018**.

(244) Kamaya, N.; Homma, K.; Yamakawa, Y.; Hirayama, M.; Kanno, R.; Yonemura, M.; Kamiyama, T.; Kato, Y.; Hama, S.; Kawamoto, K.; Mitsui, A., A lithium superionic conductor. *Nat. Mater.* **2011,** *10* (9), 682-686.

(245) Bron, P.; Johansson, S.; Zick, K.; Schmedt auf der Günne, J.; Dehnen, S.; Roling, B., $Li_{10}SnP_2S_{12}$: An Affordable Lithium Superionic Conductor. *J. Am. Chem. Soc.* **2013,** *135* (42), 15694-15697.

(246) Murayama, M.; Kanno, R.; Irie, M.; Ito, S.; Hata, T.; Sonoyama, N.; Kawamoto, Y., Synthesis of New Lithium Ionic Conductor Thio-LISICON—Lithium Silicon Sulfides System. *J. Solid State Chem.* **2002,** *168* (1), 140-148.

(247) Sang, L.; Haasch, R. T.; Gewirth, A. A.; Nuzzo, R. G., Evolution at the Solid Electrolyte/Gold Electrode Interface during Lithium Deposition and Stripping. *Chem. Mater.* **2017,** *29* (7), 3029-3037.

(248) Homma, K.; Yonemura, M.; Kobayashi, T.; Nagao, M.; Hirayama, M.; Kanno, R., Crystal structure and phase transitions of the lithium ionic conductor Li3PS4. *Solid State Ion.* **2011,** *182* (1), 53-58.

(249) Seo, I.; Martin, S. W., Fast lithium ion conducting solid state thin-film electrolytes based on lithium thio-germanate materials. *Acta Mater.* **2011,** *59* (4), 1839-1846.

(250) Kaib, T.; Haddadpour, S.; Kapitein, M.; Bron, P.; Schröder, C.; Eckert, H.; Roling, B.; Dehnen, S., New Lithium Chalcogenidotetrelates, LiChT: Synthesis and Characterization of the Li+-Conducting Tetralithium ortho-Sulfidostannate Li4SnS4. *Chem. Mater.* **2012,** *24* (11), 2211-2219.

(251) Vinatier, P.; Gravereau, P.; Ménétrier, M.; Trut, L.; Levasseur, A., Li_3BS_3. *Acta Crystallogr. Sect. C* **1994,** *50* (8), 1180-1183.

(252) Sendek, A. D.; Cubuk, E. D.; Antoniuk, E. R.; Cheon, G.; Cui, Y.; Reed, E. J., Machine Learning-Assisted Discovery of Solid Li-Ion Conducting Materials. *Chem. Mater.* **2018,** *31* (2), 342-352.

(253) Wenzel, S.; Randau, S.; Leichtweiß, T.; Weber, D. A.; Sann, J.; Zeier, W. G.; Janek, J., Direct Observation of the Interfacial Instability of the Fast Ionic Conductor $Li_{10}GeP_2S_{12}$ at the Lithium Metal Anode. *Chem. Mater.* **2016,** *28* (7), 2400-2407.

(254) Bianchini, F.; Fjellvåg, H.; Vajeeston, P., A first-principle investigation of the Li diffusion mechanism in the super-ionic conductor lithium orthothioborate Li_3BS_3 structure. *Mater. Lett.* **2018,** *219*, 186-189.

(255) Zhu, Y.; He, X.; Mo, Y., Origin of Outstanding Stability in the Lithium Solid Electrolyte Materials: Insights from Thermodynamic Analyses Based on First-Principles Calculations. *ACS Appl. Mater. Interfaces* **2015,** *7* (42), 23685-23693.

(256) Paolella, A.; Zhu, W.; Marceau, H.; Kim, C.-s.; Feng, Z.; Liu, D.; Gagnon, C.; Trottier, J.; Abdelbast, G.; Hovington, P.; Vijh, A.; Demopoulos, G. P.; Armand, M.; Zaghib, K., Transient existence of crystalline lithium disulfide Li_2S_2 in a lithium-sulfur battery. *J. Power Sources* **2016,** *325*, 641-645.

(257) Park, H.; Siegel, D. J., Tuning the Adsorption of Polysulfides in Lithium–Sulfur Batteries with Metal–Organic Frameworks. *Chem. Mater*. **2017**, *29* (11), 4932-4939.

(258) Li, F.; Zhang, X.; Liu, X.; Zhao, M., Novel Conductive Metal–Organic Framework for a High-Performance Lithium–Sulfur Battery Host: 2D Cu-Benzenehexathial (BHT). *ACS Appl. Mater. Interfaces* **2018,** *10* (17), 15012-15020.

(259) Xu, K.; Liu, X.; Liang, J.; Cai, J.; Zhang, K.; Lu, Y.; Wu, X.; Zhu, M.; Liu, Y.; Zhu, Y.; Wang, G.; Qian, Y., Manipulating the Redox Kinetics of Li–S Chemistry by Tellurium Doping for Improved Li–S Batteries. *ACS Energy Lett.* **2018,** *3* (2), 420-427.